

# Improved Multiphase Smoothed Particle Hydrodynamics

by

Mostafa Safdari Shadloo

Thesis Submitted to  
the Graduate School of Engineering and Natural Sciences  
in Partial Fulfillment of  
the Requirements for the Degree of  
Doctor of Philosophy

SABANCI UNIVERSITY

January 2013

Improved Multiphase Smoothed Particle Hydrodynamics

APPROVED BY

Associate professor Dr. Mehmet Yildiz .....  
(Thesis Supervisor)

Professor Dr. Ali Rana Atilgan .....

Associate Professor Dr. Gullu Kiziltas Sendur .....

Assistant Professor Dr. Burc Misirlioglu .....

Assistant Professor Dr. Robert Weiss .....  
(Virginia Tech. University)

DATE OF APPROVAL: 7th January 2013

©Mostafa Safdari Shadloo 2013  
All Rights Reserved

# *Acknowledgements*

I would like to thank:

- Dr. Mehmet Yildiz, for offering me this great opportunity to continue my education. I would like to say special thanks to him for his thoughtful advice, guidance and his patience. He inspired me academically and more important personally during my PhD career.
- Dr. Robert Weiss, for hosting me and allowing me access to their world class facilities. The skills and experience I gained there will be highly beneficial to me for the rest of my career.
- Thesis juries, for their valuable time and constructive comments, which improved the quality of the current work significantly.
- Yousef Jameel scholarship, for providing its highly prestigious fellowship.
- European Commission Research Directorate General, for Marie Curie International Reintegration Grant Program (with the grant agreement number of PIRG03 -GA -2008 -231048).
- Sabanci University, for providing the excellent research environment and its financial support.
- My family and friends, for their support, advice, motivation during my stay at Sabanci university.
- My wife, for her relentless support and encouragement for me to pursue my dreams academically, professionally and personally; and the personal sacrifices she has made to allow me to do this.

# Improved Multiphase Smoothed Particle Hydrodynamics

Mostafa Safdari Shadloo

ME, PhD. Thesis, Jan. 2013

Thesis Supervisor: Dr. Mehmet Yildiz

**Keywords:** Smoothed Particle Hydrodynamics, Meshless Method, Multiple Boundary Tangents (MBT) Method, Multi-Phase Fluid Flows, Continuum Surface Force (CSF), Hydrodynamic Instability, Electrohydrodynamics.

## Abstract

Smoothed Particle Hydrodynamics (SPH) is a relatively new meshless numerical approach which has attracted significant attention in the last 15 years. Compared with the conventional mesh-dependent computational fluid dynamics (CFD) methods, the SPH approach exhibits unique advantages in modeling multiphase fluid flows and associated transport phenomena due to its capabilities of handling complex material surface behavior as well as modeling complicated physics in a relatively simple manner. On the other hand, as SPH is still a developing CFD tool, it is vital to investigate its attributes, namely, advantages or potential limitations in modeling different multiphase flow problems to further understand and then improve this technique. Toward this end, this work aims to design a computational code using SPH method for the simulation of multiphase flows.

In this work, we present numerical solutions for flow over an airfoil and square obstacle using both weakly compressible and incompressible SPH method with an improved solid boundary treatment approach, referred to as Multiple Boundary Tangents (MBT) method. It is shown that the MBT boundary treatment technique is very effective for tackling boundaries of complex shapes. Also, we have proposed the usage of the repulsive component of the Leonard Jones Potential (LJP) in the advection equation to repair particle fracture occurring in SPH method due to the tendency of SPH particles to follow the stream line trajectory. This approach is named as the artificial particle displacement method.

Furthermore, the proposed method is totalized for the multiphase fluid systems and implemented accordingly. The presented model is validated by solving Laplace's law,

and square bubble deformation without surface tension whereby it is shown that the implemented SPH discretization does not produce any artificial surface tension. Then, the problem descriptions and solutions for two important hydrodynamic instabilities namely, Kelvin-Helmholtz and Rayleigh-Taylor instabilities, are provided along with their brief analytical linear stability analysis to describe the accuracy and the limitation of the numerical scheme. The long time evolution for both cases are investigated and the comparison between the simulation results and existence theories are provided in details.

Finally, we have presented a model to study the deformation of a droplet suspended in a quiescent fluid subjected to the combined effects of surface tension and electric field forces. The electrostatics phenomena are coupled to hydrodynamics through the solution of a set of Maxwell equations. The relevant Maxwell equations and associated interface conditions are simplified relying on the assumptions of the so called leaky dielectric model. All governing equations and the relevant jump and boundary conditions are discretized in space using the SPH method with improved interface and boundary treatments. Numerical results are validated by two highly credential analytical results which are frequently cited in the literature.

# Contents

<b>Acknowledgements</b>	<b>iii</b>
<b>Abstract</b>	<b>iv</b>
<b>List of Figures</b>	<b>viii</b>
<b>List of Tables</b>	<b>xiii</b>
<b>1 Introduction</b>	<b>1</b>
1.1 Motivation . . . . .	1
1.2 Numerical methods for interfacial flows . . . . .	2
1.2.1 Eulerian methods . . . . .	5
1.2.1.1 Interface capturing . . . . .	5
1.2.1.2 Surface tracking . . . . .	6
1.2.1.3 Volume tracking . . . . .	8
1.2.2 Mixed Eulerian-Lagrangian methods . . . . .	9
1.2.2.1 Segregated flow-interface treatment . . . . .	9
1.2.2.2 Integrated flow-interface treatment . . . . .	10
1.2.3 Lagrangian methods . . . . .	10
1.2.3.1 Free Lagrangian methods . . . . .	11
1.2.3.2 Meshless particle methods . . . . .	12
1.3 Computational strategy and thesis outline . . . . .	13
<b>2 Mathematical Background</b>	<b>16</b>
2.1 Mathematical primaries . . . . .	16
2.2 Dirac delta function . . . . .	17
2.3 Multi-dimensional Taylor expansions . . . . .	20
<b>3 Smoothed Particle Hydrodynamics</b>	<b>22</b>
3.1 Introduction . . . . .	22
3.2 The first and second derivative approximations . . . . .	25
3.3 Projective SPH . . . . .	27
3.4 XSPH . . . . .	29
3.5 Artificial viscosity . . . . .	30
3.6 Multiple Boundary Tangent (MBT) method . . . . .	31

---

3.7	Instabilities and their possible remedies in SPH method . . . . .	35
3.8	Initial and boundary conditions . . . . .	37
3.9	Neighbor search algorithm . . . . .	39
3.10	Numerical scheme . . . . .	40
<b>4</b>	<b>Single Phase Flows</b>	<b>45</b>
4.1	Introduction . . . . .	45
4.2	Governing equations . . . . .	48
4.3	Flow around bluff bodies . . . . .	48
4.3.1	Flow around a square obstacle . . . . .	49
4.3.2	Flow around a NACA airfoil . . . . .	53
4.3.3	Conclusion . . . . .	64
<b>5</b>	<b>Two Phase Flows</b>	<b>66</b>
5.1	Introduction . . . . .	66
5.2	Governing equations . . . . .	66
5.3	Interface treatment . . . . .	67
5.4	Benchmarking . . . . .	70
5.4.1	Square-droplet deformation . . . . .	70
5.4.2	Laplace's law . . . . .	72
5.4.3	Square droplet . . . . .	74
5.5	Kelvin-Helmholtz instability . . . . .	76
5.5.1	Introduction . . . . .	76
5.5.2	Definition of the problem . . . . .	77
5.5.3	Linear stability analysis . . . . .	79
5.5.4	Discussion . . . . .	81
5.5.5	Conclusions . . . . .	90
5.6	Rayleigh-Taylor instability . . . . .	91
5.6.1	Introduction . . . . .	91
5.6.2	Definition of the problem . . . . .	91
5.6.3	Linear stability analysis . . . . .	93
5.6.4	Discussion . . . . .	96
5.6.5	Conclusions . . . . .	105
<b>6</b>	<b>ElectroHydrodynamics</b>	<b>108</b>
6.1	Introduction . . . . .	108
6.2	Mathematical Formulation . . . . .	109
6.2.1	Mechanical balance laws of continua . . . . .	109
6.2.2	Electrohydrodynamics Balance Laws . . . . .	110
6.2.3	Leaky dielectric model . . . . .	114
6.3	Results . . . . .	115
6.4	Conclusion . . . . .	126
<b>7</b>	<b>Future Works</b>	<b>128</b>
<b>A</b>	<b>First and second order approximations</b>	<b>131</b>
<b>B</b>	<b>Publications</b>	<b>135</b>

# List of Figures

1.1	Eulerian and Lagrangian representation of fluid flow equations. . . . .	3
1.2	(left) interface-capturing Eulerian method; (center) surface-tracking Eulerian method; (right) volume-tracking Eulerian method. . . . .	7
1.3	Arbitrary Lagrangian-Eulerian (ALE) method with interface-tracking. . .	9
1.4	(left) Strictly Lagrangian interface-tracking; (center) Free Lagrangian interface-tracking; (right) Lagrangian meshless SPH method. . . . .	11
2.1	(left) Unit step function $H(x)$ , (right) shifted unit step function $H(x - a)$ and (center) window function $\bar{W}(x - x_o, \varepsilon)$ . . . . .	18
3.1	The schematic representation of Helmholtz-Hodge decomposition on a divergence free subspace. . . . .	29
3.2	Boundary treatment for a submerged thin object: (a) step-1, and (b) step-2.	32
3.3	Boundary treatment for a submerged thin object; (a): step-3 and (b): step-4. . . . .	34
3.4	The sketch of the channel for which fully periodic condition is imposed in the horizontal direction. Particles denoted by $\triangleright$ are the imaginary copies of those designated by $\blacktriangleright$ while particles represented by $\triangleleft$ are the imaginary copies of those shown by $\blacktriangleleft$ . . . . .	38
3.5	Schematic illustration of neighbor searching algorithm. . . . .	40
4.1	The comparison of (up) ISPH, (center) FEM and (down) WCSPH simulation results in terms of the contours of the velocity magnitude ( $m/s$ ) for (a) $Re = 100$ and (b) $Re = 200$ . . . . .	50
4.2	The comparison of (up) ISPH, (center) FEM and (down) WCSPH pressure contours for (a) $Re = 100$ and (b) $Re = 200$ , where pressure unit is Pascal ( $pa$ ). . . . .	51
4.3	The comparison of a full period of vortex shedding velocity contours obtained with (up) ISPH, (center) FEM and (down) WCSPH for the Reynolds number of 320. . . . .	52
4.4	The velocity fields in terms of velocity magnitudes over the airfoil (with an angle of attack of $5^\circ$ at Reynolds number of 420) computed on three different sets of particles by the WCSPH method, namely $150 \times 62$ (coarse), $300 \times 125$ (intermediate) and $400 \times 167$ (fine), for which results are given from top to bottom, respectively. . . . .	55
4.5	The comparison of (up) ISPH, (center) FEM and (down) WCSPH velocity contours for the angle of attack of $5^\circ$ at (a) $Re = 420$ and (b) $Re = 570$ . .	56
4.6	The comparison of (up) ISPH, (center) FEM and (down) WCSPH velocity contours for the angle of attack of $15^\circ$ at (a) $Re = 420$ and (b) $Re = 570$ .	57

4.7	The comparison of pressure envelopes for the angle of attack of $15^\circ$ at (a) $Re = 420$ (left) and (b) $Re = 570$ (right). . . . .	58
4.8	The comparison of total forces on the upper and lower cambers of the airfoil for the angle of attack of $15^\circ$ at $Re = 420$ . . . . .	59
4.9	The comparison of the components of the velocity gradient on the upper camber of the airfoil with the angle of attack of $15^\circ$ at $Re = 420$ . . . . .	60
4.10	The close-up view of particle positions around airfoils with the angle of attack of $15^\circ$ at (a) $Re = 570$ and (b) $Re = 1400$ for ISPH (up) and WCSPH (down) methods, respectively. . . . .	61
4.11	The close-up view of particle positions around airfoils with the angle of attack of $5^\circ$ at $Re = 300$ without using the APD method for (a) ISPH and (b) WCSPH methods. . . . .	62
4.12	(a) The density contours and (b) corresponding particle distributions (right) around the airfoils obtained with the WCSPH method with the angle of attack of $5^\circ$ at $Re = 1000$ . . . . .	63
4.13	The comparison of vortex shedding contours produced by (up) WCSPH and (down) FEM methods for the angle of attack of $5^\circ$ at $Re = 1400$ . . . . .	64
5.1	Replacing the sharp interface between two fluids with the transition region of finite thickness. . . . .	68
5.2	The initial (a) $t = 0(s)$ and the final (b) $t = 1(s)$ shapes of the square-droplet problem with thin interface. . . . .	71
5.3	Interface curvature versus droplet radius and the form of the Dirac delta function at the final time ( $t = 1(s)$ ) for the square-droplet deformation problem; (a) thick interface, (b) thin interface. . . . .	72
5.4	(a) Initial particle distribution for the circular droplet (fluid-2) surrounded by the background fluid (fluid-1) (b) pressure field for the over all domain. The particle resolution is $100 \times 100$ . . . . .	74
5.5	The locations of the spurious currents in the neighborhood of the interface for the particle resolutions of (a) $50 \times 50$ and (b) $100 \times 100$ . . . . .	74
5.6	(a) Initial particle distribution of a square drop of fluid 2 surrounded by fluid 1 (b) the particle distribution for the same problem after 1s. . . . .	75
5.7	Configuration of Kelvin-Helmholtz instability at initial time, $t = 0$ . . . . .	78
5.8	Time evolution of the interface in the two-dimensional KHI problem for the density ratio of ( $\rho_2/\rho_1 = 2$ ), and $\alpha = 0.001$ at $Ri = 0.01$ , which is given between dimensionless time $t^* = 0.25$ and $t^* = 4.0$ with a time interval of $\Delta t = 0.25$ . The time step increment is from left-to-right for each row. . . . .	82
5.9	Time evolution of the interface in the two-dimensional KHI problem for the density ratio of $\rho_2/\rho_1 = 2$ at various $Ri$ numbers; (a) $t^* = 0.5$ , (b) $t^* = 1.0$ , (c) $t^* = 1.5$ , (d) $t^* = 2.0$ ; ( $\alpha = 0.001$ ). . . . .	83
5.10	Time evolution of the interface in the two-dimensional KHI problem for the density ratio of $\rho_2/\rho_1 = 5$ at various $Ri$ numbers; (a) $t^* = 0.5$ , (b) $t^* = 1.0$ , (c) $t^* = 1.5$ , (d) $t^* = 2.0$ ; ( $\alpha = 0.001$ ). . . . .	84
5.11	Time evolution of the interface in the two-dimensional KHI problem for the density ratio of $\rho_2/\rho_1 = 10$ at various $Ri$ numbers; (a) $t^* = 0.5$ , (b) $t^* = 1.0$ , (c) $t^* = 1.5$ , (d) $t^* = 2.0$ ; ( $\alpha = 0.001$ ). . . . .	85
5.12	Growth rate ( $\gamma$ ) of the KHI in the linear regime for various $Ri$ numbers and density ratios( $Ri$ numbers are based on surface tension; $\alpha = 0.001$ ). . . . .	86

5.13	Effect of stabilizing forces on the growth rate ( $\gamma$ ) of the KHI in the linear regime ( $\rho_2/\rho_1 = 10$ ; $\alpha = 0.01$ ). . . . .	87
5.14	Effect of the artificial viscosity coefficient $\alpha$ on the growth rate ( $\gamma$ ) of the KHI in the linear regime ( $\rho_2/\rho_1 = 10$ ). . . . .	88
5.15	Time evolution of the interface in the two-dimensional KHI problem for the density ratio of ( $\rho_2/\rho_1 = 10$ ), and $\alpha = 0.01$ at $Ri = 0.01$ , which is given between dimensionless time $t^* = 0.25$ and $t^* = 6.0$ with a time interval of $\Delta t = 0.25$ . The time step increment is from left-to-right for each row. . . . .	89
5.16	(a) Initial particle distribution for Rayleigh-Taylor instability (b) The zoom view of initial particle distribution for half of the interface. The particle resolution is $80 \times 320$ . . . . .	92
5.17	The schematic of two layer of fluid where the heavy fluid '2' is initially above the light fluid '1' (a) before initial disturbance, and (b) after initial disturbance. . . . .	94
5.18	The dependence of the linear growth rate $\gamma$ , of a disturbance on its stability parameter, $\phi$ , for the Atwood number of $A_T = 1/3$ . The dashed-dotted and dashed lines show two roots for the analytical approximation ( $\gamma_{x1}$ , $\gamma_{x2}$ ), the dotted line is exact theoretical result ( $\gamma_e$ ), and the solid line with the symbol inside is for numerical simulation ( $\gamma_n$ ). . . . .	97
5.19	The stability parameter dependency of the fluid interface of the single mode perturbation Rayleigh-Taylor instability for the Atwood number of $A_T = 1/3$ at dimensionless time of $t^* = t(g/H)^{0.5} = 9$ . The left hand side of each sub figures presents particle distributions whereas the right hand side indicates the contour plots of the color function for the stability parameter values of (a) $\phi = 0.0$ , (b) $\phi = 0.2$ , (c) $\phi = 0.6$ , (d) $\phi = 0.9$ , and (e) $\phi = 1.1$ . . . . .	98
5.20	Time evolution of the fluid interface of the single mode perturbation Rayleigh-Taylor instability for the Atwood number of $A_T = 1/3$ and the stability parameter of $\phi = 0.0$ . The left panels of each sub figures show particle distributions while the right panels illustrate contour plots of the color function for dimensionless times of (a) $t^* = 1.8$ , (b) $t^* = 2.6$ , (c) $t^* = 5.4$ , (d) $t^* = 7.2$ , and (e) $t^* = 9.0$ . . . . .	99
5.21	Time evolution of the fluid interface of the single mode perturbation Rayleigh-Taylor instability for the Atwood number of $A_T = 1/3$ and the instability parameter of $\phi = 0.4$ . On the left panels are given particle distributions while on the right panels are presented contours of the color function for dimensionless times of (a) $t^* = 1.8$ , (b) $t^* = 2.6$ , (c) $t^* = 5.4$ , (d) $t^* = 7.2$ , and (e) $t^* = 9.0$ . . . . .	100
5.22	Time evolution of velocity fields of the Rayleigh-Taylor instability for the Atwood number of $A_T = 1/3$ and the stability parameter of $\phi = 0.0$ . The left hand sides of sub figures denote velocity vectors while the right hand sides show velocity contours ( $m/s$ ) (the interval between contours is 0.02) for the dimensionless time of (a) $t^* = 1.8$ , (b) $t^* = 2.6$ , (c) $t^* = 5.4$ , (d) $t^* = 7.2$ , and (e) $t^* = 9.0$ . . . . .	101

5.23	Time evolution of velocity fields of the Rayleigh-Taylor instability for the Atwood number of $A_T = 1/3$ and the stability parameter of $\phi = 0.4$ . The left hand sides of sub figures denote velocity vectors while the right hand sides show velocity contours ( $m/s$ ) (the interval between contours is 0.02) for the dimensionless time of (a) $t^* = 1.8$ , (b) $t^* = 2.6$ , (c) $t^* = 5.4$ , (d) $t^* = 7.2$ , and (e) $t^* = 9.0$ . . . . .	101
5.24	(a) The y-coordinate positions and (b) the velocities of the tip of the rising fluid (bubble) versus dimensionless time at the Atwood number of $A_T = 1/3$ for various stability parameters, namely, $\phi = 0.0, 0.2, 0.6, 0.9$ , and $1.1$ . . . . .	102
5.25	(a) The y-coordinate positions and (b) the velocities of the tip of the falling fluid (spike) versus dimensionless time at the Atwood number of $A_T = 1/3$ for various stability parameters, namely, $\phi = 0.0, 0.2, 0.6, 0.9$ , and $1.1$ . . . . .	103
5.26	The Froude number of the rising fluid (bubble) versus dimensionless bubble tip position at the Atwood number of $A_T = 1/3$ . The solid and the dashed lines are the analytical solutions proposed by Goncharov [52] and Abarzi [1] respectively, and the square and circle points represent the simulation results for the values corresponding to stability parameters $\phi = 0.0$ , and $\phi = 0.2$ respectively. The dimensionless bubble tip position is calculated as $h_b^* = h_b/\lambda$ . . . . .	103
5.27	Particle convergence for a test case with the Atwood number of $A_T = 1/3$ and the instability parameter of $\phi = 0.4$ on three different sets of particles (i.e., $60 \times 240$ (coarse), $80 \times 320$ (intermediate), and $120 \times 480$ (fine)); (a) the interface position at dimensionless time of $t^* = 4.5$ , and (b) the y-coordinates of the tip of the falling (spike) and rising (bubble) fluid versus dimensionless time . . . . .	104
5.28	The different initial particle distributions namely, (a) cubic, (b) staggered, (c) radially-centered, and (d) radially-off-centered, and in sub figures (e), (f), (g) and (e) are given the evolutions of the fluid interface of the single mode RTI for the Atwood number of $A_T = 1/3$ at dimensionless time of $t^* = t(g/H)^{0.5} = 5.4$ calculated correspondingly on the grids in sub figures (a), (b), (c) and (d).It is noted that sub figure (e) has the lowest initial disturbance amplitude (0.044) and highest tip position with respect to the bottom wall of the domain which might explain the lag in the presented position of the tip of the spike. . . . .	106
6.1	The comparison of numerically computed pressure jumps as a function of surface tension coefficient with that calculated by the analytical equation, namely, Laplace's law. . . . .	116
6.2	The schematic of the problem domain. Upon setting an electric potential at the upper and lower horizontal boundaries, a constant electric field in the downward direction is obtained in the model domain. . . . .	118
6.3	Schematics for two types of induced flow: (a) $Q < S$ and (b) $Q > S$ . . . . .	119
6.4	(a) The relation between the permittivity and the conductivity ratios: (b) $Q > S, f_{d,F} > 0$ ; (c) $Q < S, f_{d,F} < 0$ ; and (d) $Q < S, f_{d,F} > 0$ . Only a half of the central regions are displayed; different particle shape and size are also shown to indicate the fluid-fluid interfaces and drop deformations. . . . .	121

- 
- 6.5 The variation of droplet deformation parameter  $D$  as a function of (a) the electric field strength  $E_o$ , (b) the permittivity  $\varepsilon_1^E$ , (c) the initial droplet radius  $r_o$ , and (d) the reciprocal of the surface tension  $1/\sigma$ . . . . . 123
- 6.6 The profiles for the components of the velocity profile and their comparison with analytical results (a) for the case of  $\theta = 0$ , (b) for the case of  $\theta = \pi/4$ . This figures are generated from the simulation with input parameters provided in the forth row of Table6.1 after the steady state has been reached. . . . . 125
- 6.7 (a) Particle position distribution, and (b) velocity vectors, for different particle resolutions of  $60 \times 60$ ,  $80 \times 80$ ,  $100 \times 100$ , and  $120 \times 120$ . . . . . 126

# List of Tables

4.1	The computational cost in terms of the CPU time for the coarse, intermediate and fine particle numbers for one second of the real simulation time for the ISPH and WCSPH method. The reported unit is second. . .	56
4.2	The lift and drag forces acting on the airfoil with the angle of attack of $15^\circ$ at $Re = 420$ and $Re = 570$ . . . . .	60
5.1	The $L_1$ and $L_2$ norms of velocity magnitude after the first time step. . . .	75
6.1	The comparison of SPH and theoretical results (Eqs. (6.25) and (6.27)) in terms of the discriminating function $f_d$ and the deformation parameter $D$ for different combinations of conductivity and permittivities. . . . .	120

# Chapter 1

## Introduction

### 1.1 Motivation

Predicting the behavior of fluid is possible in two general ways namely, experimental and theoretical, where each one has its own advantages and disadvantages and generally these two approaches are complementary. Hitherto, experimental approaches are widely considered as the main source of information for predicting the physical behavior of the problems at hand. However, due to the complexities in fluid behavior especially regarding multi-phase flows and also the small time and length scales in such flows, experimental means become either extremely expensive or in some cases impossible. Under these constraints, scrutinizing the physical phenomenon seems to be possible only with having theoretical tools as alternative at hand.

In the theoretical study of a problem, the first issue is to determine the problem's physical influence parameters and the importance of each of these parameters on the given problem. Based on this physical model, a mathematical model can be introduced and formulated which is composed of a set of equations and relations that can virtually capture all of the fluid behaviors qualitatively and quantitatively. To solve these equations, the analytical or numerical method or a combination of these two methods can be used. However, there are many issues that on one hand have of great practical importance, and on the other hand the analytic solutions for them are very complex (or virtually impossible). In these circumstances using numerical methods as the only possible solution

are considered in the theoretical prediction of phenomena. Due to this, Computational Fluid Dynamics (CFD) branch is primarily expanded.

In this introduction section, we concisely present the most famous and frequently used numerical methods in literature for the numerical simulation of interfacial flow and elaborate on their differences, similarities, advantages and drawbacks. As such, why Smoothed Particle Hydrodynamics (SPH) method has been chosen and investigated for the numerical modeling of multiphase flow within the scope of this dissertation would be substantiated. The correct treatment of difficulties inherent to numerical modeling of fluid flow system is essential for determining the success of the entire method. These intrinsic are: (i) the method should correctly and effectively models the physical boundary condition (i.e. solid walls); (ii) it should conserve the mass (iii) it should realistically treat the complicated physical interfacial phenomena such as folding, merging and/or break-up; (iv) it should properly take the interfacial jump condition into account (i.e. large density and viscosity ratios); (v) the influence of surface tension force should be accurately evaluated and inserted into the model; and finally (vi) it should be easily extendable to deal with more complicated phenomena such as those in Electrohydrodynamics' problems. Furthermore a good methodology should lend itself to three-dimensional modeling and massively parallel computing in order to handle the real life problems.

## 1.2 Numerical methods for interfacial flows

Multiphase flow where two or more fluids have interfacial surfaces is one of the challenging and difficult areas in the field of CFD, which plays an important role in many industrial and natural systems such as cavitation, boiling heat transfer, air entrainment at ocean surfaces and bubble reactors, among others. Nevertheless, because of the complexity of these problems mainly associated with the necessity of finding precise interface evolution, most of the early works have not gone beyond simple problems. As can be inferred, the interface evolution is crucial to the modeling of multiphase flows and thus, needs to be modeled correctly and studiously in order to obtain reliable simulation results.

The ongoing attempts of modeling free surface/interfacial fluid flows resulted in the availability of a numerous amount of papers with different numerical approaches. This can be easily observed by reviewing Anderson et al. [4], Cuvelier and Schulkes [27], Floryan and Rasmussen [43], Hou [66], Scardovelli and Zaleski [133], Tsai and Yue [160] and Shyy et al. [141].

Numerical methods for fluid flow can be categorized into three distinct classes based coordinate system utilized, namely, Eulerian, Lagrangian and mixed Eulerian-Lagrangian. Eulerian methods generally employ a reference coordinate system wherein fluid properties are transmitted from one cell into another. In Lagrangian methods unlike Eulerian methods, moving coordinate system is utilized whereby the fluid elements (can be represented by numerical cells or particle) move along the fluid motion while containing identical fluid species (see Fig. 1.1). In between, mixed Eulerian-Lagrangian are the numerical schemes that employ both Eulerian and Lagrangian concepts. The above mentioned classification does not contain any information about the interface motion modeling; however it reasonably describes the fluid flow modeling. In this respect, when a fluid interface is considered, and due to the importance of interface modeling, it is crucial to take into account a new classification which divides simulations into interface-tracing and interface-capturing approaches. The difference between these two approaches relies on the construction of the interface. The interface is generated by tracking fluid trajectories in a Lagrangian field or mixed Eulerian-Lagrangian for the interface-tracking method while in the interface-capturing approach, the interface is constructed by fluid properties such as density or fluid volume fraction.

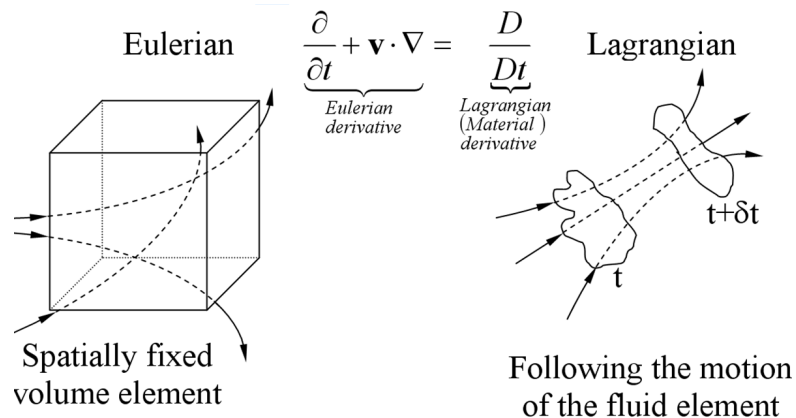


FIGURE 1.1: Eulerian and Lagrangian representation of fluid flow equations.

To gain an insight into any particular computational technique for multiphase flows knowing the following three distinguished common parts, i.e. (i) flow modeling, (ii) interface treatment, and (iii) flow-interface coupling, seems to be sufficient. However, in addition to these information, spatial discretization schemes, and the flow equation solver need to be considered. The former deals with the algorithmic component and representation of the flow equations which influences the interface representation while the latter deals with different strategies to overcome nonlinear difficulties that come from the nature of fluid flow equations.

Because both the flow-interface coupling and flow equation solver contain difficulties that include but not restricted to nonlinearities, restrictions and singularities, they are the bottle-neck parts of simulations and thus need strategies in order to deal with complicated fluid flows. These strategies can mainly be obtained by two different approaches, namely "integrated" and "segregated". For the flow-interface coupling in the segregated approach, the flow is first simulated with the determinant interface and, then, a new position of the interface is found using the last computed flow variables, while the integrated approach tends to evaluate the flow properties and interface position simultaneously. On the other hand, the segregated flow equation solver carries the concept of separate solution of all or parts of the flow such as fluid incompressibility, viscous diffusion and *etc.*, while the integrated approach solves the flow sets of equations all together.

Considering the main attributes of a numerical modeling procedure for free surface/interface flows, a general form of classification can be achieved as [143]

1. Flow modeling: Eulerian, Lagrangian, mixed Eulerian-Lagrangian, mapping Method.
2. Interface modeling: capturing, tracking.
3. Flow-interface coupling: integrated, segregated.
4. Spatial discretization: FDM, FVM, FEM, meshless, others.
5. Flow equations solver: integrated, segregated.

Now, one may find various schemes in literature by amalgamation of all reviewed approaches, strategies and methods above. In the following, the most popular schemes are briefly introduced.

### 1.2.1 Eulerian methods

In the scope of Eulerian methods, it is possible to make use of either interface-capturing or interface-tracking approach. On the other hand, the interface-tracking approach can be decomposed into two categories namely, surface-tracking and volume-tracking techniques. In the following sections, the three combinations of Eulerian methods will be discussed.

#### 1.2.1.1 Interface capturing

In the interface-capturing methods the interface is represented as either by a discontinuity line of some characteristic function or a zero-level set of some implicit function by reconstructing from the properties of some suitable field variables such as fluid fractions or density (Fig. 1.2, left). The former method called the "discontinuous approach" while the later one known as the "continuous approach". Either function expresses that the interface is a material line propagating with the fluid and it follows pure transport equation. The term "interface-capturing" comes from the fact of recovery of the interface from current distribution of that field variable.

**Discontinuous approach:** The volume-of-fluid (VOF) method, introduced by Hirt and Nichols [64], can be named as the first and the main algorithm from discontinuous approach family. This method defines a discontinuous line as the discontinuity function which is equal to unity at any point occupied by one of the fluids for a two-fluid flow system and zero elsewhere; and should satisfy the pure convection equation; and advect with the fluid velocity.

Two main steps of the VOF-type of algorithm are: (i) the propagation and (ii) the reconstruction. Since the former one introduces a serious problem for numerical method and the later one affect the viscous stress and surface tension forces' approximation at the interface (calculated from the location, orientation and curvature of the interface), both of these steps should be applied with a great care. Furthermore, it is noted that the initially proposed first-order accuracy in determining the interface location, which uses the simple line interface calculation (Noh and Woodward [107]) method, can be promoted to the second-order accuracy by implying the piecewise linear interface construction method (Rudman [128], Rider and Kothe [125], Ashgriz and Poo [7]).

The main advantages of the VOF interface-capturing methods are: (i) easy treatment of reconnection or merger of interfaces, (ii) mass conservation in a natural way, and (iii) easy extendibility to three-dimensional problems. The major disadvantages of the methods can be named as: (i) the advection of discontinuous VOF-function, (ii) the complexities in determining the exact interface' location, normal and curvature, (iii) numerical gauming of the interfacial boundary conditions as well as the interface details.

**Continuous approach:** Although in principle it shares similarities to that of the discontinuous-capturing framework (for instance, coupling flow-interface in a segregated manner, and approximating the spatial derivatives on a fixed grids), the continuous approach represents the interface as a zero level set of some continuous functions.

Defining a zero level set of a continuous "pseudo-density" function, and integrated using finite element method for the solution of flow equations, the paper by Dervieux and Thomasset [30] seems to be the first work in the scope of continuous interface-capturing algorithms. Later, The continuous interface-capturing has been divided into two distinguished groups: (i) "pseudo-concentration" function notion (Thompson [154], Dhatt et al. [31], Lewis and Ravindran [86]) and (ii) level-set approach (Osher and Sethian [111], Sussman et al. [145], Sussman and Smereka [144]).

Although, partake the strength in handling multiple interfaces and the expandability to three-dimension with the VOF method, the discontinuous interface-capturing representation of the interface gives two immediate advantages over it; which are: (i) the simpler interface convection problem of a continuous function comparing to a discontinuous one and (ii) the more convenient interpretations for the normal and curvature at interface. On the other hand, three major drawbacks of the discontinuous approach can be count as: (i) inaccurate defining of the interface position, (ii) numerical gauming of the interfacial boundary information, and (iii) worse mass conservation comparing to VOF-type methods.

### 1.2.1.2 Surface tracking

In the surface tracking methods, the interface is represented by a series of interpolated curves through a discrete set of points on the interface. After saving the information about the points' location and their sequence at each time step, the points will be moved

according to an interface evolution equation. Thus, the Lagrangian motion of particles in interface-tracking methods is the key point in the interface-tracking approach, which is in contrast to the advection of some field variables through fixed Eulerian grid in the interface-capturing methods.

In this method the interface information including its location, orientation and curvature are explicitly available at any time during the simulation process. Two general forms of surface-tracking methods exist: (i) the points are given as heights above a reference line or (ii) using a parametric representation (Fig. 1.2, center). There might be a failure in the first approach, if the interpolated curve becomes multi-valued, which strongly limits a practical utility of this method.

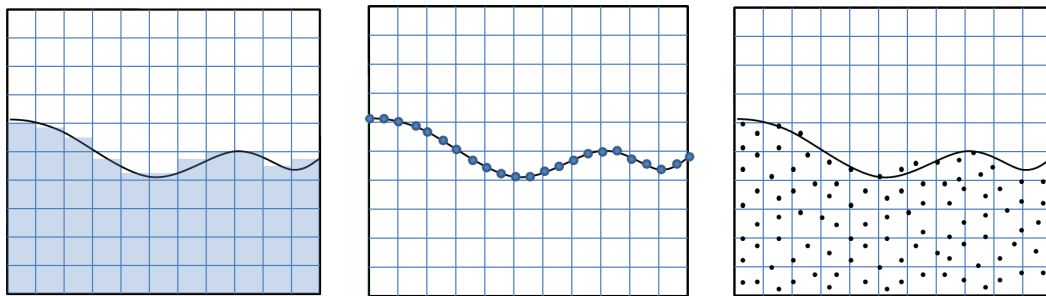


FIGURE 1.2: (left) interface-capturing Eulerian method; (center) surface-tracking Eulerian method; (right) volume-tracking Eulerian method.

The ability to resolve features of the interface that are smaller than the cell spacing of the overlaid Eulerian grid can be named as the main advantage of surface-tracking methods. However, this method has two main disadvantages namely: (i) difficulties in interfaces' folding and merging (needs interface's points reordering and as consequences it requires computational overhead and complex logical programming) and (ii) the interface points accumulation in one part of the computational domain may leave the other parts unresolved.

The paper by Hyman [73] is a comprehensive reference for the overview of early works on surface-tracking methods. Later on, using surface-tracking approach, Glimm et al. [49, 48] employed a finite element approximation with locally adaptive grid; and Tryggvason et al. ([161, 38, 39]) proposed some specific algorithm to treat interface merging in 3D where they employed the finite difference method along with segregated approach for the system of flow equations. More recently one may name, another algorithm for handling interface topology changes in the work by Shyy et al. [141], and the finite volume

and the finite element discretization used by Popinet and Zaleski [113] and Tornberg [156] respectively. In all above mentioned works, the calculations of flow variables are computationally segregated from tracking of the interface.

### 1.2.1.3 Volume tracking

In the volume-tracking methods, the interface is reconstructed when it is necessary and they do not store its representation. The presence of marker quantity within the cell is the key point of interface reconstruction (it is used to reconstruct the interface cell by cell). The notion of volume-tracking comes from the fact that the marker particles, which are used to show which cells contain a particular fluid, are moved in a purely Lagrangian manner (Fig. 1.2, right).

The marker-and-cell (MAC) method is the first Eulerian volume-tracking algorithm for free-surface flows (Harlow and Welch [58]). In this approach, a fixed uniform mesh along with finite difference method is used to approximate the flow equations and then resolved it in a segregated fashion using either a pressure Poisson equation or velocity/pressure-correction algorithm (Bulgarelli et al. [14]).

The main advantages of the method are: (i) it can treat multi-fluid flow systems, (ii) it can easily handle large interface deformation, and (iii) it can model interfaces' break-up and merging; on the other hand, the problems associated with the method are as follows: (i) no details are given regarding to the precise interface' location, orientation, and curvature in this method, (ii) the particle accumulation in one portion of the computational domain may leave the other portions not well resolved or even unresolved, (iii) it has some difficulties for imposing the interfacial boundary conditions, and (iv) since it needs a double grid system for both Eulerian and marker particles, the method is expensive in terms of computational costs.

Despite its weaknesses, and due to its flexibility in treating large interfacial deformations and its logical simplicity, the MAC method has become very popular among scientist; later, the approach were strengthened and extended by implementing the pressure correction segregated algorithm (Hirt and Cook[62]), the efficient algorithm for accurate treatment of fluid convection (Ramshaw and Trapp [122]), and the presentation of the improved algorithm for interface reconstruction respectively (Noh and Woodward [107]).

## 1.2.2 Mixed Eulerian-Lagrangian methods

### 1.2.2.1 Segregated flow-interface treatment

The arbitrary-Lagrangian-Eulerian (ALE) algorithm proposed by Hirt et al. [61] is one of the most cited early papers within the Eulerian-Lagrangian framework. The numerical algorithm for this method can be divided into three distinct phases; (i) an explicit Lagrangian calculation without moving the mesh vertices (ii) an implicit iterative velocity and pressure fields' adaptation for the new time level, followed by the mesh vertices movement to their new position, and (iii) a mesh rezoning for a new configuration (Fig. 1.3).

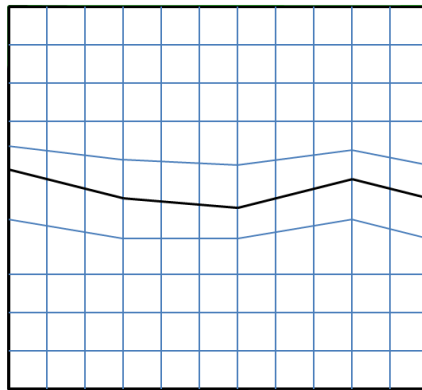


FIGURE 1.3: Arbitrary Lagrangian-Eulerian (ALE) method with interface-tracking.

The last phase is arbitrary as it may be required for moving fluid flow and interface of highly deformations by following Lagrangian principles, or may be fixed for small deformations (Eulerian principles). Thus by following the Lagrangian motion of vertices which are initially aligned with the interface the interface can be tracked. Sharing the same main advantages and drawbacks, as far as the treatment of the interface is concerned, this algorithm has remarkable similarities with conventional Lagrangian rezoning methods. In particular, the significant shortcoming can be reported as limited interface deformations due to the necessity of maintaining a fixed topology of the grid.

Nonetheless, the ALE-type methods are attractive for interfacial flows due to their flexibility in mesh vortices' motion. This algorithm were successfully implemented by Bansch [8], Belytschko and Flanagan [10], Donea et al. [33], Hughes et al. [72], Ramaswamy and

Kawahara [121]. All these works relied on the finite-element method and on the segregated treatment of flow-interface coupling. Examples of ALE methods for the integrated solver for the systems of flow equations are Tezduyar et al. [152, 153] and Hansbo [57], where space-time finite-element method was combined with least-squares type stabilization. Although simulation results obtained with diverse ALE-based algorithms are very good, the changes of interface topology lie beyond the method capabilities and especially in three-dimension the implementation seems to be rather complex.

### 1.2.2.2 Integrated flow-interface treatment

Proposed by Ruschak [129] and Saito and Scriven [131], a group of Lagrangian-Eulerian concept of mesh movement on the fully coupled (integrated) manner for the "flow variable-interface" systems was introduced. Although it is initially introduced for steady free-surface flows, later on, it has been extended to unsteady flows with free moving boundaries in works by Christodoulou and Scriven [22], Engelman and Sani [35], Kheshgi and Scriven [77], Cuvelier [26]. In this approach, after the discretization of flow equations with their corresponding interfacial boundary conditions as a whole with respect to the flow variables and to some functional representation (parametrization) of the interface, the nonlinear algebraic equations are solved benefiting from any iterative procedure such as Newton or quasi-Newton ones. Comparing to segregated methods, the fast quadratic convergence rate towards the steady-state solution is obtained. However, there remain some uncertainties for purely transient problems: (i) considering the lacks in the solution uniqueness for certain ranges of physical parameters, should the iterative process within each time step always converge to some "fixed point"?, (ii) the ways that a good initial approximation for the Newton iteration is chosen, (iii) how to determine the Jacobian matrix of discrete nonlinear operator efficiently, and (iv) since the time discretization error of the entire process usually dominates, does it really make sense to treat the "flow variables-interface" coupling so accurately on each time step?

### 1.2.3 Lagrangian methods

In the Lagrangian methods, the fluid elements originally represented by mesh are allowed to move and deform. The Lagrangian methods are inherently combined with interface-tracking approaches, holding the benefits of: (i) precise tracking and the delineation of

material interface, (ii) easily applying the interface boundary conditions and (iii) the absence of nonlinear convective term in the momentum equation. However, the mesh may get extensively distorted and in turn acquire highly irregular shape (Fig. 1.4, left) hence leading to the numerical inaccuracy. Therefore, the Lagrangian interface-tracking methods in their original form (the mesh based Lagrangian approach) are conventionally suitable to handle small interfacial deformation. An appropriate reference is the article of Hirt et al. [63], where the segregated approach for flow equations solver together in combination with the finite-volume approximation was used. Kawahara et al. ([59], [110]) and Shopov et al. [140] also proposed employed the purely Lagrangian flow description with interface-tracking and improved the finite-element method (FEM) together with fractional-step segregated and integrated algorithm respectively.

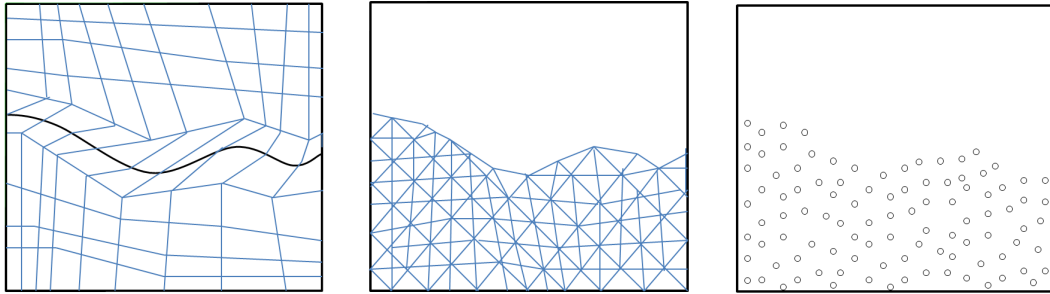


FIGURE 1.4: (left) Strictly Lagrangian interface-tracking; (center) Free Lagrangian interface-tracking; (right) Lagrangian meshless SPH method.

### 1.2.3.1 Free Lagrangian methods

Attempts are made to improve the Lagrangian methods by decreasing the effects of severe mesh distortion and resulted into two approaches: remeshing algorithms and meshless particle methods. In the remeshing approach, also called free Lagrangian methods, a new mesh will be build in conjugate with the scrambled mesh; then, using any arbitrary interpolation, the information will be transferred from the old distorted mesh to the new one. Having in mind the change in the interface topology, the remeshing procedure may need mesh point addition, deduction and/or reconnection (Fig. 1.4, center). The notion of free Lagrangian method also came from this later way of remeshing. As appropriate references in this framework one may mention the works done by Fyfe et al. [45], Fritts and Boris[44] and Crowley [24].

Although at the first glance they seem to be suitable for the moving interfacial problems, the grid-based Lagrangian methods have three critical drawbacks: (i) the remeshing algorithm is computationally expensive (ii) the large changes in the interface topology only can be modeled using some complex algorithms and (iii) performing frequent remeshing may be severely unreliable, especially in three dimensions.

### 1.2.3.2 Meshless particle methods

Using meshless particle methods is the second popular approach circumventing the mesh tangling problem. In this method grid is completely abandoned (Fig. 1.4, right). In this group, the discrete viscous flow is represented by replacing the conventional mesh with a finite number of particles which can carry the fluid characteristic properties such as position, mass, velocity, and other hydrodynamics properties; and the fluid system evolution is governed by interactions between these particles. The particles are explicitly associated with different materials, and thus the interface between species can be easily tracked. The Boltzmann lattice-gas algorithms can be classified in the category of particle methods (Benzi et al. [11], Rothman and Zaleski [127, 126]). Although they have a natural ability to treat the interfacial flows, these methods suffer from some uncertainties which are: (i) the concerns towards the reliability of physical models for flow viscosity and also inter-particle forces' representation and (ii) how to properly model the interfacial jump conditions with high density and viscosity ratio and in the presence of surface tension.

In the scope of meshless particle methods, Smoothed Particle Hydrodynamics is a solution towards achieving a realistic physical model for interfacial flows. Benefiting from a smoothing kernel function, physical quantities are interpolated in a discrete form (Monaghan [100], Morris [104]). Nevertheless, common to every numerical method, the standard SPH method in its current stage has also some shortcomings around: (i) accuracy of flow variable approximation as an optimized point between the interpolation accuracy and numerical diffusion, and (ii) modeling of large ratios of density/viscosity discontinuity at the interface. Additionally, particle clustering in some region may cause insufficient particle resolution in some other region and hence, comparing to grid-based Lagrangian methods, particle methods may suffer from the accurate representation of the interface.

### 1.3 Computational strategy and thesis outline

Having compared diverse numerical methods, which has provided us with a solid foundation in order to choose the basic components of our numerical modeling strategy, we choose purely Lagrangian meshless particle approach since it enables us to use movable particles on any arbitrarily computational domain. The particular advantages of having movable particles for interface resolving has been discussed in preceding section. Second, we rely on this fact that the interfaces between different materials can be easily followed in order to be able to deal with complex changes in interface topology including interface break-up, and merger phenomena.

Finally, we choose the SPH approach for spatial discretization in the present work. The main reason for this choice is its inherent strength which some of those may be found in other methods but the combination of all those features seems to be found only in SPH. These features are: (i) natural distinguishing between phases due to holding material properties at each individual particle, (ii) natural incorporation of coefficient discontinuities and singular forces into the numerical scheme, (iii) natural incorporation of derivative instead of the field properties' derivatives into the scheme, (iv) non-existence of convective term in discretization of the momentum equation in the numerical approximation scheme.

This work is original due to the following contributions:

It suggests an improved ISPH and WCSPH algorithm that include the implementation of (i) Multiple Boundary Tangent (MBT) method to treat geometrically complex solid boundaries in a flow field, (ii) the Artificial Particle Displacement (APD), particle fracture repair, procedure for eliminating particle clustering induced instabilities, and (iii) the corrective SPH discretization scheme to improve the accuracy of the computation.

Furthermore, the proposed method totalized for the multiphase fluid systems and implemented accordingly. The presented model is validated by solving Laplace's law, and square bubble deformation without surface tension whereby it is shown that the implemented SPH discretization does not produce any artificial surface tension. Then, it suggests an improved interface treatment approach which enable us to model multiphase systems with large variations in the transport parameters of constituents. This

improvement has been validated extensively through solving two complex hydrodynamic instabilities namely, Kelvin-Helmholtz and Rayleigh-Taylor instabilities.

Finally, it has presented a model to study the electrohydrodynamics problem through the solution of a set of Maxwell equations. The model is validated by solving the deformation of droplet suspended in a quiescent fluid subjected to the effect of constant electric field and comparing with established theory.

The rest of this thesis is structured as follows:

The presentation of the current work begins in chapter 2 with a brief description of the formulations, mathematical background and afterward in chapter 3 we concisely derive the first and second derivative approximations as well as briefly introduce projective SPH, XSPH, artificial viscosity, MBT treatment for complex geometry, interface treatment, instabilities and their possible remedies in SPH method, initial and boundary conditions, SPH neighbor search algorithm, and describe numerical schemes implementation consecutively.

In Chapter 4, two benchmark problems are solved for relatively high Reynolds numbers and a remedy for eliminating particle clustering-induced instabilities with the implementation of a particle fracture repair procedure as well as the corrected SPH discretization scheme is introduced. It is also shown that both general numerical schemes widely used in SPH, namely incompressible and weakly compressible SPH, are capable to produce numerical results as accurate and reliable as mesh dependent methods.

The treatment of the interface for the multiphase flow and the solution algorithm are discussed in chapter 5. The continuum surface force (CSF) model is used to include the surface tension force in the linear momentum balance equation. The results of simulations conducted for a droplet problem with the effect of surface tension force to validate the CSF model with analytical Laplace solution and a square-droplet deformation without the influence of surface tension to illustrate the nonexistence of artificial surface tension in the used SPH discretization.

In the same chapter, the problem description for the Kelvin-Helmholtz instability (KHI) is provided. An analytical linear stability analysis is performed to describe effective parameters for the KHI problem and simulation results for the KHI problem with a broad range of parameters are presented. Effect of surface tension and gravity on the KHI is

tested separately and simultaneously in details, and the effect of the  $Ri$  number on the development of instability is investigated. Afterwards, the problem description for the Rayleigh-Taylor instability (RTI) is provided along with simulation results validated by analytical linear stability analysis. The long time evolution of the RTI is also investigated and the comparison between the simulation results and existence theories are provided in details.

In Chapter 6, we numerically investigate the effect of an electric field on the neutrally buoyant droplet in a quiescent Newtonian fluid. The leaky dielectric model is used in order to account for the effects of the electric field, and electrical properties of liquids. In the leaky dielectric model, the droplet with finite electrical conductivity and with no free electrical charge is considered. Under these model assumptions, electric stresses are only supported at the droplet interface, and are absent in the bulk. The droplet interface is modeled as a transition zone with a finite-thickness across which the material properties vary smoothly, and the electric field effect is integrated into momentum balance equations as volumetric force by using the divergence of the Maxwell stress tensor. The extensive amount of computations performed has enabled us to study the complex nature of droplet dynamics under the combined effect of Maxwell stresses, surface tension, and viscous forces.

Finally, in Chapter 7 we discuss some possible directions for further research.

## Chapter 2

# Mathematical Background

### 2.1 Mathematical primaries

For the readability of this presentation, it is worthwhile to introduce the notational conventions which will be used throughout this work. The bold-faced Latin indices ( $\mathbf{i}, \mathbf{j}$ ) will denote explicitly particles and will always be placed as subscripts. For vector or tensor fields, we may use mixed notations (i.e., either direct or indices notations) to improve the readability. When direct notation is used, vector will be represented with either lower or upper case letters with an arrow placed on top while tensor fields will be denoted by upper case bold-faced letters. In the case of indices notations, italic Latin indices will be used to denote vector or tensor components and will always be placed as superscripts, except in the base vectors, where they are placed as subscripts. For example, the position vector for particle the " $\mathbf{i}$ " is  $\vec{r}_i = x_i^k \hat{e}_k$  where  $x_i^k$  component of the position vector with  $k = 1, 2, 3$  and  $\hat{e}_k$  is the base vector. The difference vector between the particles are indicated by  $\vec{r}_{ij}$  or  $\vec{r}_{ji}$ . Explicitly,

$$\vec{r}_{ij} = \vec{r}_i - \vec{r}_j = (x_i^k - x_j^k) \hat{e}_k = r_{ij}^k \hat{e}_k = -\vec{r}_{ji}. \quad (2.1)$$

Additionally, the magnitude of the difference vector  $|\vec{r}_{ij}|$  will be denoted by  $r_{ij}$ , and finally, the unit difference vector will be denoted by  $[\hat{r}_{ij}^k] = r_{ij}^k / r_{ij}$  vector of the difference.

## 2.2 Dirac delta function

Dirac delta (widely referred to as unit pulse function) is the starting point of the SPH approach. Therefore, it is prudent to introduce certain aspects of Dirac delta function without getting into unnecessary details. For the analysis of the Dirac delta function  $\delta(x - x_o)$ , it is convenient to start with introducing the unit step (Heaviside) function,  $H(x)$  which has the jump at zero as shown in Fig. 2.1. The unit step function shifted to the right by "a" (where "a" is an positive) can be written as  $H(x - a)$ . With the help of the unit step function, the integral of a continuous function over finite limits, i.e.,  $a \leq x \leq b$  can be extended over the whole  $x$ -axis

$$\int_a^b f(x)dx = \int_{-\infty}^{+\infty} f(x)[H(x - a) - H(x - b)]dx. \quad (2.2)$$

If we consider the integral of the same function between the limits  $x_o - \varepsilon/2$  and  $x_o + \varepsilon/2$ , we can write

$$\int_{x_o - \varepsilon/2}^{x_o + \varepsilon/2} f(x)dx = \int_{-\infty}^{+\infty} f(x)[H\{(x - x_o) + \varepsilon/2\} - H\{(x - x_o) - \varepsilon/2\}]dx. \quad (2.3)$$

Applying the mean value theorem to Eq. (2.3), we can write

$$\int_{-\infty}^{+\infty} f(x) \frac{[H\{(x - x_o) + \varepsilon/2\} - H\{(x - x_o) - \varepsilon/2\}]}{\varepsilon} dx = f(\xi), \quad (2.4)$$

where  $\frac{H\{(x - x_o) + \varepsilon/2\} - H\{(x - x_o) - \varepsilon/2\}}{\varepsilon}$  defines a window function denoted by  $\bar{W}(x - x_o, \varepsilon)$  (refer to Fig. 2.1 (center)) and  $\xi$  is a number between  $x_o - \varepsilon/2 \leq \xi \leq x_o + \varepsilon/2$ . If the parameter  $\varepsilon$  is sufficiently small, the window function  $\bar{W}(x - x_o, \varepsilon)$  is called as a unit impulse, since the area under the nonzero part of the graph is equal to unity. Here,  $x_o$  is the centre position of the impulse.

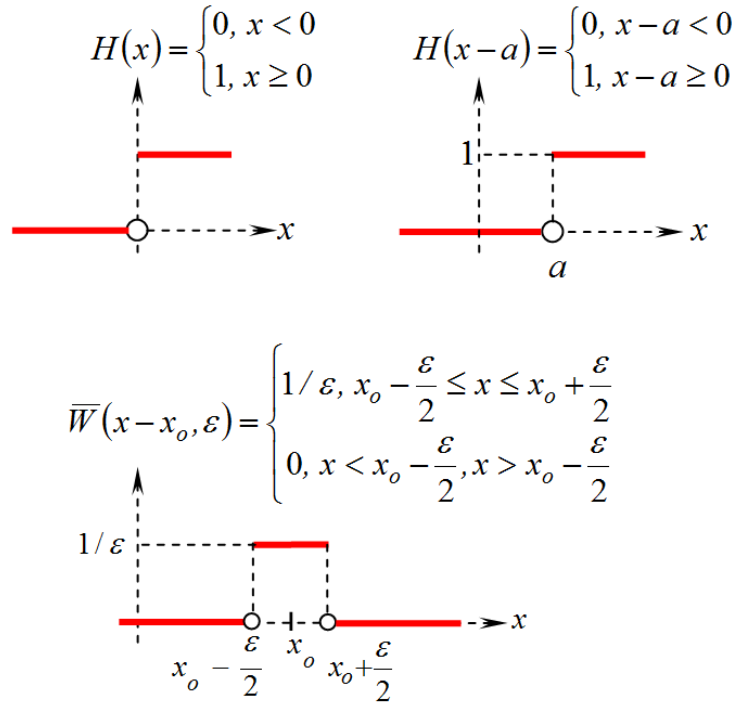


FIGURE 2.1: (left) Unit step function  $H(x)$ , (right) shifted unit step function  $H(x - a)$  and (center) window function  $\bar{W}(x - x_0, \epsilon)$ .

Taking the limit of Eq. (2.4), we can have

$$\int_{-\infty}^{+\infty} f(x) \lim_{\epsilon \rightarrow 0} \bar{W}(x - x_0, \epsilon) dx = \lim_{\epsilon \rightarrow 0} f(\xi). \tag{2.5}$$

The limit of the window function  $\bar{W}(x - x_0, \epsilon)$  as  $\epsilon \rightarrow 0$  defines a new function that is known as Dirac delta function and denoted by  $\delta(x - x_0)$ , and  $\lim_{\epsilon \rightarrow 0} f(\xi) = f(x_0)$ . Hence, Eq. (2.5) becomes

$$\int_{-\infty}^{+\infty} f(x) \delta(x - x_0) dx = f(x_0). \tag{2.6}$$

Dirac delta function has following features; (i) it is zero everywhere except when its arguments is zero, namely except when  $x = x_0$  and it approaches to infinity at  $x = x_0$ . Therefore, Dirac delta function acts like a filter through which only the value of the  $f$  at  $x = x_0$  is able to pass. It can be seen from Eq. (2.4) that Dirac delta function is the derivative of the unit step function. It is obvious to see from Fig.2.1(center) that integral of the Dirac delta function from minus infinity to plus infinity equals to

unity. This implies that delta Dirac function is an even function. Mathematically, these statements can be written as

$$\delta(x - x_o) = \begin{cases} 0, & x \neq x_o \\ \infty, & x = x_o \end{cases}, \quad \int_{-\infty}^{+\infty} \delta(x - x_o) dx = 1, \quad \delta(x - x_o) = \delta(x_o - x). \quad (2.7)$$

A function  $f(x)$  is *even* if satisfies the condition  $f(x) = f(-x)$ . Even functions are symmetric about the  $f(x)$  axis. A simple example for an even function is  $f(x) = x^2$ . A function  $g(x)$  is called *odd* if it satisfies  $-g(x) = g(-x)$ . Examples of odd functions are  $g(x) = 1/x$  and  $g(x) = x^3$ . Some of the important properties of odd and even functions that will be used in the derivations of SPH equation can be listed as; the product of an even and odd functions is odd function, and the derivative of an even function is an odd function, while the derivative of an odd function is even function. Finally, it is easy to deduce that an integration of an odd function over entire space is equal to zero; that is,

$$\int g(x) dx = 0. \quad (2.8)$$

Three dimensional Dirac delta function in Cartesian coordinates  $\delta^3(|\vec{r}_o - \vec{r}|)$  is just the product of three one-dimensional delta functions

$$\delta^3(|\vec{r} - \vec{r}_o|) = \delta(x^1 - x_o^1) \delta(x^2 - x_o^2) \delta(x^3 - x_o^3), \quad (2.9)$$

where it satisfies the condition

$$\iiint_{\Omega} \delta^3(|\vec{r} - \vec{r}_o|) d\Omega = \int_{-\infty}^{+\infty} \int_{-\infty}^{+\infty} \int_{-\infty}^{+\infty} \delta(x^1 - x_o^1) \delta(x^2 - x_o^2) \delta(x^3 - x_o^3) dx^1 dx^2 dx^3 \quad (2.10)$$

where the symbol  $\Omega$  indicates the space (differential volume) over which the integration is carried out.

In three dimensional, the corresponding relation for Eq. (2.6) is then,

$$\int_{\Omega} f(\vec{r}) \delta^3(|\vec{r} - \vec{r}_o|) d^3\vec{r} = f(\vec{r}_o). \quad (2.11)$$

This identity is an exact mathematical relationship, and is the starting point of the SPH technique.

### 2.3 Multi-dimensional Taylor expansions

In the derivation of SPH equations, we will frequently use the Taylor expansion of a scalar or vector-valued function. All continuous functions can be approximated using a Taylor series expansion. The Taylor expansion of a function  $f(x)$  with one variable about a point  $x_o$  is given as

$$f(x) = \sum_{\alpha=0}^{\infty} \frac{\delta x^{\alpha}}{k!} f^{(\alpha)}(x)|_{x=x_o} = f(x_o) + (x - x_o) f'(x_o) + \dots + \frac{(x - x_o)^{\alpha}}{k!} f^{(\alpha)}(x_o). \quad (2.12)$$

Here,  $\delta x = (x - x_o)$ ,  $\alpha$  is the summation index and the subscript on the vertical bar indicates that all the derivatives are evaluated at the point  $x_o$ . Now consider the same scalar-valued function  $f(\vec{r})$  whose argument is a position vector  $\vec{r}_o = x^1 \hat{e}_1 + x^2 \hat{e}_2 + x^3 \hat{e}_3$ . Since the position vector has three components,  $f(\vec{r})$  is a function of three variables. In vector notation (direct notation), the expansion of the function about  $\vec{r}_o$  is

$$f(\vec{r}) = f(\vec{r}_o) + ((\vec{r} - \vec{r}_o) \cdot \nabla_{\vec{r}}) f(\vec{r})|_{\vec{r}=\vec{r}_o} + \frac{1}{2} (\vec{r} - \vec{r}_o) \cdot \nabla_{\vec{r}} \nabla_{\vec{r}} f(\vec{r})|_{\vec{r}=\vec{r}_o} \cdot (\vec{r} - \vec{r}_o), \quad (2.13)$$

where the nabla operator  $\nabla_{\vec{r}}$  denotes a differentiation with respect to coordinate  $\vec{r}$ . The first order derivative of the function is a vector, and it is dotted with  $(\vec{r} - \vec{r}_o)$  to give a scalar field. The second order derivative of the function is a second order tensor, and it is dotted from both sides by  $(\vec{r} - \vec{r}_o)$  to have a scalar field; dotting a tensor from both sides is the same as taking the second-order tensor inner product, namely,  $(\vec{r} - \vec{r}_o) \otimes (\vec{r} - \vec{r}_o) : \nabla_{\vec{r}} \nabla_{\vec{r}} f(\vec{r})|_{\vec{r}=\vec{r}_o}$ . The *inner product* (also called the *double dot product*) between two second-order tensors is a scalar defined as  $\vec{a} \otimes \vec{b} : \mathbf{T} = a_i \hat{e}_i b_j \hat{e}_j : T_{kl} \hat{e}_k \hat{e}_l = a_i b_j T_{kl} \delta_{ik} \delta_{jl} = a_i b_j T_{ij}$ , where  $\delta_{ij}$  is the Kronecker delta.

From onward, two vectors multiplied side by side without any dot (ie.,  $\vec{a}\vec{b} = \vec{a}:\vec{b}$ ) is understood to be a dyadic product. Eq. (2.10) can be written in compact form as,

$$f(\vec{r}) = \sum_{\alpha=0}^{\infty} \frac{1}{n!} ((\vec{r} - \vec{r}_o) \cdot \nabla)^\alpha f(\vec{r})|_{\vec{r}=\vec{r}_o}. \quad (2.14)$$

In the component notation, a scalar valued-function  $f(\vec{r})$  of the position vector ( $\vec{r}$ ) can be written as

$$f(\vec{r}) = f(\vec{r}_o) + (x - x_o)^l \frac{\partial f(\vec{r})}{\partial x^l} |_{\vec{r}=\vec{r}_o} + \frac{1}{2} (x - x_o)^l (x - x_o)^k \frac{\partial^2 f(\vec{r})}{\partial x^l \partial x^k} |_{\vec{r}=\vec{r}_o}. \quad (2.15)$$

## Chapter 3

# Smoothed Particle Hydrodynamics

### 3.1 Introduction

Smoothed particle hydrodynamics (SPH) is a meshless Lagrangian particle method to solve partial differential equations widely encountered in the engineering problems. Unlike grid dependent technique, SPH does not require mesh since the partial derivatives in transport equations are approximated using a properly normalized distribution function (widely referred to as the Kernel function) such as Gaussian, Spline or Quantic distribution functions; hence it offers noteworthy flexibility in modeling problems involving highly irregular geometries, or where mesh break down occurs. It was initially developed by Gingold and Monaghan [46] and Lucy [94] in 1972 separately to study astrophysical problems, such as star and galaxy formations. Recently, there has been a strong interest in devoting considerable amount of research to implement SPH to engineering problems by solving energy, mass and momentum balance. Several examples where SPH has been studied includes flow in porous media (Tartakovsky et al. [149]), splash of water (Dalrymple and Rogers [28]), fluid-solid interactions (Antoci et al. [6]).

In SPH, the continuum is represented by an ensemble of particles. Strictly speaking, the term particle refers to a geometrical position in the continuum. Particles are bestowed with mass, momentum, temperature, concentration or other hydrodynamic properties. SPH approach assumes that the fields of the particle of interest are affected by that of all

other particles within the continuum under consideration. In order to narrow down the contributions coming from other particles in order for reducing the computation time, SPH only includes the effects of nearby particles, within a smoothing radius of  $\kappa h$ , also called support domain, where  $\kappa$  is a constant. The support domain is a localized domain over which the Kernel is nonzero. Therefore, the kernel  $W(|\vec{r}_i - \vec{r}_j|, h)$  is the function of distance between the particle of interest  $\vec{r}_i$  and neighboring particle  $\vec{r}_j$  as well as the smoothing length.

If the Dirac delta function in Eq. (2.11) is replaced by a smoothing kernel function, written as  $W(|\vec{r}_i - \vec{r}_j|, h)$ , the integral estimate or the kernel approximation to an arbitrary function  $f(\vec{r}_i)$  can be introduced as

$$f(\vec{r}_i) \approx \langle f(\vec{r}_i) \rangle \equiv \int_{\Omega} f(\vec{r}_j) W(|\vec{r}_i - \vec{r}_j|, h) d^3\vec{r}_j, \quad (3.1)$$

where the angle bracket " $\langle \rangle$ " denotes the kernel approximation,  $d^3\vec{r}_j$  is a differential volume element and  $\Omega$  represents the total bounded volume of the domain. Approximation to the Dirac-delta function  $\delta(|\vec{r}_i - \vec{r}_j|)$  by a smoothing kernel function is the origin of the SPH approach. It is important to note that Eq. (3.1) is no longer exact. For the Dirac-delta function to be approximated by a smoothing kernel function the smoothing kernel has to satisfy several conditions; the first one is the *normalization condition* that requires

$$\int_{\Omega} W(|\vec{r}_i - \vec{r}_j|, h) d^3\vec{r}_j = 1. \quad (3.2)$$

The second condition is the *Dirac-delta function* property. That is, as the smoothing length approaches to zero, the Dirac-delta function is recovered. Hence,

$$\lim_{h \rightarrow 0} W(|\vec{r}_i - \vec{r}_j|, h) = \delta^3(|\vec{r}_i - \vec{r}_j|). \quad (3.3)$$

The third condition is the compactness or *compact support*. This means that the kernel function has a compact support domain beyond which it becomes zero

$$W(|\vec{r}_i - \vec{r}_j|, h) = 0 \quad \text{when } |\vec{r}_i - \vec{r}_j| > \kappa h, \quad (3.4)$$

and be positive within the support domain.

Due to the compactness condition, the integration over entire problem is localized; therefore, from this point onward, the integration domain  $\Omega$  represents the support domain. The last condition is that the kernel function has to be spherically symmetric even function

$$W(|\vec{r}_i - \vec{r}_j|, h) = W(-|\vec{r}_i - \vec{r}_j|, h). \quad (3.5)$$

In literature, it is possible to find the variety of kernel function which satisfies above-listed conditions. Most famous ones are Gaussian and spline kernel distributions. The smoothing kernels can be considered as discretization schemes in mesh dependent techniques such as finite difference and volume. Stability, accuracy and the speed of SPH simulation heavily depend on the choice of the smoothing kernel distribution as well as the smoothing length. Eq. (3.6) gives the quintic spline kernel function representation (which widely used in this work)

$$W_{ij} = \frac{7}{478\pi h^2} \begin{cases} (3-q)^5 - 6(2-q)^5 + 15(1-q)^5, & 0 \leq q \leq 1 \\ (3-q)^5 - 6(2-q)^5, & 1 \leq q \leq 2 \\ (3-q)^5, & 2 \leq q \leq 3 \\ 0, & 3 \leq q \end{cases} \quad (3.6)$$

where we have used a concise notation, i.e.  $W_{ij} = W(|\vec{r}_i - \vec{r}_j|, h)$ . Here,  $q = r_{ij}/h$ .

It is also valuable to mention that the SPH approximation of a function is second order accurate as long as the function can be differentiated up to the second order. To show this, one can initiate with Taylor expansion of Eq. (3.1) as

$$\langle f(\vec{r}_i) \rangle = \int_{\Omega} \left( f(\vec{r}_i) + r_{ji}^k \frac{\partial f(\vec{r}_i)}{\partial x_i^k} + \frac{1}{2} r_{ji}^k r_{ji}^l \frac{\partial^2 f(\vec{r}_i)}{\partial x_i^k \partial x_i^l} \right) W_{ij} d^3 \vec{r}_j. \quad (3.7)$$

Using the sum rule in integration Eq. (3.7) is reduces to

$$\langle f(\vec{r}_i) \rangle = f(\vec{r}_i) \underbrace{\int_{\Omega} W_{ij} d^3 \vec{r}_j}_{=1} + \frac{\partial f(\vec{r}_i)}{\partial x_i^l} \underbrace{\int_{\Omega} r_{ji}^k W_{ij} d^3 \vec{r}_j}_{=0} + \frac{1}{2} \frac{\partial^2 f(\vec{r}_i)}{\partial x_i^k \partial x_i^l} \underbrace{\int_{\Omega} r_{ji}^k r_{ji}^l W_{ij} d^3 \vec{r}_j}_{=\delta^{kl}}. \quad (3.8)$$

The first integral term in Eq. (3.8) is equal to unity because Kernel used is properly normalized. The second integral on the right hand side of the same equation vanishes since integration of a symmetric odd function over whole space is zero. The kernel used is a symmetric even function. Position vector is an odd function. Multiplication of an even and odd function is an odd function. This is a very important point to remember since it forms the basis for the derivation of SPH equations. The remaining integral is equal to identity tensor or Kronecker delta due to the spherical symmetry and isotropy. The proof for the last integration will be introduced in section A when Laplace of a function is approximated by a first order derivative. Consequently Eq. (3.8) is further simplified to

$$\langle f(\vec{r}_i) \rangle = f(\vec{r}_i) + \frac{1}{2} \frac{\partial^2 f(\vec{r}_i)}{\partial x_i^k \partial x_i^k}, \quad (3.9)$$

which shows a second order accuracy for the SPH approximation of an arbitrary function.

### 3.2 The first and second derivative approximations

The integral estimate or the kernel approximation to an arbitrary function  $f(\vec{r}_i)$ , evaluated at particle  $\mathbf{i}$  can be introduced as (Eq. (3.1))

$$f(\vec{r}_i) \cong \langle f(\vec{r}_i) \rangle \equiv \int_{\Omega} f(\vec{r}_j) W_{ij} d^3 \vec{r}_j. \quad (3.10)$$

Approximating the integration in Eq. (3.10) by the summation over particle  $\mathbf{j}$  and setting  $d^3 \vec{r}_j = 1/\psi_j$ , one can write SPH interpolation for an arbitrary field  $f(\vec{r}_i)$  as

$$f(\vec{r}_i) = \sum_{\mathbf{j}} \frac{1}{\psi_j} f(\vec{r}_j) W_{ij}, \quad (3.11)$$

where the number density  $\psi_{\mathbf{i}}$  for the particle  $\mathbf{i}$  is defined as

$$\psi_{\mathbf{i}} = \sum_{\mathbf{j}} W_{\mathbf{ij}}, \quad (3.12)$$

which is approximately equal to reciprocal of the corresponding particle's volume  $\psi_{\mathbf{i}} = \rho_{\mathbf{i}}/m_{\mathbf{i}}$ .

The SPH approximation for the gradient of an arbitrary function  $f(\vec{\mathbf{r}}_{\mathbf{i}})$  can be introduced as

$$\frac{\partial f(\vec{\mathbf{r}}_{\mathbf{i}})}{\partial x_{\mathbf{i}}^k} = \sum_{\mathbf{j}} \frac{1}{\psi_{\mathbf{j}}} f(\vec{\mathbf{r}}_{\mathbf{j}}) \frac{\partial W_{\mathbf{ij}}}{\partial x_{\mathbf{i}}^k}, \quad (3.13)$$

For improving the accuracy and the stability of the SPH method, in the literature, several forms of corrective SPH gradient discretizations have been proposed and implemented with the aim of remedying particle inconsistency and kernel-boundary truncation related problems. Out of many excellent SPH studies that utilized the corrective SPH schemes, some deserves particular mention due to being the pioneering works in the field [123, 93, 19, 75, 91, 92, 18]. Randalls et al. [123] used the renormalization procedure which modifies the gradient of the kernel function through utilizing two by two corrective matrix. Liu, Belytschko, and their co-workers [93, 19, 75, 91, 92] in series of papers used a reproducing kernel approach, which consists of a correction function and the conventional SPH kernel function and showed that their correction formulations removes the tensile instability [91]. It should be mentioned that many other corrective formulations are also possible. For example, Chen and Beraun in [18] also presented corrective SPH formulations for the first and the second order derivatives. Their first-order derivative correction is quite similar to what has been utilized in this work. However, their second-order derivative correction requires the inversion of three by three matrix unlike the formulation presented in this work. In our earlier studies, we have attempted to use a corrective SPH formulation for the second-order derivative which also necessitate the inversion of three by three corrective matrix, and observed that three by three corrective matrix is rather sensitive to particle distribution, and becomes easily ill-conditioned, which is not the case for two by two corrective matrix [136].

Using a Taylor series expansion and the properties of a second-rank isotropic tensor, the corrective SPH approximation for the gradient of a vector-valued function can also be introduced as

$$\frac{\partial f^p(\vec{r}_i)}{\partial x_i^k} a_i^{ks} = \sum_j \frac{1}{\psi_j} (f^p(\vec{r}_j) - f^p(\vec{r}_i)) \frac{\partial W_{ij}}{\partial x_i^s}, \quad (3.14)$$

where  $a_i^{ks} = \sum_j \frac{1}{\psi_j} r_{ji}^k \frac{\partial W_{ij}}{\partial x_i^s}$  is the corrective second-rank tensor. The corrective term  $a_i^{ks}$  is ideally equal to Kronecker delta  $\delta^{ks}$  for a continuous function (see Appendix A for more details). The corrective SPH discretization scheme for the Laplacian of an arbitrary function can be written in two different ways [136, 138]

$$\frac{\partial}{\partial x_i^k} \left( \zeta_i \frac{\partial f^p(\vec{r}_i)}{\partial x_i^k} \right) = 8(a_i^{pm})^{-1} \sum_j \frac{2}{\psi_j} \frac{\zeta_i \zeta_j}{\zeta_i + \zeta_j} (f^p(\vec{r}_i) - f^p(\vec{r}_j)) \frac{r_{ij}^p}{r_{ij}^2} \frac{\partial W_{ij}}{\partial x_i^m}, \quad (3.15)$$

$$\frac{\partial}{\partial x_i^k} \left( \zeta_i \frac{\partial f^p(\vec{r}_i)}{\partial x_i^k} \right) = \frac{8}{(1 + a_i^{ll})} \sum_j \frac{2}{\psi_j} \frac{\zeta_i \zeta_j}{\zeta_i + \zeta_j} (f^p(\vec{r}_i) - f^p(\vec{r}_j)) \frac{r_{ij}^s}{r_{ij}^2} \frac{\partial W_{ij}}{\partial x_i^s}, \quad (3.16)$$

where  $\zeta$  might denote  $\mu$ , and  $\rho^{-1}$ . In a multiphase system with a large mismatch in transport parameters such as density and viscosity of phases, the attentive treatment of interface fluxes or gradients is of significant importance for the accuracy and the robustness of the computation. Therefore, it is a common practice in the SPH approach to smooth transport parameters through using a weighted harmonic mean interpolation, namely  $\zeta_i = 2\zeta_i \zeta_j / (\zeta_i + \zeta_j)$ , as has been done in above equations.

In this work, Eq. (3.15) is used for the discretization of the Laplacian of velocity field in the linear momentum equation while Eq. (3.16) is utilized for the Laplacian of pressure in the pressure Poissons equation.

### 3.3 Projective SPH

Let us have two vectors  $\vec{u}$  and  $\vec{w}$ . By using the vector dot product, we can extract parts of a vector in particular directions. The operation  $\vec{u} \cdot [\vec{w}]$  (where  $[\vec{w}] = \vec{w}/|\vec{w}|$ ) gives the rectangular component of  $\vec{u}$  in the direction of  $\vec{w}$ . If we were to multiply the  $\vec{u} \cdot [\vec{w}]$

by  $[\vec{w}]$ , then we would obtain a vector that is in the direction of  $\vec{w}$ . This operation, in which multiplying the component of  $\vec{u}$  in the direction of  $[\vec{w}]$  by  $[\vec{w}]$  itself is called the orthogonal vector projection of  $\vec{u}$  onto  $\vec{w}$ . This new vector will be denoted by

$$\vec{u}^{Dw} = (\vec{u} \cdot [\vec{w}])[\vec{w}] = \frac{\vec{u} \cdot [\vec{w}]}{[\vec{w}] \cdot [\vec{w}]} [\vec{w}]. \quad (3.17)$$

The remaining part of the vector  $\vec{u}$  that is perpendicular to  $\vec{w}$ , which will be denoted by  $\vec{u}^{Pw}$  is then calculated as

$$\vec{u}^{Pw} = \vec{u} - \vec{u}^{Dw} = \vec{u} - \vec{u} \cdot ([\vec{w}] \otimes [\vec{w}]), \quad (3.18)$$

or in index notation as

$$u_l^{Pw} = u_l - u_l^{Dw} = u_k \underbrace{(\delta_{lk} - [w]_k [w]_l)}_{P_{kl}}, \quad (3.19)$$

where  $P_{kl}$  is a second rank tensor, is referred to as orthogonal projector, and when it is operated on a vector field, it extracts its tangential component. Eq. (3.19) shows clearly that any vector can be decomposed into two parts; one is being parallel to  $\vec{w}$  and the remainder is perpendicular to  $\vec{w}$ . Depending on this idea, the Helmholtz-Hodge decomposition theorem states that an arbitrary vector field  $\vec{w}$  can be decomposed into the sum of other vector fields; a divergence-free vector field, and the gradient of a scalar field.

$$\vec{w} = \vec{u} + \nabla\Phi, \quad (3.20)$$

where  $\vec{u}$  is a divergence free vector field ( $\nabla \cdot \vec{u} = 0$ ) and  $\Phi$  is a scalar field (see Fig. 3.1).

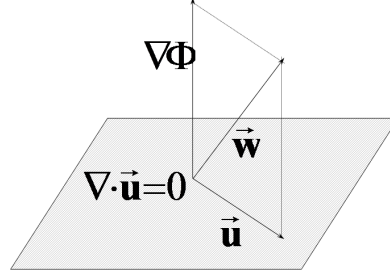


FIGURE 3.1: The schematic representation of Helmholtz-Hodge decomposition on a divergence free subspace.

Operating the projection operator  $\mathbf{P}$  on Eq. (3.20), we can have,

$$\mathbf{P} \cdot \vec{u} = \mathbf{P} \cdot \vec{w} - \underbrace{\mathbf{P} \cdot \nabla \Phi}_{=0} = \vec{u}, \quad (3.21)$$

where  $\mathbf{P} \cdot \nabla \Phi = 0$  are used. This results shows that the projector tensor projects any arbitrary vector  $\vec{w}$  field onto its divergence free part  $\vec{u} = \mathbf{P} \cdot \vec{w}$ . If we apply the divergence operator to both side of  $\vec{w} = \vec{u} + \nabla \Phi$ , we will obtain a Poisson equation for the scalar field with the divergence of  $\vec{w}$  being the source term which is subjected to the Neumann boundary condition  $\partial \Phi / \partial n = 0$  at the boundary

$$\nabla \cdot \vec{w} = \nabla^2 \Phi. \quad (3.22)$$

Solution of this equation is then used to compute the projection

$$\vec{u} = \mathbf{P} \cdot \vec{w} = \vec{w} - \nabla \Phi. \quad (3.23)$$

### 3.4 XSPH

In smoothed particle hydrodynamics particles are moved using the following relation,

$$\frac{dx_{\mathbf{i}}^k}{dt} = v_{\mathbf{i}}^k. \quad (3.24)$$

Here, the  $v_{\mathbf{i}}^k$  is the velocity components for particle  $\mathbf{i}$  that is computed through the solution of the balance of the linear momentum equation. It should be noted that in

the SPH method, the orderness of particles affects the accuracy of interpolations for the gradient and Laplacian computations. Therefore, for computational stability and accuracy, it is preferable to move the particles in a more orderly fashion, which can be achieved through using the XSPH technique suggested by Monaghan [102]. The XSPH method includes the contribution from neighboring particles, hence causing a fluid particle to move with an average velocity

$$\frac{dx_{\mathbf{i}}^k}{dt} = v_{\mathbf{i}}^k - \varepsilon \sum_{\mathbf{j}} \frac{2m_{\mathbf{j}}}{\rho_{\mathbf{i}} + \rho_{\mathbf{j}}} (v_{\mathbf{i}}^k - v_{\mathbf{j}}^k) \hat{W}_{\mathbf{ij}}, \quad (3.25)$$

where the second term on the right hand side is the XSPH-averaged new velocity by the correction factor of  $\varepsilon$  ( $0 < \varepsilon < 1$ ).

### 3.5 Artificial viscosity

The artificial viscosity term is included in the current model in order to circumvent numerical instabilities due to the meshless nature of the SPH method. This term introduces some numerical diffusion into the model, thus preventing non-physical oscillations. There are various forms of the artificial viscosity term in SPH literature. In this work, the one suggested by Monaghan [102] is implemented in the form of

$$\Pi_{\mathbf{ij}} = \frac{8\mu_m(\vec{v}_{\mathbf{ij}} \cdot \vec{r}_{\mathbf{ij}})}{\psi_{\mathbf{i}}\psi_{\mathbf{j}}(r_{\mathbf{ij}}^2 + \epsilon h_m^2)}. \quad (3.26)$$

Here,  $h_m = \frac{h_{\mathbf{i}} + h_{\mathbf{j}}}{2}$ ,  $\epsilon \approx 0.0001$  is a small number that is introduced to prevent singularity when  $r_{\mathbf{ij}} = 0$ , and  $\mu_m$  is the harmonic average of  $\mu_{\mathbf{i}}$  and  $\mu_{\mathbf{j}}$ , which is defined as

$$\mu_m = \frac{2}{\frac{1}{\mu_{\mathbf{i}}} + \frac{1}{\mu_{\mathbf{j}}}}, \quad (3.27)$$

where  $\mu_{\mathbf{i}} = \frac{1}{8}\alpha h_{\mathbf{i}} c_{\mathbf{i}} \rho_{\mathbf{i}}$  in which  $c$  is the speed of sound and  $\alpha$  is the artificial viscosity constant.

### 3.6 Multiple Boundary Tangent (MBT) method

In most engineering problems, the domain of interest has, in general, solid boundaries. The SPH formulations being valid for all interior particles are not necessarily accurate for particles close to the domain boundary since the kernel function is truncated by the boundary. Therefore, the application of boundary conditions is problematic in the SPH technique. Consequently, the proper and correct boundary treatments have been an ongoing concern for an accurate and successful implementation of the SPH approach (Kulasegaram et al. [80], Feldman and Bonet [80, 40]) as well as other meshless methods (Krongauz and Belytschko [79], Alfaro et al. [3]) in the solution of engineering problems with solid walls. Improper boundary treatment has two important consequences. The first originates from the penetration of fluid particles into boundary walls, which then leave the computational domain. The second is that kernel truncation at the boundary produces errors in the solution. Hence, over the years, several different approaches have been used for the boundary treatment such as specular reflections, or bounce-back of fluid particles with the boundary walls (Simpson and Wood [142]), Lennard-Jones Potential (LJP) type force as a repulsive force (Monaghan and Kos [103], Monaghan [102]), ghost particles (Morris et al. [105], Colagrossi and Landrini [23], and Takeda et al. [147]), and Multiple Boundary Tangent (MBT) method (Yildiz et al. [168], Shadloo et al. [136]) which is initially proposed to treat complex boundaries and is mainly used in this work.

The various steps of implementing MBT boundary treatment technique to the airfoil geometry (as an example of a complex geometry with highly curved part at the tip and thin region at the tail), as depicted in Figs. 3.2 and 3.3, are as follows:

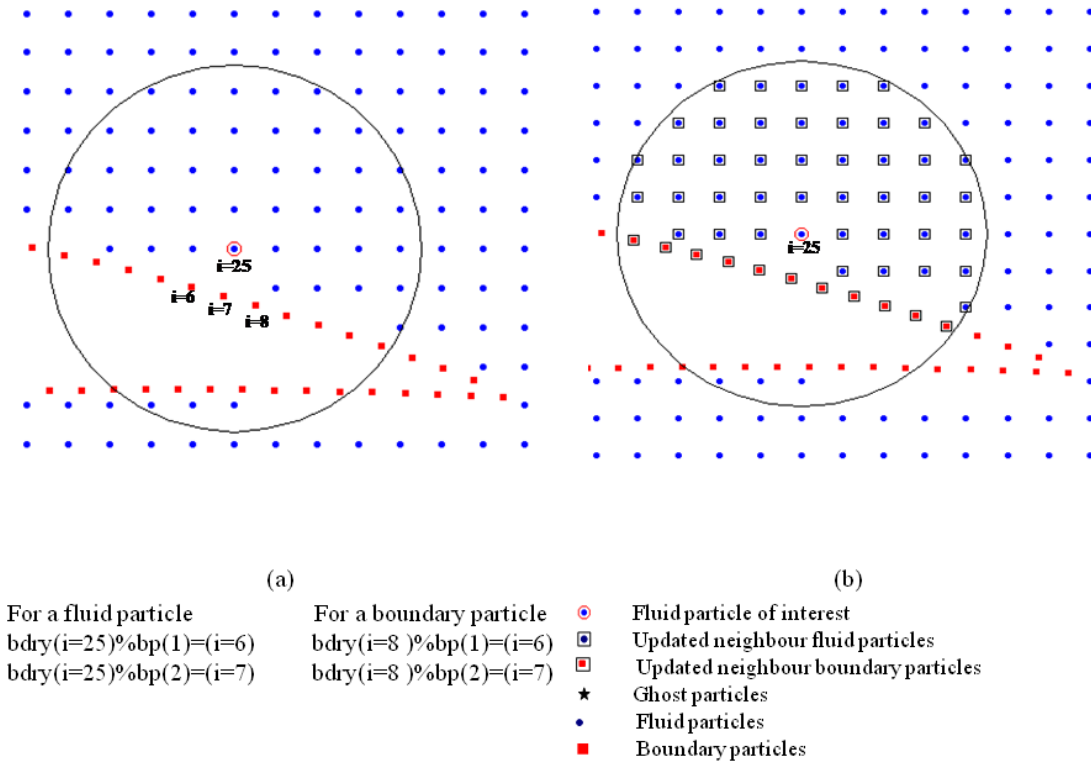


FIGURE 3.2: Boundary treatment for a submerged thin object: (a) step-1, and (b) step-2.

1. At each or prescribed time steps, all near boundary fluid particles (particles with boundary truncations) as well as boundary particles are associated with their neighbour boundary particles using the cell array data structure (the Fortran 90 derived data type) as also described in [168], see Fig. 3.2a. When dealing with a thin solid object enclosed by flow such as the trailing edge of the airfoil, for instance, near boundary fluid particles or boundary particles positioned above/on the upper camber take contribution from fluid and boundary particles located below the upper camber since the weighting function  $W_{ij}$  has an influence domain that spans over the smoothing radius. Physically, particles flanking a solid wall should not affect each other. Consequently, the neighbour list computed through the standard box-sorting algorithm has to be modified, and then updated at each time step. The neighbour boundary particles of a given near boundary fluid particle are sorted in accordance with the distance between boundary particles and the fluid particle in ascending order. Then, the fluid particle in question is given the unit normal vector of its nearest boundary neighbour particle. For instance, fluid particle  $i = 25$  in Fig. 3.2 is given the unit normal of the boundary particle

$\mathbf{i} = 7$ . The neighbour lists of all particles are updated by computing the angles ( $\vec{\mathbf{n}}_{\mathbf{i}} \cdot \vec{\mathbf{n}}_{\mathbf{j}}$ ) among unit normal vectors of particles and their neighbours. Here,  $\vec{\mathbf{n}}_{\mathbf{i}}$  and  $\vec{\mathbf{n}}_{\mathbf{j}}$  are the unit normal of a given particle and its neighbours. Only the particles with angles smaller than the preset value ( $130^\circ$  used in this study) are regarded as neighbours to each other, whereby forming the updated neighbour list. To be more specific, as can be seen from Fig. 3.2b, the updated neighbour list of the particle  $\mathbf{i} = 25$  include only those particles enclosed by a square frame since other neighbour particles do not satisfy the preset angle condition even though they are in the influence domain of the particle  $\mathbf{i}=25$ .

2. As in the case of previous step, all near boundary fluid and boundary particles are associated with their updated neighbour boundary particles. Associating near boundary fluid particles and boundary particles with their neighbour boundary particles and sorting and then storing these neighbour boundary particles in accordance with the shortest distance among them allows for (i) the computation of the overlapping contributions of mirrored particles from each boundary particle, (ii) the confinement of the mirrored particles into the solid domain, (iii) defining solid boundaries by the envelope of boundary tangent lines, as well as (iv) associating mirrored particles with near boundary fluid particles.
3. Given that each boundary particle has fluid particles in its influence domain as neighbours, these fluid particles are mirrored with respect to the tangent line of the corresponding boundary particle as indicated in Fig. 3.3. The fluid particles should satisfy the condition  $\vec{\mathbf{r}}_{bf} \cdot \vec{\mathbf{n}}_b \geq 0$ , where  $\vec{\mathbf{r}}_{bf}$  is a position vector between the boundary particle and its neighbour fluid particles directing towards the fluid particles and  $\vec{\mathbf{n}}_b$  is the unit normal of the boundary particle. This condition ensures that only fluid particles above the associated boundary particle tangent line are mirrored. The second condition  $\vec{\mathbf{r}}_{nbg} \cdot \vec{\mathbf{n}}_{nb} \leq 0$  to be fulfilled is that mirrored particles should be confined into the solid region, meaning that mirrored particles associated with a boundary particle have to be inside of the all tangent lines of the neighbour boundary particles of the boundary particle in question, where  $\vec{\mathbf{r}}_{nbg}$  is the position vector between the ghost particles and the neighbour boundary particles of the given boundary particle and,  $\vec{\mathbf{n}}_{nb}$  is the unit normal vector of the neighbour boundary particles for the boundary particle in question. Using the cell array structure, every boundary particle is associated with its corresponding

mirrored particles. Spatial coordinates and particle identification numbers of mirrored particles are stored in a cell array. To be more precise, mirrored particles are associated with the particle identification number of the fluid particle from which they are originated (referred to as the 'mother' fluid particle). For example, for a fluid particle indexed with  $i = 25$ , the ghost particle mirrored about a boundary particle tangent line (for example, boundary particle 7) will also be associated with  $i = 25$  as shown in Fig. 3.3a. Note that fluid and boundary particles have numerical identifications that are permanent, whereas mirrored particles have varying (dummy) indices, throughout the simulation. A ghost particle is given the same mass, density and transport parameters, such as viscosity, as the corresponding fluid particle. As for the field values (i.e. velocities) of a ghost particle, they are obtained depending on the type of boundary condition implemented.

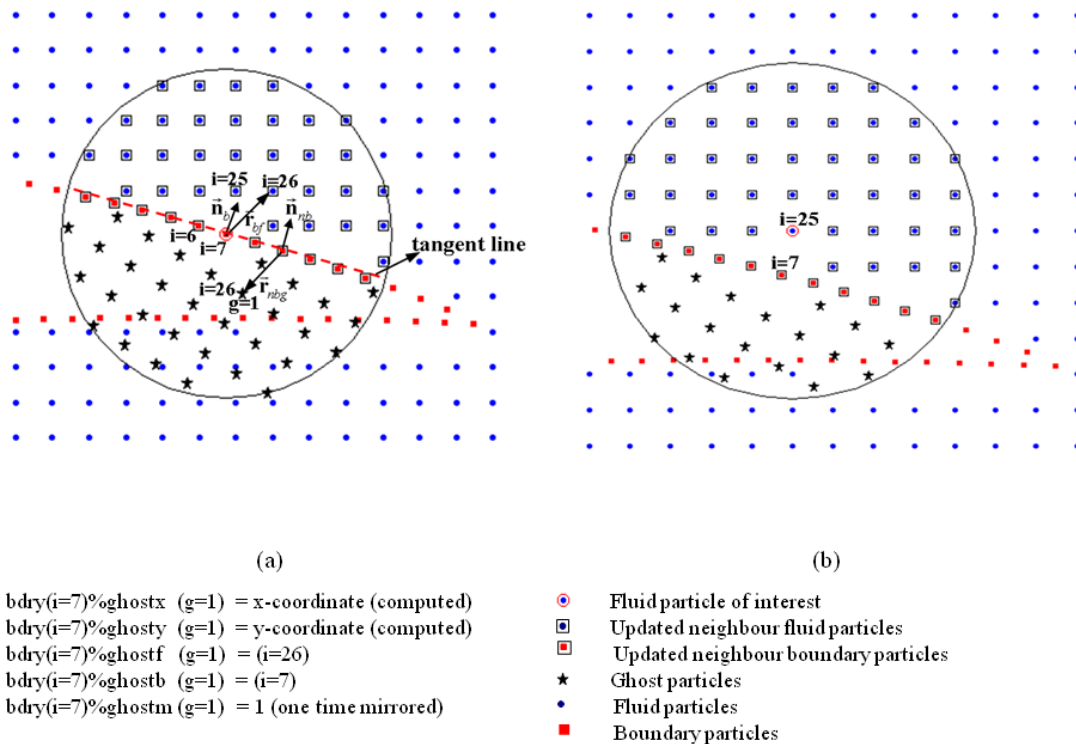


FIGURE 3.3: Boundary treatment for a submerged thin object; (a): step-3 and (b): step-4.

- In a loop over all particles, if a fluid particle has a boundary particle or multiple boundary particles as neighbour(s), then the fluid particle will become a neighbour of all mirrored particles associated with the corresponding boundary particles on the condition that (i) the mirrored particles are in the influence domain of the fluid

particle in question, and (ii) for a mirrored particle, its mother particle has to be within the influence domain of the fluid particle in question. During the creation of ghost particles, there is an over-creation of ghost particles due to the fact that the influence domain of neighbouring boundary particles overlaps. The overlapping contributions of mirrored particles can be eliminated by determining the number of times a given fluid particle is mirrored into the influence domain of the associated fluid particle with respect to a boundary particle's tangent line. For computational efficiency, the fluid particle can only be associated with the mirror particles of its several nearest boundary particle rather than all neighbour boundary particles as explained in Fig. 3.3b. Boundary particle  $\mathbf{i} = 7$  has the shortest distance to  $\mathbf{i} = 25$  compared to other boundary particles neighbor to the fluid particle  $\mathbf{i} = 25$ . Hence, mirror particles of  $\mathbf{i} = 7$  also become the neighbor of  $\mathbf{i} = 25$  provided that above two conditions (*i* and *ii*) are satisfied. Near boundary fluid particles hold the information of spatial coordinates and fluid particle identity numbers, boundary particle identity numbers (i.e. the particle number for a boundary particle to which mirrored particles are associated initially), and over-creation number for mirrored particles in the cell array format. During the SPH summation over ghost particles for a fluid particle with a boundary truncation, the mass of the ghost particles are divided by the number of corresponding over-creations.

### 3.7 Instabilities and their possible remedies in SPH method

The homogeneity of the particle distribution is quite important for the accuracy and the robustness of the SPH method. The formation of ill particle distributions during the simulation may result in the numerical solution to fail. For instance, if the pressure field is solved correctly thereby imposing the incompressibility condition as accurately as possible, the particle motion closely follows the trajectory of streamline, hence resulting in a linear clustering and in turn fracture in particle distribution. In these regions due to the lack of sufficient number of particles, or inhomogeneous particle distribution, the gradients of field variables can not be computed reliably. Such a situation leads to spurious fields, especially erroneous pressure values in the ISPH approach. As the computation progresses, errors in computed field variables accumulate whereby blowing-up the simulation.

To prevent the particle clustering, the trajectory of particles can be disturbed by adding relatively small artificial displacement,  $\delta r_{\mathbf{i}}^k$ , to the advection of particles computed by the solution of the equation of motion. Recall the form of a Lennard-Jones potential (LJP)-type force used in the SPH literature as a repulsive force for the solid boundary treatment,

$$F_{\mathbf{i},LJP}^k = \sum_{\mathbf{j}}^N \left[ \left( \frac{r_o}{r_{\mathbf{ij}}} \right)^{n_1} - \left( \frac{r_o}{r_{\mathbf{ij}}} \right)^{n_2} \right] \frac{\beta r_{\mathbf{ij}}^k v_{max}^2}{r_{\mathbf{ij}}^2}, \quad (3.28)$$

where  $F_{\mathbf{i},LPG}^k$  is the force per unit mass on fluid particle  $\mathbf{i}$  due to the neighbor particles  $\mathbf{j}$ ,  $n_1$  and  $n_2$  are constants,  $\beta$  is a problem-dependent parameter,  $r_o$  is the cutoff distance and  $v_{max}$  is the largest particle velocity in the system. If the second term (attractive interaction) on the right-hand side of LJP force is neglected, and  $n_1 = 2$ , and the force  $F_{\mathbf{i},LPG}^k$ , and  $v_{max}$  are replaced by  $\delta r_{\mathbf{i}}^k / (\Delta t)^2$  and  $r_{\mathbf{ij}}^k / \Delta t$ , one can write the relationship

$$\delta r_{\mathbf{i}}^k = \beta \sum_{\mathbf{j}}^N \frac{r_{\mathbf{ij}}^k}{r_{\mathbf{ij}}^3} r_o^2 v_{max} \Delta t, \quad (3.29)$$

where  $\delta r_{\mathbf{i}}^k$  is the artificial particle displacement (APD) vector. Here, the cut-off distance can be approximated as  $r_o = \sum_{\mathbf{j}}^N r_{\mathbf{ij}} / N$ . Given that  $r_{\mathbf{ij}}^k / r_{\mathbf{ij}}^3$  is an odd function with vanishing integral, one can write  $\sum_{\mathbf{j}}^N r_{\mathbf{ij}}^k / r_{\mathbf{ij}}^3 = 0$  for a spherically symmetric particle distribution. However, if the particle distribution is asymmetric, and clustered, the term  $\sum_{\mathbf{j}}^N r_{\mathbf{ij}}^k / r_{\mathbf{ij}}^3 \neq 0$  is no longer equal to zero, whereby implying the region with clustered particle distribution. The APD is only influential in the clustered region and negligibly small in the rest of the computational domain due to  $\sum_{\mathbf{j}}^N r_{\mathbf{ij}}^k / r_{\mathbf{ij}}^3 \cong 0$  provided that the particle distribution is closely uniform. The offset vector between the particle  $\mathbf{i}$  and the center of mass of its influence domain,  $\delta \tilde{r}_{\mathbf{ii}}^k$ , can be presented as

$$\delta \tilde{r}_{\mathbf{ii}}^k = x_{\mathbf{i}}^k - \tilde{x}_{\mathbf{i}}^k = \sum_{\mathbf{j}=1}^N \frac{r_{\mathbf{ij}}^k}{N}, \quad (3.30)$$

where  $x_{\mathbf{i}}^k$  and  $\tilde{x}_{\mathbf{i}}^k$  are the coordinates of the particle  $\mathbf{i}$  and the center of mass for the influence domain of the particle  $\mathbf{i}$ .

The comparison of the APD and offset vector implies that upon using the particle displacement vector in the advection equation, the particle  $\mathbf{i}$  moves towards the diluted particle region (the region which is away from the center of mass). Hence, the fractures in the simulation domain are repaired. Since the near boundary fluid particles have influence domains truncated by boundaries, with the usage of the artificial particle displacement vector in the computation, these fluid particles will tend to move towards the boundary and stick to it. Even though this situation may appear as a problem and the deficiency of the approach, it might be used in advantageous way such that fluid particles close to boundaries are then artificially forced to move in conformation with boundaries. Hence pressure forces on the boundaries can be computed much more accurately in that particle deficiency is no longer problem therein. In our simulations, since the ghost particles are used for near boundary fluid particles, the influence domain of the kernel function is fully populated, and therefore such a problem is not an issue. The artificial particle displacement vector is added to the particle advection equation in both prediction and correction steps. This approach repairs all the clustering and fracture in the domain gradually without inducing significant errors in the computation, and enabling a quite robust SPH approach. It is due to this approach that it becomes possible to run simulations with higher Reynolds numbers, which are otherwise impossible to achieve.

### 3.8 Initial and boundary conditions

The modeling process starts with generating particles for the flow domain and its boundaries. Initially, particles are created in the form of a rectangular grid with equidistant particle spacing. All physical boundaries are represented by a row of fixed particles (hereafter referred to as boundary particles) whose pertinent fields are evolved in accordance with the numerical solution. To distinguish among fluid and boundary particles, boundary and fluids particles are assigned to different integer labels. Additionally, boundary particles of dissimilar boundaries are also differently tagged, thereby enabling the implementation of various boundary conditions when necessary. Fluid and boundary particles are given their physical parameters and initial conditions. The particle spacing between each boundary particle is the same as the initial particle spacing between fluid particles. All particles are given the same smoothing lengths as  $h = \kappa r_{\mathbf{ij},o}$  where  $r_{\mathbf{ij},o}$  is the initial

particle spacing, and  $\kappa$  is a problem-dependent input parameter. It should note that in this work, a constant smoothing length is used.

Through using a standard box-search algorithm (see section 3.9), the neighbor list is formed for each particle. Subsequently, ghost particles are created for the incorporation of the MBT boundary treatment into the numerical procedure (see section 3.6). It should be mentioned that ghost particles are given the same mass, density, number density, and transport parameters (i.e., viscosity) as their corresponding fluid particles.

Either, no-slip, ( $\vec{v}|_{\Gamma} = 0$ ), or free-slip, ( $\vec{v} \cdot \vec{n} = 0$ ,  $\vec{t} \cdot (\nabla \vec{v} + \nabla \vec{v}^T) \cdot \vec{n} = 0$ , where for 2D vertical boundary it will reduce to:  $u = 0$ ,  $\frac{\partial v}{\partial x} = 0$ ), boundary conditions for the velocity field are applied depending on the considered case study. Pressure field is subjected to homogeneous Neumann boundary condition,  $\rho/\Delta t (\vec{v}^* - \vec{v}^{(n+1)}) \cdot \vec{n} = \nabla p \cdot \vec{n}$ , where  $\vec{n}$  is the unit normal vector. Upon replacing  $\vec{v}^*$  by  $\vec{v}^{(n+1)}$  [25], the pressure boundary condition reduces to  $\nabla p \cdot \vec{n} = 0$ .



FIGURE 3.4: The sketch of the channel for which fully periodic condition is imposed in the horizontal direction. Particles denoted by  $\triangleright$  are the imaginary copies of those designated by  $\blacktriangleright$  while particles represented by  $\triangleleft$  are the imaginary copies of those shown by  $\blacktriangleleft$ .

Field values  $\Lambda$  (i.e. velocities, pressure and elastic stress tensor) of a ghost particle, are obtained depending on the type of boundary condition implemented. For the Dirichlet boundary condition which specifies values for the field variables on the boundary of the domain, the following linear interpolation is utilized; namely,  $\Lambda_g = 2\Lambda_b - \Lambda_f$  where  $\Lambda_g$ ,  $\Lambda_b$  and  $\Lambda_f$  are the fields variables of the ghost, boundary, and fluid particles, respectively. As for the zero gradient boundary condition (Neumann boundary condition) which specifies values for the field variables as a derivative on the boundary, a ghost particle is assigned to the same field values as the corresponding fluid particle possesses  $\Lambda_g = \Lambda_f$ .

The fully periodic boundary condition is imposed in a following manner. In order to conserve the mass of the system, particles leaving the channel off the right boundary are reinserted into the flow domain from the left boundary at the same  $y$ -position. In addition, the fluid particles around the left boundary are defined as neighbors to those at the proximity of the right boundary and vice versa as shown in Fig. 3.4.

### 3.9 Neighbor search algorithm

There are several known searching algorithms that will find and store neighboring particles. Recall that neighbor particles are those particles  $\mathbf{j}$  that satisfy the condition  $r_{\mathbf{i}\mathbf{j}} \leq \kappa h$  for a given particle  $\mathbf{i}$ . The most direct approach for finding particle neighbors is to cycle through all particles, and check whether the above given condition is satisfied or not, storing the results. However, this algorithm searches all  $N$  particles for each of the  $N$  particles  $\mathbf{i}$ . Therefore, this type of search procedure is of the order  $N \times N$  in terms of computation searching effort required. A more efficient approach is the "box-sorting" algorithm, which is known to be of order  $N \log N$ . This algorithm divides the domain into an ordered number of boxes, with side dimensions equal to the maximum smoothing length in the domain ( $\kappa h_{max}$ ) in length. Each of the  $N$  particles,  $\mathbf{i}$ , is then catalogued by which box it is located in. Since the box side dimensions are chosen to be  $\kappa h_{max}$ , a neighbor  $\mathbf{j}$  of particle  $\mathbf{i}$  must be located in one of the adjacent boxes to the box containing particle  $\mathbf{i}$ . Therefore, instead of searching all  $N$  particles, one must search a much smaller group of particles. Due to the much smaller computational expense, all simulations in this work used the box-sorting procedure (see Fig. 3.5).

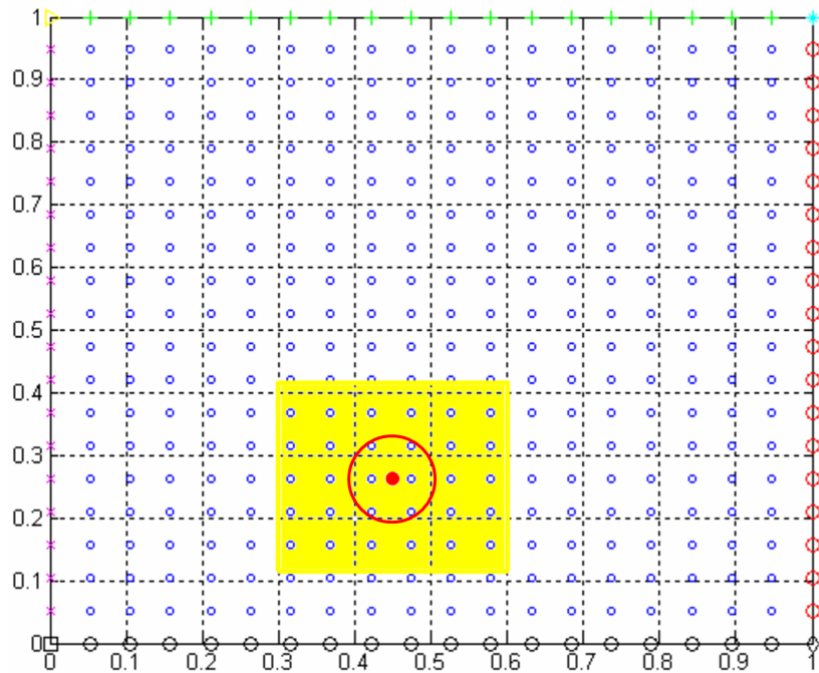


FIGURE 3.5: Schematic illustration of neighbor searching algorithm.

### 3.10 Numerical scheme

Here, we briefly introduce the numerical algorithm implemented in this work. There are two common approaches utilized in the SPH literature for solving the balance of the linear momentum equation. The first one is widely referred to as the weakly compressible SPH (WCSPH) where the pressure term in the momentum equation is determined through an artificial equation of state. In the second approach known as incompressible SPH (ISPH), the pressure is computed by means of solving a pressure Poisson equation. Within the frame work of this research program, we have implemented both WCSPH and ISPH approaches. It is noted that in this section we only present the numerical scheme for the ISPH treatment of the most complicated problem (i.e. two phase Electrohydrodynamics' problem), where all electric field, surface tension and viscous forces exist. The algorithm for WCSPH and for each individual problem are eliminated for the sake of redundancy. The interested readers are referred to our papers [135, 136, 137, 138, 170].

The procedure starts with the initial mass calculation for each particle using the relation  $m_i = \rho_i/\psi_o$  where  $\psi_o = \max(\psi_i)$  is the initial or reference particle number density which is retained constant during the computation. For the time marching, we have used a

first-order Euler time step scheme along with a projection method based ISPH approach [139]. Thus, we first move particles from their current positions  $\vec{r}_i^{(n)}$  with their current divergence free velocities  $\vec{v}_i^{(n)}$  at time  $t$  to the temporary or intermediate positions  $\vec{r}_i^*$  using

$$\vec{r}_i^* = \vec{r}_i^{(n)} + \vec{v}_i^{(n)} \Delta t + \delta \vec{r}_i. \quad (3.31)$$

Here, to enhance the robustness of the model, and circumvent the particle disorderness and fracture induced numerical problems, the APD term is added to the advection equation [136]. The APD vector  $\delta \vec{r}_i$  is calculated from the Eq. (3.29) for all fluid particles where the  $\beta$  is a problem-dependent parameter which is set to be equal to 0.03 for all test cases in this work. As it noted before the APD vector is an odd function and therefore has a non zero value only for asymmetric particle distribution.

Having advected particle positions to their intermediate positions, their neighbors (both real and ghost particles) are recalculated. Assuming relatively small changes in particle positions at each time step, one may presume that the neighbor of a given particle will not change significantly. Thus, the neighbor lists and ghost particles are updated every tenth time step to reduce the computational cost due to neighbor finder algorithm.

Afterward, in the interface subroutine, the surface tension force is computed using Eq. (5.13) (see section 5.3). Furthermore, since each fluid particle has constant density, viscosity, and electrical permittivity and conductivity ( $\rho$ ,  $\mu$ ,  $\varepsilon^E$  and  $\sigma^E$  respectively) which are discontinuous across the interface, the numerical scheme might have instabilities especially in the case of a large mismatch in the transport parameters of constituents. Thus, these transport parameters are smoothed in the same subroutine using the weighted arithmetic mean interpolation (see section 5.3)

$$\rho_i = (1 - C_i)\rho_1 + C_i\rho_2, \quad (3.32)$$

$$\mu_i = (1 - C_i)\mu_1 + C_i\mu_2, \quad (3.33)$$

$$\varepsilon_{\mathbf{i}}^E = (1 - C_{\mathbf{i}})\varepsilon_1^E + C_{\mathbf{i}}\varepsilon_2^E, \quad (3.34)$$

and

$$\sigma_{\mathbf{i}}^E = (1 - C_{\mathbf{i}})\sigma_1^E + C_{\mathbf{i}}\sigma_2^E. \quad (3.35)$$

Then, the intermediate velocity  $\vec{v}_{\mathbf{i}}^*$  is computed on the temporary particle locations through the solution of the momentum balance equations with the forward time integration as

$$\vec{v}_{\mathbf{i}}^* = \vec{v}_{\mathbf{i}}^{(n)} + \vec{f}_{\mathbf{i}}^{(n)} \Delta t. \quad (3.36)$$

Here,  $\vec{f}_{\mathbf{i}}^{(n)}$  represents the right hand side of the momentum balance equation given in Eq. (6.22), which embodies viscous, volumetric surface tension and electric forces excluding the pressure gradient term, calculated using old velocities, updated transport properties and intermediate positions. Given the intermediate particle positions and velocities, the intermediate number densities

$$\psi_{\mathbf{i}}^* = \psi_{\mathbf{i}}^{(n)} - \Delta t \psi_{\mathbf{i}}^{(n)} (\nabla \cdot \vec{v}_{\mathbf{i}}^*), \quad (3.37)$$

and mixture densities

$$\rho_{\mathbf{i}}^* = \psi_{\mathbf{i}}^* \sum_{\alpha} m_{\mathbf{i}}^{\alpha} C_{\mathbf{i}}^{\alpha}, \quad (3.38)$$

as well as divergences of intermediate velocities are calculated, which will be used at the correction step in the pressure Poisson equation. Then, at the correction step, we add the effect of pressure gradient term into intermediate velocity  $\vec{v}_{\mathbf{i}}^*$  to obtain the divergence free velocity vector  $\vec{v}_{\mathbf{i}}^{(n+1)}$  at the new time

$$\vec{v}_{\mathbf{i}}^{(n+1)} = \vec{v}_{\mathbf{i}}^* - \frac{\Delta t}{\rho_{\mathbf{i}}^*} \nabla p_{\mathbf{i}}^{(n+1)}. \quad (3.39)$$

where the pressure  $p^{(n+1)}$  has been obtained through the solution of the pressure-Poisson equation, which can be formulated in general form as

$$\frac{\nabla \cdot \vec{v}^*}{\Delta t} = \nabla \cdot \left( \frac{\nabla p^{(n+1)}}{\rho^*} \right). \quad (3.40)$$

To be able to treat large variation in the density across the interfaces in a robust manner without facing pressure related convergence issues, the discretization of the pressure gradient term (the second term on the right hand side) in Eq. (3.39) requires a special treatment. Upon using the product rule of differentiation, one can write that

$$\frac{1}{\rho} \nabla p = \nabla \left( \frac{p}{\rho} \right) - p \nabla \left( \frac{1}{\rho} \right), \quad (3.41)$$

whose right hand side can be discretized by using Eq. (3.14) as

$$\begin{aligned} \frac{1}{\rho} \nabla p &= (a_i^{ks})^{-1} \left( \sum_j \frac{1}{\psi_j} \left[ \left( \frac{p_j}{\rho_j} - \frac{p_i}{\rho_i} \right) - \left( \frac{p_i}{\rho_j} - \frac{p_i}{\rho_i} \right) \right] \frac{\partial W_{ij}}{\partial x_i^s} \right) \\ &= (a_i^{ks})^{-1} \left( \sum_j \frac{1}{\rho_j \psi_j} (p_j - p_i) \frac{\partial W_{ij}}{\partial x_i^s} \right). \end{aligned} \quad (3.42)$$

It is noted that in the calculation of the pressure gradient in Eq. (3.42), the intermediate number density and mixture densities are used.

Upon taking the divergence of Eq. (3.39) and noting that the incompressibility condition requires that  $\nabla \cdot \vec{v}_i^{(n+1)} = 0$ . Eq. (3.40) is solved using a direct solver based on the Gauss elimination.

Finally, with the correct velocity field for  $t^{(n+1)}$ , all fluid particles are advected to their new positions  $\vec{r}_i^{(n+1)}$  using an average of the previous and current particle velocities as

$$\vec{r}_i^{(n+1)} = \vec{r}_i^{(n)} + 0.5(\vec{v}_i^{(n)} + \vec{v}_i^{(n+1)})\Delta t + \delta \vec{r}_i. \quad (3.43)$$

Neighbor and ghost particle lists are updated, and then the initial (reference) number density of the fluid is restored. Finally, For a stable solution, the time step is selected in accordance with  $\Delta t \leq \frac{C_{CFL}h}{v_{max}}$  where  $C_{CFL} = 0.125$  in this work.

# Chapter 4

## Single Phase Flows

### 4.1 Introduction

Due to being a relatively new computational method for engineering applications, there are still a few significant issues with SPH that need to be scrutinized. It is still a challenge to model physical boundaries correctly and effectively. In addition, there are various ways to construct SPH equations (discretization), and a consistent approach has not gained consensus. Highly irregular particle distributions which occur as the solution progresses may cause numerical algorithms to break down, thereby making robustness another significant issue to be addressed. Namely, it is well-known by SPH developers that when passing from one test case to another, new problems are faced. For example, instabilities due to clamping of SPH particles which is not in general present in modeling a dam-breaking problem show themselves in the simulation of flow over bluff bodies, especially at the leading and trailing edges. These shortcomings are not insurmountable. The underlying factors causing these shortcomings can be understood through extensive research on the verification of SPH against a wide variety of possible applications as being done in the SPH literature.

As it mentioned before, in the SPH literature, there are two commonly utilized approaches for solving the balance of the linear momentum equations. The ISPH technique is based on the projection method originally proposed in [20, 21] and first implemented to the SPH method in the work of Cummins and Rudman [25], which is referred to as the standard projection method in this work. In this method, the pressure term

in the momentum balance equation is computed by solving a pressure Poisson's equation. The standard projection method has been reported to suffer from the density error accumulation during the computation of the intermediate density field [139, 114]. To circumvent this and the associated problems, and consequently enhance the accuracy and the performance of the standard ISPH scheme, several modifications have been proposed for it in literature. For example, Shao and Lo [139] enforced the incompressibility in a somewhat similar manner to the one proposed in [25] with two main differences: first, they computed the intermediate velocity and then advected SPH particles; and second, they utilized the density variation as a source term rather than the divergence of the intermediate velocity. Their projection scheme has been referred to as the density invariance algorithm in the SPH literature.

Hu and Adams [68] have pointed out the density invariant ISPH algorithm leads to large density variations, thereby producing less accurate pressure field. In what follows, they have proposed the concurrent usage of the standard and the density invariant ISPH algorithms. However, such an approach requires that the pressure Poisson's equation be solved two times in each time step of a simulation, hence bringing about additional computational load to the simulation.

As for the WCSPH method, the pressure is computed explicitly from a simple thermodynamic equation of state [25, 105, 99]. The above introduced state equations enforce the incompressibility condition on the flow such that a small variation in density produces a relatively large change in pressure thereby limiting the dilatation of the fluid to 1%. To keep the relative incompressibility or the density variation factor, defined as ( $\delta = \rho/\rho_o - 1$ ), under 1%, the sound speed is as a rule of thumb chosen to be at least one order of magnitude larger than the maximum bulk fluid velocity  $v_{max}$  thus resulting in a very small Mach number  $M = v_{max}/c = \delta^{0.5} = 0.1$ .

The major advantages of WCSPH over ISPH are the ease of programming and better ordered particle distributions. Mainly for these reasons, the WCSPH method has become the most widely used approach to solve the linear momentum balance equation in SPH literature. However, unlike the ISPH method, when dealing with fluid flow problems characterized by higher Reynolds number values (i.e. greater than 100), the standard WCSPH method has been reported to suffer from large density variations, and therefore it requires the usage of a much smaller Mach number than 0.1 to avoid the formation

of unphysical void regions in the computational domain [74, 84]. From the numerical stability point of view, the speed of sound has a direct effect on the permissible time-step in a given simulation, and hence directly affects the total computational cost.

There are several recent works that have aimed to compare ISPH against WCSPH for free surface and bluff body problems [84, 71, 85]. Hughes and Graham [71] have recently compared the ISPH and WCSPH approaches for free-surface water flows. They have concluded in their work that if the standard WCSPH method is used along with some special treatments such as density smoothing, the WCSPH technique can be as correct as the ISPH approach. On the other hand, Lee et al. [85] illustrated that the ISPH method produces more accurate pressure fields with respect to the WCSPH through simulating three-dimensional (3D) water collapse in waterworks, and consequently concluded that the ISPH method is much more reliable in modelling free surface flow problems.

Referring back to the reported SPH simulation results in literature, one may argue that there is still no consensus in the SPH community on WCSPH being as accurate as the ISPH method. Therefore, the necessity of further comparisons of both methodologies to enforce the incompressibility condition is obvious, which is also acknowledged in [51]. To shed further light on the current understanding of the performance of both methodologies, an improved SPH algorithm for both WCSPH and ISPH approaches is proposed and implemented. The improved algorithm comprises the following: (i) the MBT method to treat solid boundaries with complex geometries [136]; (ii) the APD procedure to repair the nonuniformity and local fractures in particle distributions; and (iii) a corrective SPH discretization scheme to circumvent the particle inconsistency problem and in turn enhance the accuracy of the overall computation. Both WCSPH and ISPH methods are implemented and tested for two bluff body examples, namely the square obstacle and airfoil flow problems. Results of WCSPH and ISPH simulations are compared with each other for various test cases and are also validated against the outcomes of the FEM analyses. It is shown that the WCSPH approach can be as reliable as the ISPH if the APDt, density smoothing, corrective SPH formulations, and proper boundary treatments are concurrently employed in the same problem. The improved WCSPH method can correctly model fluid flows at Reynolds numbers as high as ISPH can handle in the laminar flow regime without the necessity of using a Mach number much smaller than 0.1, and without suffering from the common issues related to particle clustering or fracture in the computational domain. As a final remark of the introduction,

even though the APD improves the particle distribution and in turn enables the usage of a lower Mach number and consequently a larger time step, the ISPH method is still superior to WCSPH from the computational time point of view.

## 4.2 Governing equations

In this chapter, a laminar, incompressible, viscous and Newtonian fluid flow is considered. Equations governing fluid problems in hand are the conservation of mass and linear momentum, which are expressed in the Lagrangian form and given in direct notation as

$$\frac{D\rho}{Dt} = -\rho\nabla \cdot \vec{v}, \quad (4.1)$$

$$\rho \frac{D\vec{v}}{Dt} = \nabla \cdot \mathbf{T} + \rho \vec{f}^b, \quad (4.2)$$

where  $\vec{v}$  is the fluid velocity vector,  $\rho$  is the fluid density,  $\mathbf{T}$  is the total stress tensor, and  $\vec{f}^b$  is the body force which is equal to gravitational force in this work. The total stress tensor is defined as  $\mathbf{T} = -p\mathbf{I} + \tau$ , where  $p$  is the absolute pressure,  $\mathbf{I}$  is the identity tensor, and  $\tau = \mu(\nabla\vec{v} + (\nabla\vec{v})^T)$  is the viscous part of the total stress tensor, where  $\mu$  is the dynamic viscosity. Finally,  $\frac{D}{Dt}$  is the material time derivative operator.

## 4.3 Flow around bluff bodies

There are several complex flow phenomena such as separation, circulation and reattachment in many industrial and engineering problems. These phenomena occur in various practical applications like the heat transfer performance of fins, sudden expansion in air-conditioning ducts, flow behaviours in a diffuser, and flow around structures. Flows around a square obstacle and an airfoil are two of the widely used benchmark problems that are appropriate for understanding the aerodynamics and the fundamental characteristics of fluid flows around structures. They are relatively well documented and understood both experimentally and numerically [106, 109, 95] and therefore have become benchmark problems to validate new computational fluid dynamic approaches as

well as to show the capability and the accuracy of developing in-house codes and new algorithms.

The flows around the airfoil and square obstacle placed inside the channel were modelled for a range of Reynolds numbers  $Re = \frac{\rho l_c v_b}{\mu}$  where  $l_c$  is the characteristic length being set equal to the side length for the square obstacle, and  $v_b$  is the bulk flow velocity. The ISPH and WCSPH modelling results are compared in terms of velocity, and pressure contours and Strouhal number for the square obstacle, and the chord length for the airfoil geometry, and the pressure envelope, surface traction forces, and velocity gradients on the airfoil boundaries as well as the lift and drag values for the airfoil.

To be able to test the effectiveness of the improved SPH algorithm for both WCSPH and ISPH approaches (involving the utility of the MBT method together with the APD and the corrective SPH discretization scheme) for modelling fluid flow over complex geometries, we solved two benchmark flow problems, namely, two-dimensional simulations of a flow around a square obstacle and a NACA airfoil. Mass and linear momentum balance equations are solved for both test cases on a rectangular domain with the length and height of  $L = 15m$ , and  $H = 6m$ , respectively.

### 4.3.1 Flow around a square obstacle

A square obstacle with a side dimension of  $0.7m$  is positioned within the computational domain with its center coordinates at  $x = L/3$  and  $y = H/2$ . Initially, a  $349 \times 145$  array (in x-direction and y-direction, respectively) of particles is created in the rectangular domain, and then particles within the square obstacle are removed from the particle array. The boundary particles are created and then distributed on solid boundaries such that their particle spacing is almost the same as the initial particle spacing of the fluid particles.

The simulation parameters, fluid density, dynamic viscosity and body force in x-direction are respectively taken as  $\rho = 1000(\frac{kg}{m^3})$ ,  $\mu = 1(\frac{kg}{ms})$ , and  $|\vec{f}^b| = 3.0 \times 10^{-3}(\frac{N}{kg})$ . The mass of each particle is set equal and found through the relation  $m_i = \frac{\rho_i}{\psi_i}$  and the smoothing length for all particles is chosen equal to 1.6 times the initial particle spacing.

Boundary conditions for inlet and outlet particles are implemented such that particles crossing the outflow boundary are reinserted into the flow domain at the inlet from the

same  $y$ -coordinate positions with the velocity of the inlet fluid region with its coordinates of  $x = 0$ , and  $y = 3$  so that the inlet velocity profile is not poisoned by the outlet velocity profile. The no-slip boundary condition is implemented for the square obstacle. For upper and lower walls bounding the simulation domain, the symmetry boundary condition for the velocity is applied such that  $v = 0$ , and  $\partial u/\partial y = 0$ . The pressure, no-slip and symmetry boundary conditions of relevant fields are implemented on both benchmark problems using the MBT method, which has been explained in detail in [136, 168].

Fig. 4.1 presents the modelling results as contour plots of the velocity magnitude ( $m/s$ ) for the square obstacle problem with Reynolds numbers of 100 (left) and 200 (right), respectively. One can note that the modelling outcomes of both SPH approaches are in a very good agreement with those of the FEM method. In Fig. 4.2 are shown the pressure contours computed by ISPH, FEM and WCSPH methods for the same Reynolds numbers as in Fig. 4.1. It is worthy to accentuate that the WCSPH pressure contours for both Reynolds numbers are as accurate as those of both ISPH and FEM and do not show any oscillatory or noisy behaviour as reported in other relevant literature [84, 29].

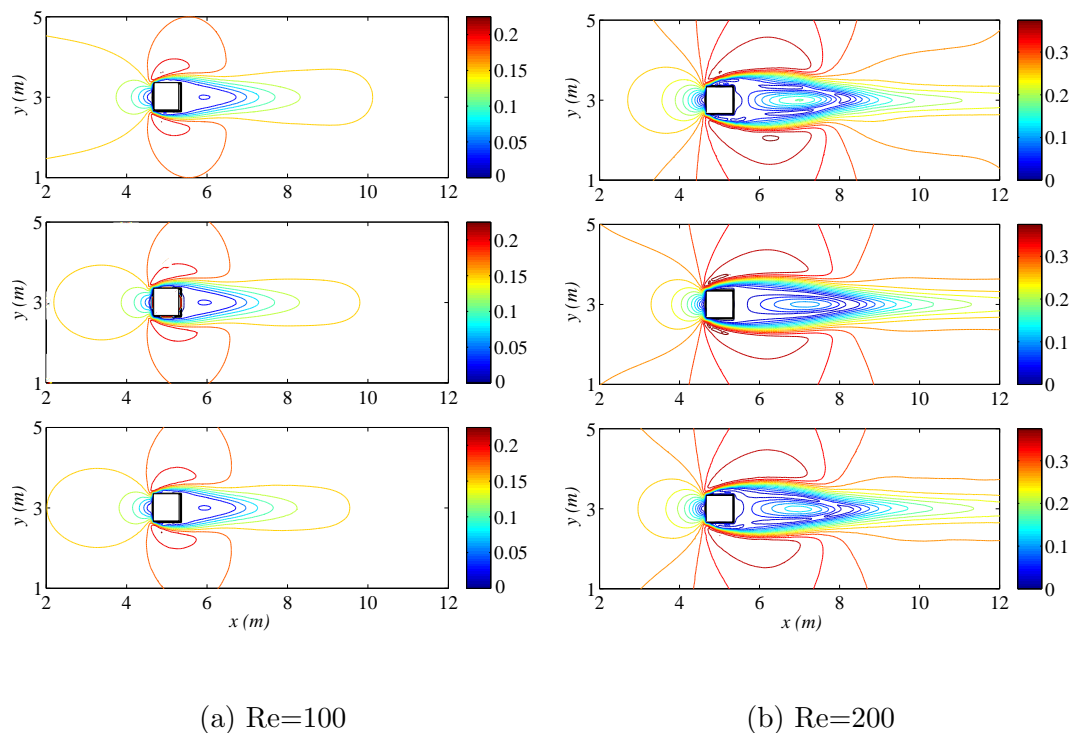


FIGURE 4.1: The comparison of (up) ISPH, (center) FEM and (down) WCSPH simulation results in terms of the contours of the velocity magnitude ( $m/s$ ) for (a)  $Re = 100$  and (b)  $Re = 200$ .

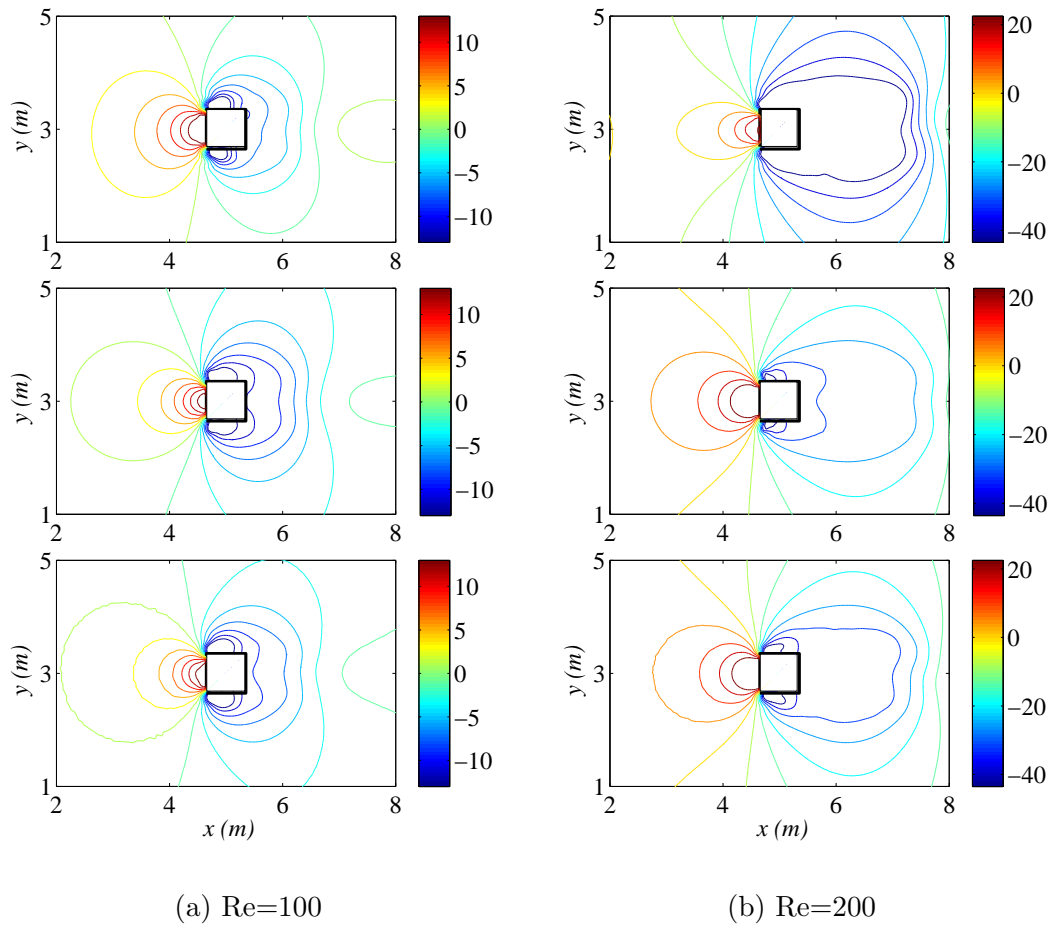


FIGURE 4.2: The comparison of (up) ISPH, (center) FEM and (down) WCSPH pressure contours for (a)  $Re = 100$  and (b)  $Re = 200$ , where pressure unit is Pascal ( $pa$ ).

Early experiments and numerical studies reported the occurrence of vortex shedding at the rear edge of the square obstacle at higher Reynolds numbers [109]. In this direction, to show that both WCSPH and ISPH algorithms proposed in this work are also capable of capturing vortex shedding at the trailing edge of the square obstacle as accurately as mesh dependent solvers, simulation results of WCSPH and ISPH methods are compared with those of FEM in Fig. 4.3 for a Reynolds number of 320 in terms of vortex shedding contours for a full period of shedding. It can be observed that the results are in a good agreement with each other with regard to the magnitude of velocities as well as the position and number of vortices.

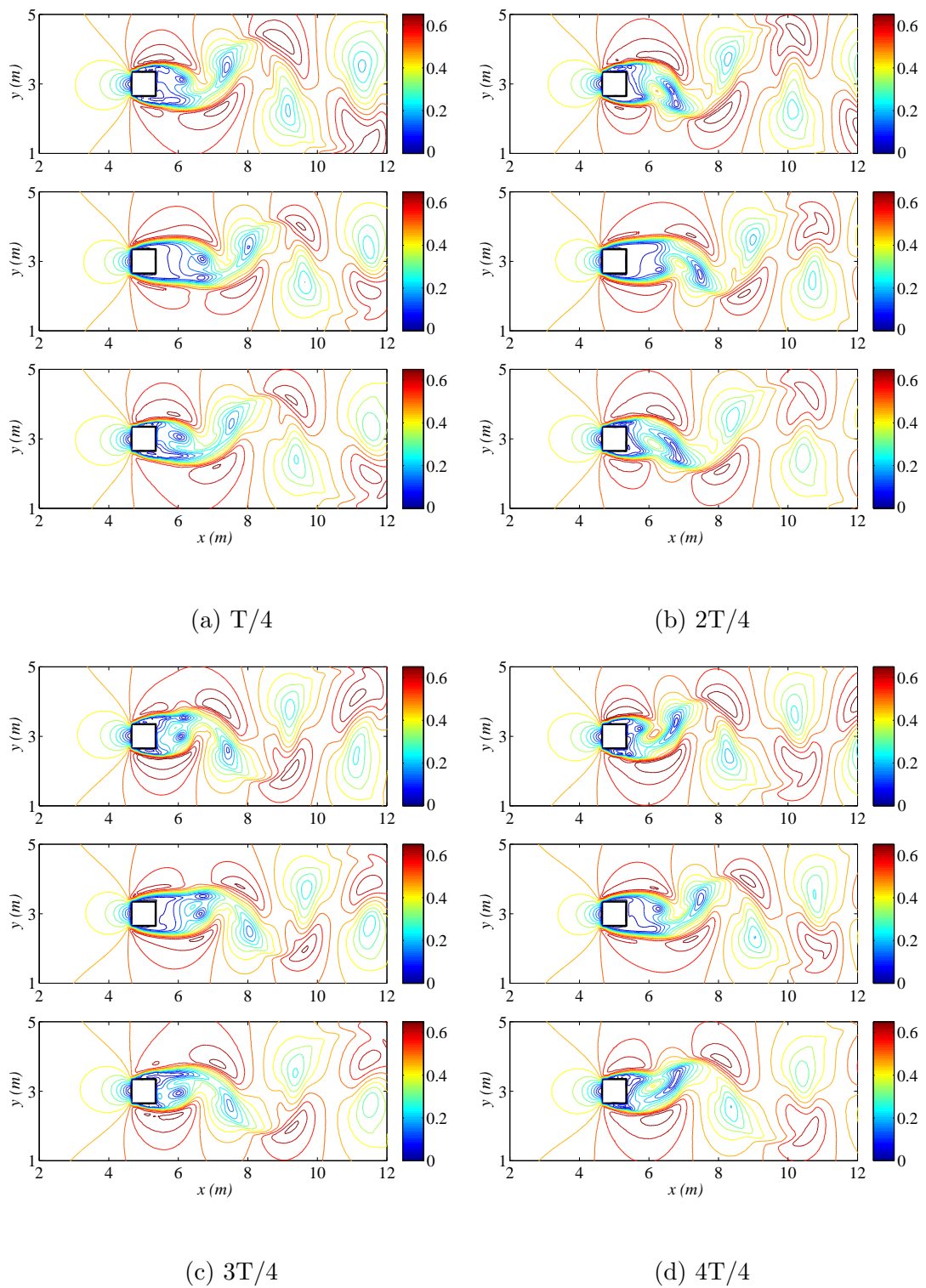


FIGURE 4.3: The comparison of a full period of vortex shedding velocity contours obtained with (up) ISPH, (center) FEM and (down) WCSPH for the Reynolds number of 320.

To further comment on the correctness of the SPH modelling results presented, the Strouhal number  $St = \frac{\omega l_c}{v_b}$  is considered, where  $\omega$  is the frequency of vortex shedding.

The computed values of the Strouhal number for WCSPH and ISPH methods for the Reynolds number of 320 are 0.139 and 0.142, respectively, which are also consistent with the experimental result reported in the literature [109].

### 4.3.2 Flow around a NACA airfoil

The channel geometry and the boundary conditions for the second benchmark problem are identical to the first one with the exception that the square obstacle is replaced by the NACA airfoil with a chord length of  $2m$ , which is created by

$$y_c = \begin{cases} m \left( \frac{2px_c - x_c^2}{p^2} \right), & 0 \leq x_c \leq p \\ m \left( \frac{2p(x_c - 1) + 1 - x_c^2}{1 - p^2} \right), & p \leq x_c \leq 1 \end{cases} \quad (4.3)$$

where  $x_c$  and  $y_c$  are the mean camber line coordinates,  $m$  is the maximum camber in percentage of the chord, which is taken to be 5%, and  $p$  is the position of the maximum camber in percentage of the chord that is set to be 50%. The thickness distribution above and below the mean camber line is calculated as

$$y_t = 5t (0.2969x_c^{0.5} - 0.126x_c - 0.3516x_c^2 + 0.284x_c^3 - 0.1015x_c^4) \quad (4.4)$$

Here,  $t$  is the maximum thickness of the airfoil in percentage of chord, which is 15%. The final coordinates of the airfoil for the upper surface  $(x_U, y_U)$  and the lower surface  $(x_L, y_L)$  are determined using

$$\begin{cases} x_U = x_c - y_t \sin \phi \\ y_U = y_c + y_t \cos \phi \end{cases} \quad (4.5)$$

and

$$\begin{cases} x_L = x_c + y_t \sin \phi \\ y_L = y_c - y_t \cos \phi \end{cases} \quad (4.6)$$

respectively, where  $\phi = \arctan(dy_c/dx)$ . Because the leading edge of the airfoil has a curve with a steeper slope, the chord is split into two parts to be able to locate more boundary particles towards the leading edge. Discrete points on the chord are created with the formula

$$x_c = \left[ \frac{(i-1)}{(ilen-1)} \right]^n \times idis \quad (4.7)$$

where  $i$  is a nodal index,  $ilen$  is the number of nodes along the chord,  $idis$  is the length of the chord, and  $n$  is the geometrical progression coefficient that controls the distance between points on the chord. Given the chord length of 1, six inequidistant nodal points created through the geometrical progression coefficient of 2 are located along 5% of the chord length starting from the leading edge. The remaining section of the chord has 50 equidistant nodal points. The leading edge of the airfoil is located at Cartesian coordinates  $(L/5, H/2)$ .

Having obtained all coordinates of the airfoil geometry, the upper and lower surface lines are curve fitted using the least squares method of order six. In so doing, it becomes possible to compute boundary unit normals, tangents and slopes for each boundary particles. An array of  $300 \times 125$  particles in  $x$  and  $y$ -directions, respectively, is created in the rectangular domain. All the initial particles falling between fitted curves for upper and lower cambers are removed from the rectangular computational domain, and then the remaining fluid particles are combined with the boundary particles to form a particle array of the computational domain. The smoothing length for all particles is set equal to 1.6 times the initial particle spacing. To show convergence, three different particle arrays, namely,  $150 \times 62$  (coarse),  $300 \times 125$  (intermediate) and  $400 \times 167$  (fine) were used. It was observed that  $300 \times 125$  array of particles is sufficient for particle number independent solutions.

After demonstrating the competence and success of the improved ISPH and WCSPH algorithms on a geometry with sharp corners, the proposed algorithm was also tested on a more general and complex geometry with curved boundaries and a thin body section. The sensitivity of the numerical solutions to particle numbers and the convergence of the present modelling have been recently investigated by Shadloo et al.[136] for the ISPH method as well as the FEM. Therefore, a comprehensive validation is not repeated

here. Instead, the emphasis is placed on the validation of the numerical scheme for the WCSPH method. To do this, the velocity fields over the airfoil with the same values of the parameters were computed (Fig. 4.4) on three different sets of particles (i.e.  $150 \times 62$  (coarse),  $300 \times 125$  (intermediate) and  $400 \times 167$  (fine)).

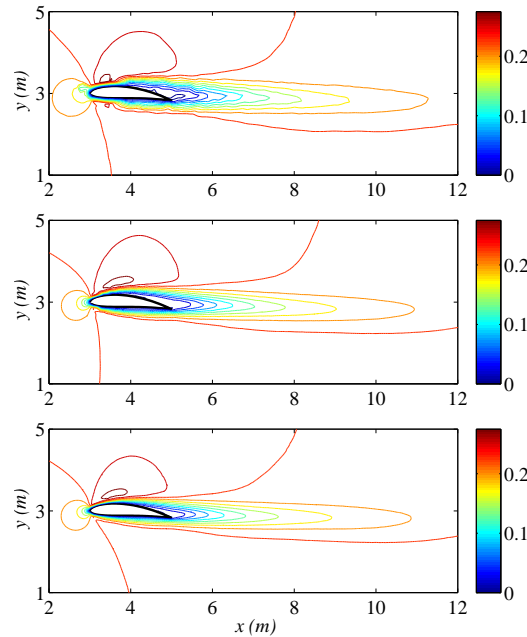


FIGURE 4.4: The velocity fields in terms of velocity magnitudes over the airfoil (with an angle of attack of  $5^\circ$  at Reynolds number of 420) computed on three different sets of particles by the WCSPH method, namely  $150 \times 62$  (coarse),  $300 \times 125$  (intermediate) and  $400 \times 167$  (fine), for which results are given from top to bottom, respectively.

The comparison of results on the coarse, medium and fine particle numbers clearly indicates that the intermediate particle number can produce numerical results with satisfactory accuracy given the trade-off between computational costs and capturing flow characteristics of interest. Because finer meshes are computationally expensive, the intermediate particle number is chosen for the numerical simulations presented in this work. The simulations are performed on a workstation using an Intel  $\text{\textcircled{R}}$  *Core<sup>TM</sup>* i7-950 Processor (8M Cache, 3.06 GHz, 4.80 GT/s) under a WINDOWS XP (64-Bit Edition) operating system. The computational cost in terms of the CPU time for the coarse, intermediate and fine particle numbers for one second of the real simulation time is shown in table 4.1.

TABLE 4.1: The computational cost in terms of the CPU time for the coarse, intermediate and fine particle numbers for one second of the real simulation time for the ISPH and WCSPH method. The reported unit is second.

	coarse	intermediate	fine
ISPH	21.2s	85.6s	159.2s
WCSPH	128.9s	1352.8s	2651.3s

Figs. 4.5 and 4.6 compare the velocity contours of (up) ISPH, (center) FEM and (down) WCSPH for the angles of attack of  $5^\circ$  and  $15^\circ$  respectively (contours show the velocity magnitude,  $(m/s)$ ) for the Reynolds numbers of 420 (left) and 570 (right). Similar to the previous benchmark problem, both WCSPH and ISPH results are in good agreement with those of the mesh dependent FEM technique. In all simulations, the results of WCSPH are as accurate as the ISPH ones. The figures further illustrate that the proposed algorithm is also very successful in simulating the flow around the airfoil geometry with different angles of attack across the flow field.

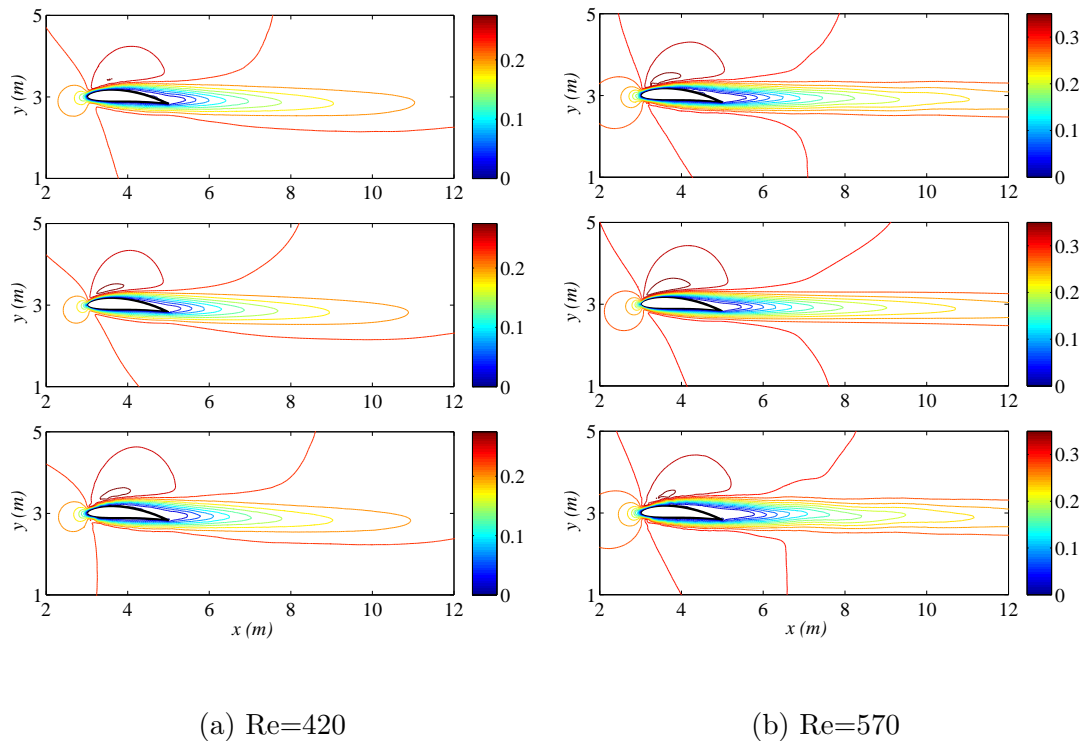


FIGURE 4.5: The comparison of (up) ISPH, (center) FEM and (down) WCSPH velocity contours for the angle of attack of  $5^\circ$  at (a)  $Re = 420$  and (b)  $Re = 570$ .

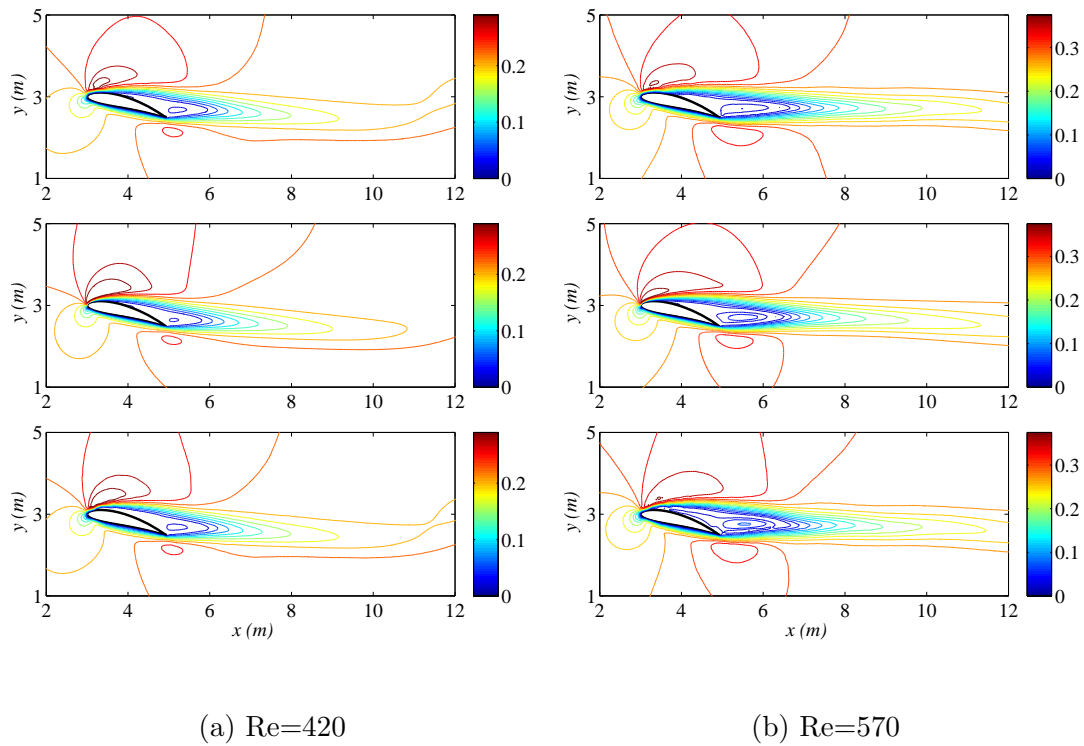


FIGURE 4.6: The comparison of (up) ISPH, (center) FEM and (down) WCSPH velocity contours for the angle of attack of  $15^\circ$  at (a)  $Re = 420$  and (b)  $Re = 570$ .

Fig. 4.7 provides a comparison for the WCSPH, ISPH and FEM pressure envelopes around the airfoil for the angle of attack of  $15^\circ$  with the Reynolds numbers of 420 (left) and 570 (right). The results of both SPH approaches are consistent with those corresponding to the mesh dependent solver. It is noted that the WCSPH pressure envelop is more accurate and is in a closer agreement with the FEM method than that of ISPH, especially at the higher Reynolds number. Observing the figures, one can notice that there is a small discrepancy in pressure values compared with the FEM results for the upper camber in the vicinity of the leading edge and the stagnation point. Also, the x-coordinates of minimum pressure for both WCSPH and ISPH methods are slightly greater than that of the FEM method. These discrepancies in pressure values might be attributed to the dynamic nature of the SPH method because fluid particles are in continuous motion. This local temporary scarcity of particles near the solid boundaries might deteriorate the accuracy of the computed pressure because the SPH gradient discretization scheme is rather sensitive to the particle deficiencies within the influence domain of the smoothing kernel function.

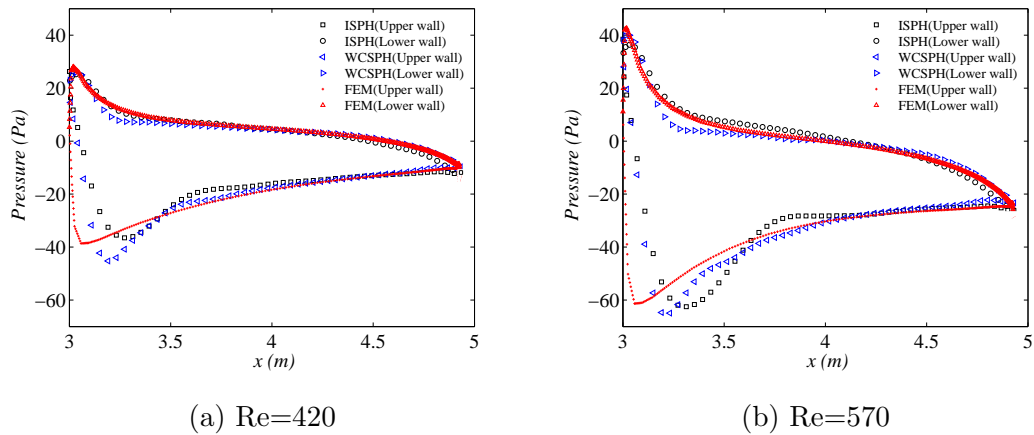


FIGURE 4.7: The comparison of pressure envelopes for the angle of attack of  $15^\circ$  at (a)  $Re = 420$  (left) and (b)  $Re = 570$  (right).

To have an additional quantitative comparison between the proposed SPH methods and the FEM analysis, the total surface force  $\vec{F} = \mathbf{T} \cdot \vec{n} da$  acting on the upper and the lower cambers are plotted as a function of the chord length, as denoted in Fig.4.8 where  $da$  is the area of a surface element. One can notice that there exist similar discrepancies in total surface forces between SPH and FEM results as in the case of pressure values. This is due to the fact that at this Reynolds number range, the pressure force is dominant over the viscous forces.

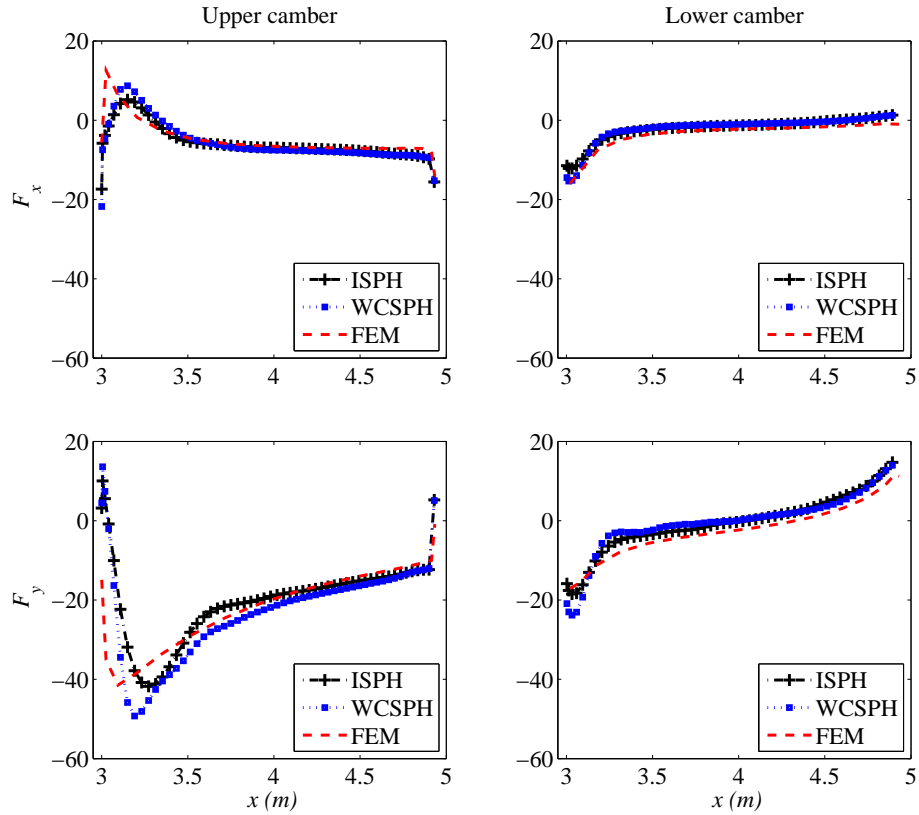


FIGURE 4.8: The comparison of total forces on the upper and lower cambers of the airfoil for the angle of attack of  $15^\circ$  at  $Re = 420$ .

Fig. 4.9 illustrates the components of the velocity gradient on the airfoil boundary for the upper camber. Upon integrating the  $x$ -component and  $y$ -component of the total surface force over the airfoil, one can calculate the lift and drag forces, respectively. The lift and drag forces acting on the airfoil with the angle of attack of  $15^\circ$  for the Reynolds numbers of 420 and 570 are reported in table 4.2. Given the difficulty of having more particles in the vicinity of the airfoil boundaries in the SPH method unlike the mesh-dependent methods because of the dynamic nature of SPH particles, satisfactorily good agreement is observed between SPH and FEM results.

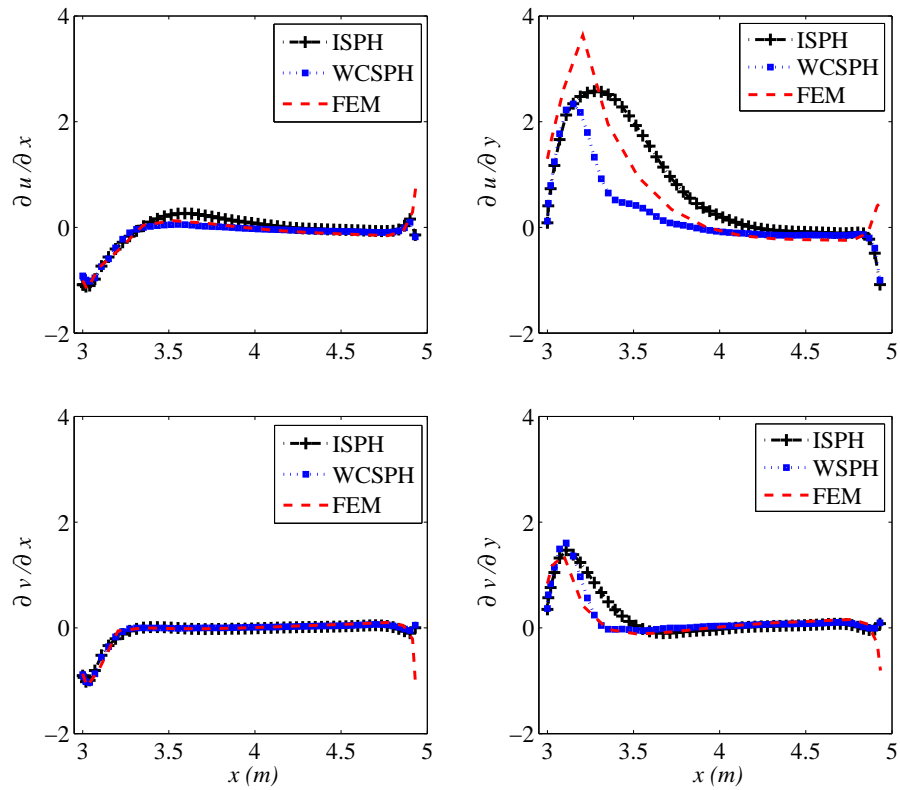


FIGURE 4.9: The comparison of the components of the velocity gradient on the upper camber of the airfoil with the angle of attack of  $15^\circ$  at  $Re = 420$ .

TABLE 4.2: The lift and drag forces acting on the airfoil with the angle of attack of  $15^\circ$  at  $Re = 420$  and  $Re = 570$ .

	ISPH		FEM		WCSPH	
Re	Lift	Drag	Lift	Drag	Lift	Drag
420	43.218	16.9709	52.0167	17.5942	49.2342	16.5904
570	66.4510	26.4433	69.9198	25.9040	62.9650	24.4302

Fig. 4.10 presents the close-up view of particle positions around airfoils with the angle of attack of  $15^\circ$  and Reynolds numbers of 570 (left) and 1400 (right) for the ISPH and WCSPH methods. Incompressibility condition is enforced more accurately in the ISPH method than in the WCSPH method. Therefore, particles in the WCSPH method do not have a strong tendency to follow the streamline trajectory. As a consequence, the WCSPH technique does not suffer from particle deficiency around the upper camber as much as ISPH. These figures also illustrate the effectiveness of using the MBT method

to treat difficult geometries, which might not be achievable with other boundary treatment methods proposed for meshless numerical approaches. For both the low and high Reynolds number values (i.e.  $Re = 570$ , and  $Re = 1400$ ) there are no particle deficiencies in the domains of interest for the WCSPH method.

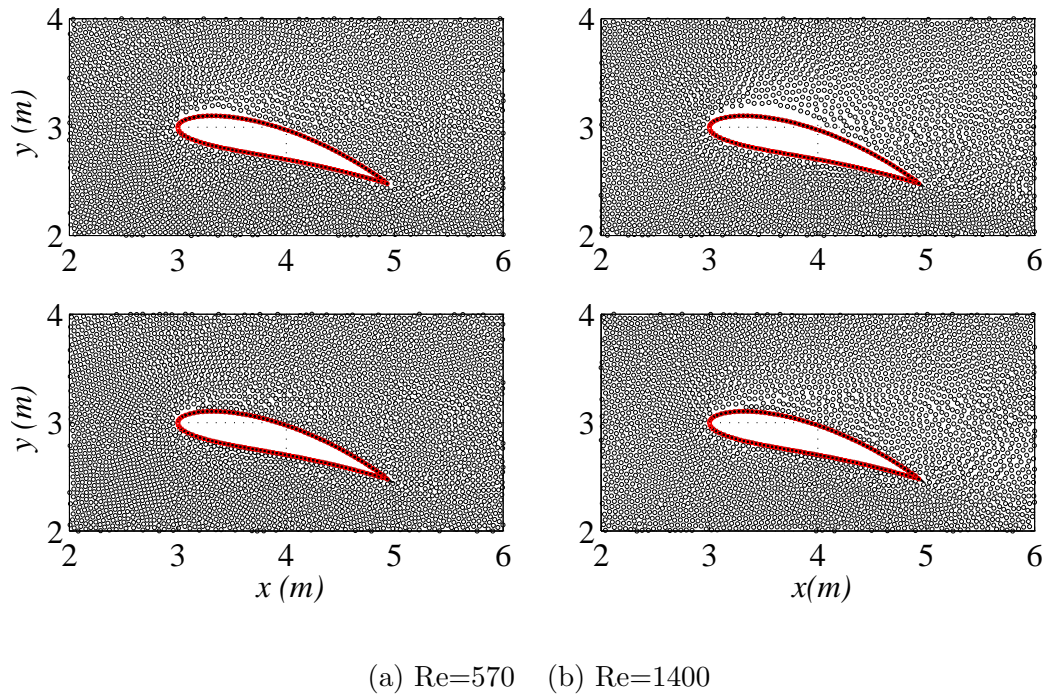


FIGURE 4.10: The close-up view of particle positions around airfoils with the angle of attack of  $15^\circ$  at (a)  $Re = 570$  and (b)  $Re = 1400$  for ISPH (up) and WCSPH (down) methods, respectively.

It is noteworthy to emphasize that without the APD algorithm presented and implemented in this work, nonphysical particle fractures occur around the airfoil geometry because of the relatively high velocity and the tendency of SPH particles to follow a streamline trajectory as illustrated in Fig.4.11. This brings about erroneous density, pressure and velocity fields and in turn blows up the simulations even for relatively small Reynolds numbers (i.e.  $Re = 100 - 300$ ) and angle of attack values. In passing, it should be mentioned that within the scope of this work, the artificial stress method [101, 53] has also been considered and implemented as a possible remedy for particle fractures for both the ISPH and the WCSPH techniques. It was observed that the artificial stress method could partially eliminate particle clustering and associated instabilities in computational domains and is effective only up to a Reynolds number of roughly 120. This may lead one to conclude that the particle disorderliness has a significant effect on the existence of numerical instabilities in the SPH method.

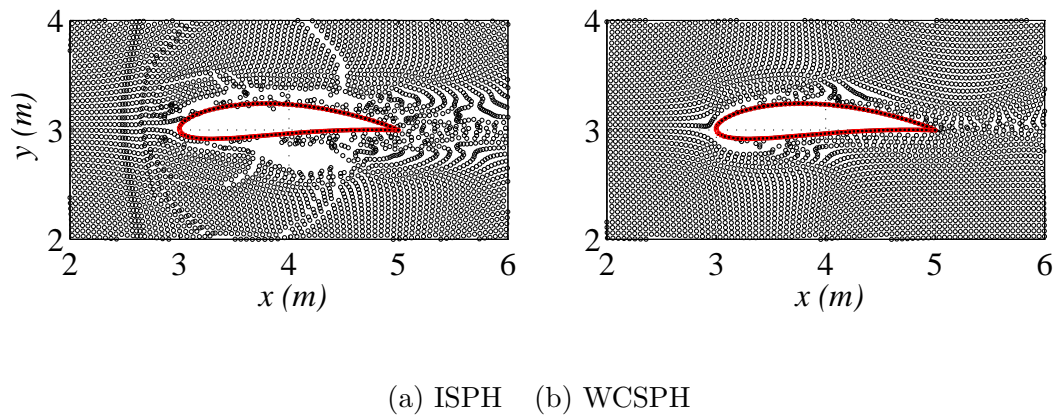


FIGURE 4.11: The close-up view of particle positions around airfoils with the angle of attack of  $5^\circ$  at  $Re = 300$  without using the APD method for (a) ISPH and (b) WCSPH methods.

Another approach to avert the formation of particle clustering and fractured domains in the WCSPH method is to increase the speed of sound value. Although this treatment might be a remedy for void formations as also reported in [74, 84], it increases the computational cost significantly. For example, the computational costs to achieve one second of the real time simulation are 4665.7 s, 1352.8 s, 1069.8 s, and 761.2 s in terms of CPU time for large ( $M = 0.025$ ), default ( $M = 0.1$ ), small ( $M = 0.173$ ), and very small ( $M = 0.316$ ) sound speeds, respectively. The large and default speed of sound values keep the density variation less than 1%, and small and very small speed of sound values are chosen such that the density variation is less than 3% and 10% in that order. In Fig. 4.12 are given particle distributions and the contour plots for the density field corresponding to default, small and very small speed of sound values. One can see that the APD permits the usage of much smaller sound speed values without the concern of any fractured regions in particle distribution. Despite the fact that small and very small sound speed values do not cause any noticeable problem in the particle distribution, they cannot enforce the incompressibility. Therefore, the sound speed value referred to as the default has been used to generate all the reported WCSPH results in this work.

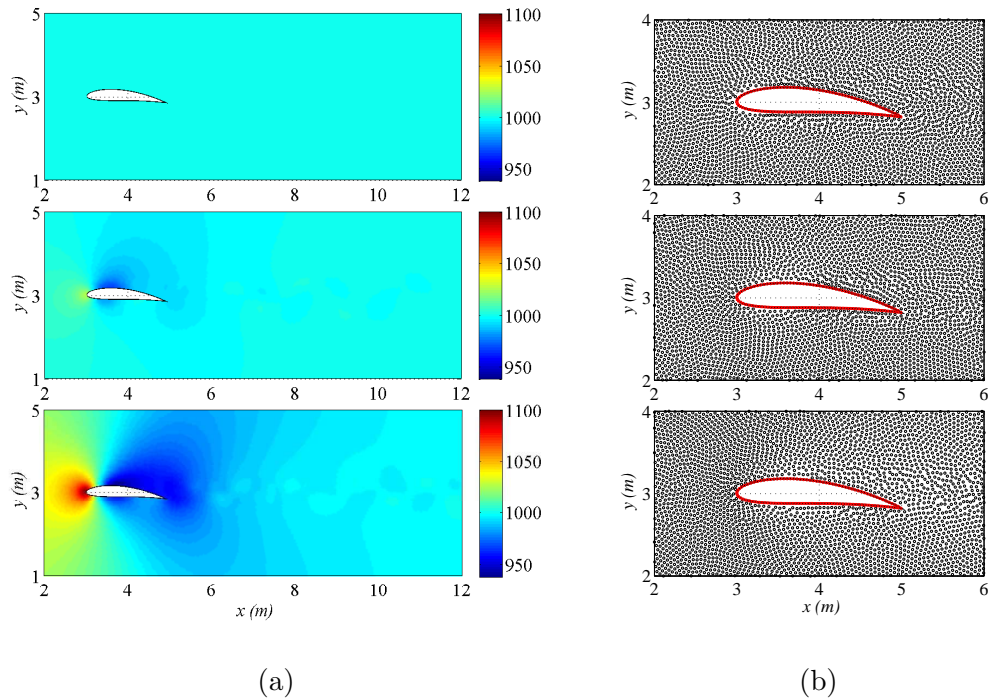


FIGURE 4.12: (a) The density contours and (b) corresponding particle distributions (right) around the airfoils obtained with the WCSPH method with the angle of attack of  $5^\circ$  at  $Re = 1000$ .

Having shown that the WCSPH algorithm presented in this work can simulate fluid flow around the bluff bodies as successfully and accurately as ISPH and FEM, for the sake of completeness, it is prudent and valuable to show that it can also model laminar fluid flow over bluff bodies with high Reynolds number values. Fig. 4.13 shows a snapshot of the vortex shedding contours produced by WCSPH (up) and FEM (down) methods for the angle of attack of  $5^\circ$  and the Reynolds number of 1400 (colors denote the velocity magnitude ( $m/s$ )). As in the case of the presented square obstacle results, the WCSPH result is also satisfactorily in agreement with FEM regarding the magnitude of velocities as well as the position and number of vortices for the airfoil geometry.

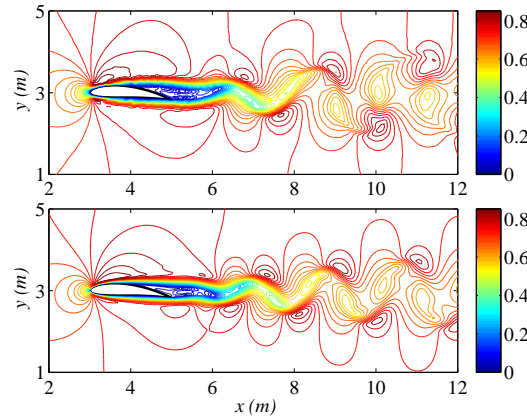


FIGURE 4.13: The comparison of vortex shedding contours produced by (up) WCSPH and (down) FEM methods for the angle of attack of  $5^\circ$  at  $Re = 1400$ .

### 4.3.3 Conclusion

In this section, solutions for flow over an airfoil and square obstacle are presented to demonstrate that the WCSPH and ISPH algorithms integrated concomitantly with the MBT and APD methods as well as the corrective SPH discretization scheme can simulate flow around complex geometries accurately and reliably. The WCSPH and ISPH results were compared in terms of velocity and pressure contours and Strouhal number for the former benchmark problem, and velocity contours, the pressure envelope, surface traction forces, and velocity gradients on the airfoil boundaries as well as the lift and drag values for the latter one. Simulation results for both SPH methods were validated using the FEM method. Excellent agreements among the results were observed. It was demonstrated that the improved WCSPH method is able to capture the complex physics of bluff-body flows such as flow separation, wake formation at the trailing edge, and vortex shedding as accurately as the ISPH method without experiencing any particle clustering and fracture problems. It has been documented in the SPH open literature that the WCSPH method may not estimate pressure fields reliably and is believed to produce noisy and oscillatory pressure fields. It is further considered that if a relatively low speed of sound value is used, the WCSPH method cannot simulate flow problems with high Reynolds number values and leads to the occurrence of void regions in the computational domain. It was shown that with the proper and judicious implementation of the proposed algorithms, for all Reynolds numbers in the laminar regimes, the WCSPH technique can provide stable simulations and accurate results without any noticeable

noise in pressure values. Also, the Mach number equal to 0.1 satisfactorily enforces the fluid incompressibility condition with the density variation less than 1%.

# Chapter 5

## Two Phase Flows

### 5.1 Introduction

In this chapter, we have modeled several challenging two phase flow problems, namely, square bubble deformation under and without the effect of surface tension force, Laplace's law, and Kelvin-Helmholtz instability, and Rayleigh-Taylor instability. The outcomes of our numerical solutions are validated against available numerical data in literature, and excellent agreement is observed between the current SPH and literature results.

### 5.2 Governing equations

We consider Newtonian, viscous, incompressible, and immiscible two-phase system. The governing equations for such a system are the conservation of mass and linear momentum, which are respectively formulated in Lagrangian form as

$$\frac{D\rho}{Dt} = -\rho\nabla \cdot \vec{v}, \quad (5.1)$$

$$\rho \frac{D\vec{v}}{Dt} = \nabla \cdot \mathbf{T} + \rho \vec{f}^b + \vec{f}^v, \quad (5.2)$$

where  $\vec{v}$  is the fluid velocity vector,  $\rho$  is the fluid density,  $\mathbf{T}$  is the total stress tensor,  $\vec{f}^b$  is the body force which is equal to gravitational force in this work, and  $\vec{f}^v$  is the

volumetric surface tension force. The total stress tensor is defined as  $\mathbf{T} = -p\mathbf{I} + \tau$ , where  $p$  is the absolute pressure,  $\mathbf{I}$  is the identity tensor, and  $\tau = \mu(\nabla\vec{v} + (\nabla\vec{v})^T)$  is the viscous part of the total stress tensor, where  $\mu$  is the dynamic viscosity. Finally,  $\frac{D}{Dt}$  is the material time derivative operator.

### 5.3 Interface treatment

The mass and momentum balance equations on the discontinuity surfaces can be formulated respectively as

$$\|\rho(\vec{v} - \vec{u})\| \cdot \vec{n} = 0, \quad (5.3)$$

and

$$\|\rho\vec{v}(\vec{v} - \vec{u}) - \mathbf{T}\| \cdot \vec{n} = \nabla_{(s)}\sigma + \kappa\sigma\vec{n}, \quad (5.4)$$

or in a component form

$$\|\rho(v_k - u_k)\| n_k = 0, \quad (5.5)$$

and

$$\|\rho v_l(v_k - u_k) - T_{kl}\| n_k = \sigma_{,k}P_{kl} + \kappa\sigma n_l. \quad (5.6)$$

The symbol  $\|\ \|$  indicates the jump of the enclosed quantities across the discontinuity surface; for instance,  $\|\varphi\| = \varphi^+ - \varphi^-$  where  $\varphi^+$  and  $\varphi^-$  are the values of  $\varphi$  on the positive and negative sides of the discontinuity surface,  $\vec{u}$  is the velocity of the discontinuity surface,  $\vec{n}$  is the unit normal to the discontinuity surface,  $\nabla_{(s)}$  is the surface gradient operator,  $\sigma$  is the surface tension, and  $\kappa$  is the curvature.

Assuming that the discontinuity surface is a material interface (which requires that  $v_k = u_k$ ), and the momentum flux is continuous across the fluid-fluid interface, and

finally the surface tension is independent of the position on the interface, the interface mass balance is satisfied identically, and the momentum balance on the interface reduces to

$$\|p\| \cdot \vec{n} = \vec{f}^s = \sigma \kappa \vec{n}. \quad (5.7)$$

For computational simplicity and efficiency, it is preferable to express this local surface force as an equivalent volumetric force  $\vec{f}^v$  (the force per unit volume) as is done in the Continuum Surface Force (CSF) method originally proposed by Brackbill et al. in [13]. The basic concept behind this approach is to replace the sharp interface between two fluids with the transition region of finite thickness (see Fig. 5.1). This can be realized through multiplying the local surface tension force with a surface delta function as

$$\vec{f}^v = \sigma \kappa \delta^s \vec{n}, \quad (5.8)$$

The volumetric surface tension force  $\vec{f}^v$  acts only on the interface in the unit normal direction thereby reducing the total surface energy and the surface area, and vanishes in the bulk of the fluid. The effect of interfacial surface tension is consequently included in the computational model in the form of an external force term.

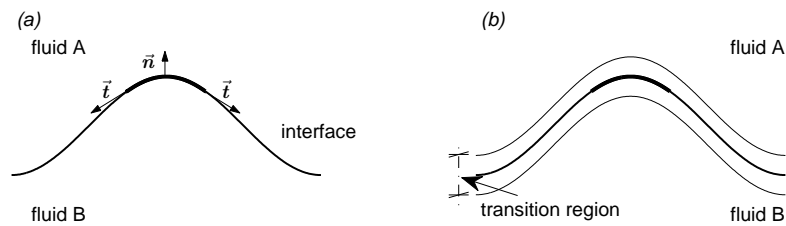


FIGURE 5.1: Replacing the sharp interface between two fluids with the transition region of finite thickness.

To be able to distinguish among constituents of an immiscible multiphase system, and calculate relevant interface fields (i.e., the interface unit normal, curvature, and interfacial forces), each particle is assigned to color function such that  $c = 0$  for fluid *A* and  $c = 1$  for fluid *B*. To avoid sharp variations in the color function across the interface, the color function for each particle is smoothed as

$$C_{\mathbf{i}} = \frac{\sum_{\mathbf{j}} W_{\mathbf{ij}} c_{\mathbf{j}}}{\sum_{\mathbf{j}} W_{\mathbf{ij}}}. \quad (5.9)$$

Here, it should be noted that the smoothed color function  $C_{\mathbf{i}}$  effectively represents the volume fraction of fluid  $B$ , namely,  $C_{\mathbf{i}}^B = C_{\mathbf{i}}$  and  $C_{\mathbf{i}}^A = 1 - C_{\mathbf{i}}$  wherewith one can write  $\sum_{\alpha} C_{\mathbf{i}}^{\alpha} = 1$  where  $C_{\mathbf{i}}^{\alpha}$  is the smoothed color function of  $\alpha$  th phase.

Since each fluid particle has constant transport properties which are discontinuous across the interface, the numerical scheme might have instabilities especially in the case of a large mismatch in the transport parameters of constituents. Hence, it is practical to smooth the density and the viscosity of fluids through using a weighted arithmetic mean interpolation. Upon using smoothed color function, the density and viscosity of the multiphase system can be calculated from those of constituents respectively as

$$\chi_{\mathbf{i}} = (1 - C_{\mathbf{i}})\chi^A + C_{\mathbf{i}}\chi^B, \quad (5.10)$$

where  $\chi$  can be any particle's properties such as density ( $\rho$ ), viscosity ( $\mu$ ), and/or electrical permittivity ( $\varepsilon^E$ ) or conductivity ( $\sigma^E$ ).

The unit normal vector  $\vec{\mathbf{n}}$  for particle  $\mathbf{i}$  can be calculated as

$$\vec{\mathbf{n}} = \frac{\nabla C}{|\nabla C|}. \quad (5.11)$$

Unit normals in the vicinity of fringes of the interface might be erroneous and in turn may produce faulty results when they are used in the computation of the curvature. Therefore, a constraint is required to determine reliable normals as also pointed out in [104]. In this direction, the constraint in the form of  $|\nabla C_{\mathbf{i}}| > \epsilon/h$  is employed. Here,  $\epsilon$  is a constant used to control the thickness of the interface, which is set to be  $\epsilon = 0.08$  in this work. Particles satisfying this condition are regarded to be interface particles with reliable unit normals.

Further, upon using only these reliable normals, the curvature for particle  $\mathbf{i}$  is calculated as

$$\kappa = -\nabla \cdot \vec{n}. \quad (5.12)$$

Finally, substituting Eqs. (5.11) and (5.12) into Eq. (5.8), one can rewrite the volumetric surface force as,

$$\vec{f}^v = -\sigma \nabla \cdot \left( \frac{\nabla C}{|\nabla C|} \right) \nabla C. \quad (5.13)$$

## 5.4 Benchmarking

### 5.4.1 Square-droplet deformation

To be able to show the effect of the interface thickness on the accuracy of the computed interface curvature, a two-dimensional simulation for a square-droplet deformation under the influence of the surface tension force is considered where the two-fluid system has density and viscosity ratios of one, namely ( $\rho_2/\rho_1 = 1$ ,  $\rho_1 = 1(\frac{kg}{m^3})$ ) and ( $\mu_2/\mu_1 = 1$ ,  $\mu_1 = 1(Pa.s)$ ), respectively. The initial square-droplet with a side length of  $1m$  is placed at the center of the square domain with a side length of  $2(m)$ . A  $100 \times 100$  array of particles is distributed on a regular lattice. Upon the application of a constant surface tension ( $\sigma = 1$ ) on the two-fluid system interface, the initial square-droplet starts deforming into a circular shape in order to reduce its surface energy and surface area. This problem has been solved with two different interface thicknesses, namely, four and two rows of interface particles from each fluid side, which is referred to as thick and thin interface configurations, respectively. Figure 5.2 shows the initial ( $t = 0(s)$ ) and the final ( $t = 1(s)$ ) shapes of the square-droplet with a thin interface.

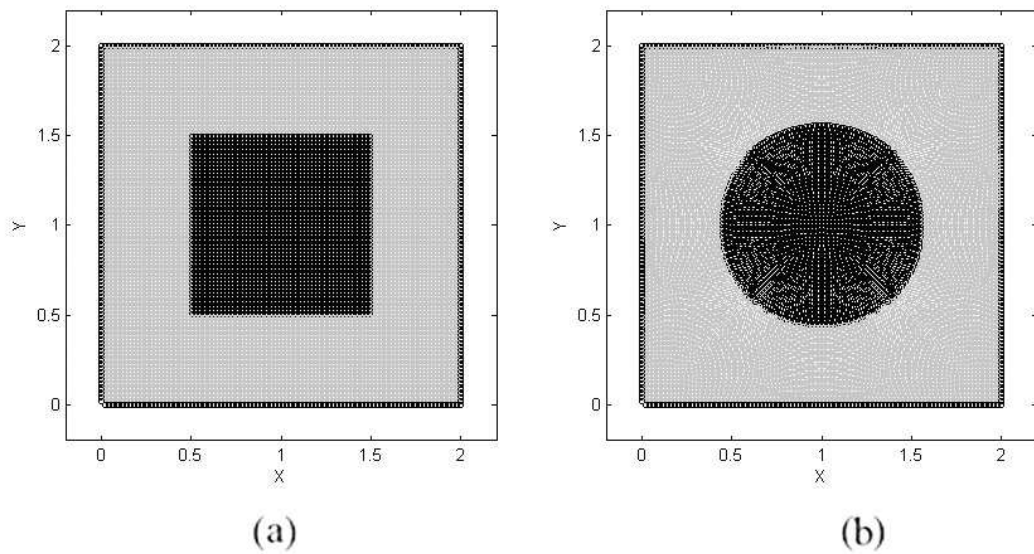


FIGURE 5.2: The initial (a)  $t = 0(s)$  and the final (b)  $t = 1(s)$  shapes of the square-droplet problem with thin interface.

Figure 5.3 presents the variation of the interface curvature as a function of the radius of the deformed droplet and also illustrates the form of the Dirac delta function for the thick and thin interfaces at ( $t = 1(s)$ ). The Dirac delta function is plotted along the vertical line starting at the geometrical location of ( $x = 1, y = 1$ ) and ending at ( $x = 1, y = 2$ ) in Fig. 5.2b. It should be noted that the integration of the Dirac delta function for both cases over the associated thickness of the interface produces unity. It can be inferred from Fig. 5.3 that the thicker the interface, the more oscillatory and inaccurate the curvature values in the vicinity of the interface fringes. Therefore, the surface tension force is to have more erroneous values in the vicinity of the interface fringes for the thick interface than for the thin one due to the multiplication of the Dirac delta function with the curvature.

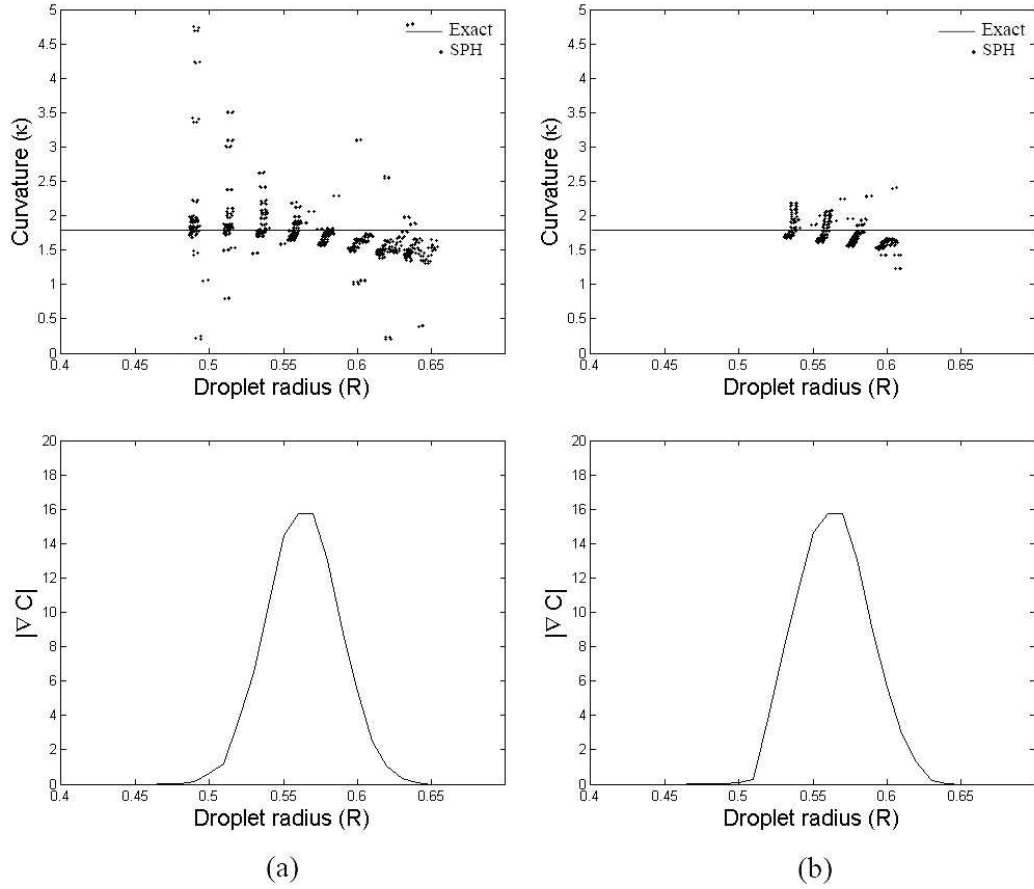


FIGURE 5.3: Interface curvature versus droplet radius and the form of the Dirac delta function at the final time ( $t = 1(s)$ ) for the square-droplet deformation problem; (a) thick interface, (b) thin interface.

#### 5.4.2 Laplace's law

A static circular bubble is a commonly used test case for validating the accuracy of numerically computed pressure jump across the interface in multiphase systems since it has a simple analytical solution, ( $p_{in} - p_{out} = \sigma/r$ ), widely referred to as Laplace's law for a stationary droplet [108, 47]. The computational domain for this test case is a unit square with  $H$  denoting the edge length and a circular bubble with a radius of  $r = 0.25(m)$  is placed at the center of the unit square domain ( $H = 1(m)$ , see Fig. 5.4a). It is represented by an array of 100 by 100 particles in  $x$ - and  $y$ - directions, and the smoothing length for all particles is set equal to 1.6 times the initial particle spacing.

The simulation parameters are density, viscosity and surface tension coefficient with the numerical values of  $\rho_1 = \rho_2 = 1000(\frac{kg}{m^3})$ ,  $\mu_1 = \mu_2 = 1(Pa.s)$  and  $\sigma = 0.25(\frac{N}{m})$ , respectively. The utilized model parameters, namely, the radius of the bubble and the

surface tension should lead to pressure jump of unity on the interface in accordance with the Laplace relation  $p_{in} - p_{out} = 1(Pa)$ . As for the boundary conditions, the pressure on the boundaries are set equal to zero, and no-slip boundary condition is imposed for velocity on all solid walls. The initial velocity field is zero.

As stated previously, in the numerical modeling of multiphase flows, the physically sharp interface is approximated by a transition region of a finite thickness, and the surface tension force is included in the momentum balance equation as a volumetric force that is active only over this finite interface thickness through the usage of Dirac delta function. Thus, it is numerically impossible to reproduce sharp or exact pressure jump as in the case of analytical solution [108] since the pressure jump across the interface is smoothed. The existence of this smoothed pressure gradient, and also the slight variation of curvature along the perimeter of the circular bubble due to the discrete nature of the numerical approach induce spurious or parasite currents which are observed as vortices in the vicinity of interface despite the absence of any external force. Not only are they inherent to the CSF method but also observed in other surface tension methods [133, 82]. Figure 5.4b presents the computed pressure field for the over all domain.

Figure 5.5 illustrates the locations of the spurious currents in the neighborhood of the interface for two different mesh resolutions for the first time step. It is seen from the figure that the spurious current can be alleviated through the mesh refinement. In spite of the spurious current, it is observed that the computed pressure gradient across the interface is equal to  $p_{in} - p_{out} = 1.004(pa)$  which is in a good agreement with the analytical result. Here, the pressure inside and outside the bubble is calculated by averaging the pressure fields of particles for fluids 2 and 1 which are far enough from the interface. Since the parasitic current in this test case in the energy point of view is at least two order of magnitude lower than the applied surface tension force, it does not create any serious effect on the results; nevertheless, in some problems, force due to the spurious effect might be comparable to other physical forces such as viscous, gravitational, and surface tension forces, among others, thereby leading to over/underestimated erroneous values in computational results.

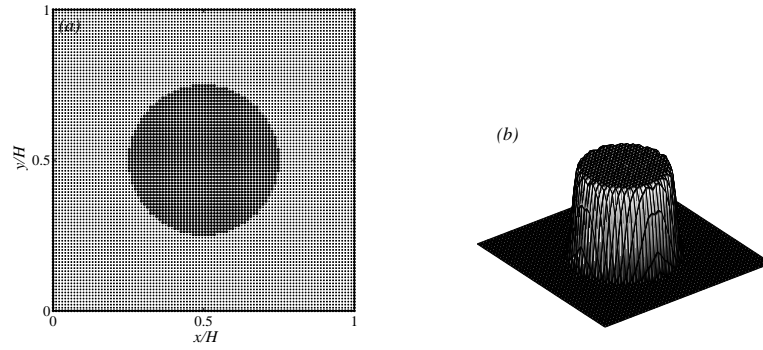


FIGURE 5.4: (a) Initial particle distribution for the circular droplet (fluid-2) surrounded by the background fluid (fluid-1) (b) pressure field for the over all domain. The particle resolution is  $100 \times 100$ .

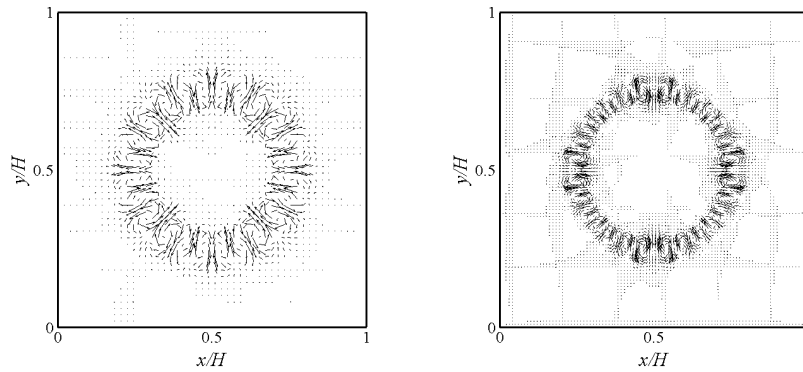


FIGURE 5.5: The locations of the spurious currents in the neighborhood of the interface for the particle resolutions of (a)  $50 \times 50$  and (b)  $100 \times 100$ .

To show the convergence of the numerical model, in table 6.1 are given the  $L_1$  and  $L_2$  norms of the velocity magnitude for the same time step, which are respectively defined as  $L_1 = \sum_i^N |\vec{v}|/N$  and  $L_2 = \sqrt{\sum_i^N |\vec{v}|^2/N^2}$ . Given that the simulation starts with zero initial velocity field, the interface velocities after the first time step are a direct measure for the error in the pressure fields. As seen from table 6.1, as the particle resolution increases, both  $L_1$  and  $L_2$  norms decrease, which indicates the convergence due to the particle refinement.

### 5.4.3 Square droplet

The presence of velocity field on the interface of two fluids in absence of any external forces due to the jump in the density of phases across the interface is known as artificial

TABLE 5.1: The  $L_1$  and  $L_2$  norms of velocity magnitude after the first time step.

Particle resolution	$L_1$ Norm	$L_2$ Norm
$25 \times 25$	8.64 e-6	1.64 e-6
$50 \times 50$	4.64 e-6	6.4 e-7
$100 \times 100$	3.64 e-6	2.4 e-7
$200 \times 200$	2.64 e-6	1.35 e-7

surface tension [65]. This is an undesired non-physical phenomenon which is directly related to the discretization scheme and the treatment of density discontinuity. The artificial surface tension can introduce some error into the model thereby leading to inaccurate calculation of curvature, and the formation of unphysical flow across the interface. Square droplet problem is one of the simplest test cases which can be used effectively to demonstrate if the artificial surface tension exists in the solution domain. For this benchmark problem, the domain geometry and the boundary conditions are identical to the previous example except that the bubble is replaced by a square droplet. The density ratio of phases is  $\rho_2/\rho_1 = 5$  where  $\rho_1 = 1000(\frac{kg}{m^3})$  and the kinematic viscosity is kept constant, which is equal to  $\nu_1 = \nu_2 = 10^{-3}(\frac{m^2}{s})$ .

Figure 5.6 shows particle positions for  $t = 0$ , and  $t = 1(s)$ . Unlike the standard SPH [148], both sub figures are identical to each other, which indicates that the particle number density formulations used in the discretization of governing equations do not generate any artificial surface tension in contrast to the standard SPH.

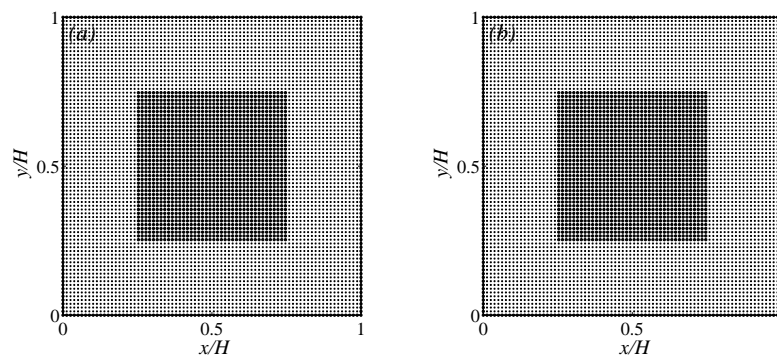


FIGURE 5.6: (a) Initial particle distribution of a square drop of fluid 2 surrounded by fluid 1 (b) the particle distribution for the same problem after 1s.

## 5.5 Kelvin-Helmholtz instability

### 5.5.1 Introduction

Flow instability at the interface between two horizontal parallel streams of different velocities and densities, with the heavier fluid at the bottom, is called the Kelvin-Helmholtz Instability (KHI). The KHI is induced by either velocity shear within a continuous fluid or a sufficiently large velocity difference across the interface of a multiphase fluid. The instability kicks in when the destabilizing effect of shear across the interface overcomes the stabilizing effect of stratification due to gravity and/or surface tension if it exists. The KHI manifests itself as a row of horizontal eddies (in the form of waves) aligned across the interface. These eddies or waves are referred to as main billows. There are several well-known natural situations where the KHI can be observed such as wind blowing over the ocean or water surface, a meteor entering the Earth's atmosphere, the interface between the tails of comets and solar wind, or the interface between a liquid layer and a compressible gas, among others.

The Kelvin-Helmholtz instability problem was solved first for the ideal case of inviscid and incompressible fluids in 1871 by Lord Kelvin. It has been studied both theoretically [83, 98, 146, 78] and experimentally [88, 89, 163, 56], as well as numerically using several techniques including lattice Boltzmann [172], direct simulation Monte Carlo [167], molecular dynamics [50], volume of fluid [87], and level set method [60], as well as, some recent works which have been conducted to investigate the feasibility and the ability of the SPH method to capture the physics behind the KHI [76, 2, 116, 12].

Junk *et al.* [76] reported an SPH simulation for the KHI problem with surface tension and viscosity included in the model, and compared their modeling results with those obtained by a grid-based method and an analytical solution in the linear regime. In the light of their modeling outcomes, they concluded that the SPH method is not capable of following the evolution of the KHI in a two-phase flow system with a large density contrast due to the smoothing property of the SPH technique.

Agertz *et al.* [2] examined the fundamental differences between SPH and grid-based methods in problems with density and thermal energy discontinuities at the interface without the inclusion of any stabilizing term (i.e., surface tension or gravity) within the modeling domain. They concluded that unlike ordinary grid-based methods, the

standard SPH formulation used in astrophysical simulations in general is unable to predict the dynamics of KHI when density differences exist between fluid layers.

In reply to the study by Agertz, Price [116] discussed the treatment of discontinuities in the SPH technique. In particular, Price discussed the difference between the integral and differential representations of fluid equations in the SPH context and then elaborated on how this difference relates to the formulation of dissipative terms to capture shocks and other discontinuities. He proposed a new formulation referred to as artificial thermal conductivity, which minimizes the dissipation away from discontinuities and showed that the results are in good agreement with those obtained by ordinary grid-based methods, reported in Agertz *et al.* [2]. More recently, Borve and Price [12] compared three different SPH formulations and illustrated that these formulations can handle hydrodynamic instabilities in compressible fluids provided that they are integrated with proper artificial dissipation terms; namely, artificial conductivity or particle regularization.

### 5.5.2 Definition of the problem

The KHI can occur at the interface between two horizontal parallel streams of different velocities and densities, with the heavier fluid at the bottom. For the simulation of this natural flow phenomenon, two immiscible fluids that are intervened between two infinite parallel horizontal plates with the height of  $H$  ( $0 < y < H$ ) (Fig. 5.7) are considered. For simplicity, the  $x$ -dimension of the computational domain  $L$  ( $0 < x < L$ ) is chosen to be equal to the domain height  $H$  ( $L = H$ ).

The computational domain for the KHI problem is represented by a set of particles created on a Cartesian grid with an equidistance particle spacing. At the beginning of the simulations, the computational domain is halved by a horizontal midline ( $H_1 = H_2 = H/2$  and  $H = 1(m)$ ), where each half represents the different fluid region. The number of particles for each fluid region is the same. An initial sinusoidal perturbation is applied to the fluid-fluid interface through swapping the color fields of particles in the vicinity of the perturbation. The wavelength of the initial disturbance is set to be equal to the domain length ( $\lambda = L$ ) so that the instability can be confined to the mid section of the model domain. The magnitude of the perturbation is ( $\zeta_o/H \approx 0.03$ ) where  $\zeta_o$  is the initial amplitude of the applied disturbance. Let  $U_1$  and  $\rho_1$  be the velocity and density of the basic state of the upper layer and  $U_2$  and  $\rho_2$  be those of the lower layer.

Particles of two fluids initially at rest are set into motion in opposite directions with the same velocity magnitude (*i.e.*  $U_1 = -U_2 = U = 0.5(\frac{m}{s})$ ).

We have implemented periodic boundary conditions at  $x = 0$  and  $x = L$ , and wall boundary conditions at  $y = 0$  and  $y = H$ . Periodic boundary conditions are enforced using ghost particles. Each solid wall is represented by a single row of wall boundary particles, and four rows of dummy particles to account for the kernel truncation by the boundaries. The no-slip boundary conditions on solid boundary walls are implemented by fixing the positions of wall boundary and dummy particles and setting their velocities to  $(U_1)$  and  $(U_2)$  correspondingly throughout the simulation. Such an implementation of wall boundary conditions is referred to as the standard fixed boundary particle approach for which further details can be found in [90].

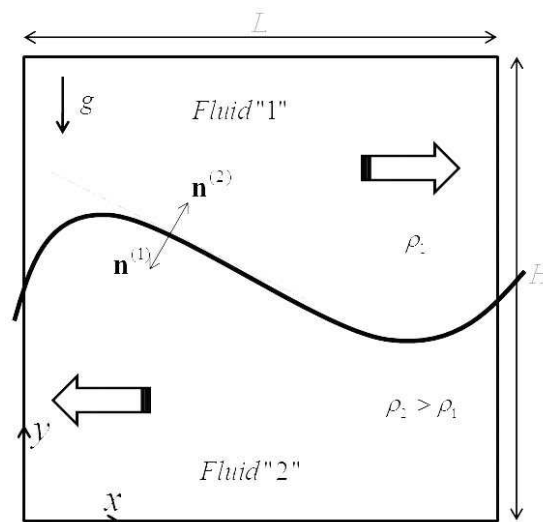


FIGURE 5.7: Configuration of Kelvin-Helmholtz instability at initial time,  $t = 0$ .

To be able to show the effect of density on the KH instability, we have conducted simulations with three density ratios, namely,  $\rho_2/\rho_1 = 2, 5$  and  $10$  where the density of the upper fluid layer is set to be  $\rho_1 = 1000(\frac{kg}{m^3})$ . When all modeling parameters are active, the surface tension force per unit length ( $\sigma$ ) acts only on the interface particles in the unit normal direction, while the gravity ( $g$ ) acts in downward direction on all particles. To show convergence, several test cases have been run where three different particle arrays  $80 \times 80$ ,  $150 \times 150$  and  $300 \times 300$  are used. It was observed that a  $150 \times 150$  array of particles is sufficient for capturing the primary wave as well as obtaining particle independent solutions.

### 5.5.3 Linear stability analysis

Here, a two-phase unperturbed flow system with uniform streams slipping past each other in opposite directions at steady state is considered. This two-fluid system can be perturbed by applying a sinusoidal disturbance on the fluid-fluid interface in the form of

$$\zeta = \zeta_o e^{i(kx - \omega t)} \quad (5.14)$$

where  $\zeta$  is the local coordinate system on the interface, which is a function of the horizontal direction  $x$ ,  $t$  is the time,  $\omega$  is the angular frequency of the wave, and  $k$  is the wave number. It can be shown that when both gravitational and surface tension forces are present, the eigenvalue condition [34] is given by

$$\frac{\omega}{k} = \frac{\rho_1 U_1 + \rho_2 U_2}{\rho_1 + \rho_2} \pm \sqrt{-\frac{\rho_1 \rho_2 (U_1 - U_2)^2}{(\rho_1 + \rho_2)^2} + \frac{g \rho_2 - \rho_1}{k \rho_1 + \rho_2} + \frac{\sigma k}{\rho_1 + \rho_2}}, \quad (5.15)$$

In the absence of stabilizing forces, namely gravity and surface tension, one can see from Eq. (5.15) that the perturbation grows unconditionally. Thus, the velocity discontinuity is always unstable. On the other hand, both solutions are neutrally stable (*i.e.* correspond to a real value of  $\omega$ ) as long as the sum of all the terms in the square root is positive. This situation results in stable waves for the system. However, perturbation will grow if the imaginary part of  $\omega$  is non-zero, that is,

$$-\frac{\rho_1 \rho_2 (U_1 - U_2)^2}{(\rho_1 + \rho_2)^2} + \frac{g \rho_2 - \rho_1}{k \rho_1 + \rho_2} + \frac{\sigma k}{\rho_1 + \rho_2} < 0. \quad (5.16)$$

With some mathematical manipulations on Eq. (5.16), one can write

$$Ri = \frac{\rho_1 + \rho_2}{k \rho_1 \rho_2 (U_1 - U_2)^2} (g(\rho_2 - \rho_1) + k^2 \sigma) < 1 \quad (5.17)$$

where  $Ri$  is the *Richardson number* which is defined as the ratio of potential energy to kinetic energy. The potential energy in the  $Ri$  number constitutes surface tension and body force effects. To be able to analyze the effect of surface tension and body force

individually on the occurrence of instability, it is more convenient to split up the  $Ri$  number into two parts as

$$Ri_\sigma = \frac{k\sigma(\rho_1 + \rho_2)}{\rho_1\rho_2(U_1 - U_2)^2} \quad (5.18)$$

$$Ri_g = \frac{g(\rho_2^2 - \rho_1^2)}{k\rho_1\rho_2(U_1 - U_2)^2}. \quad (5.19)$$

where  $Ri_\sigma$  and  $Ri_g$  are the surface tension and gravity  $Ri$  numbers, respectively.

For the case of  $Ri < 1$ , the analytical non-dimensional growth rate  $\gamma_e$  in the linear regime can be written as

$$\gamma_e = Im(\omega) = \frac{2\pi\sqrt{\rho_1\rho_2}}{\rho_1 + \rho_2} \sqrt{1 - Ri}, \quad (5.20)$$

which relates the growth rate of the interface perturbation to the  $Ri$  number.

For numerical investigation, the numerical growth rate  $\gamma_n$  is calculated in the form of

$$\gamma_n = \frac{\hat{\zeta}/\zeta_o - 1}{t^*}, \quad (5.21)$$

where  $\hat{\zeta}$  is the amplitude of the disturbance at time  $t$  and  $t^*$  is the dimensionless time

$$t^* = \frac{t|U_2 - U_1|}{H}, \quad (5.22)$$

where  $t$  is the real time and  $H$  is the domain height.

To be able to compare the analytical growth rate in Eq. (5.20) which is only valid for the linear regime with the numerical one in Eq. (5.21),  $t^*$  is calculated when the wave amplitude reaches up to 10 percentage of the domain height ( $\hat{\zeta}/H \cong 0.1$ ).

#### 5.5.4 Discussion

Having perturbed the fluid-fluid interface at the initial time ( $t^* = 0$ ) by a small disturbance in accordance with Eq. (5.14), under certain input parameters (*i.e.*, surface tension, gravity, density, *etc.*), the interface disturbance grows and the flow system becomes unstable. Figure 5.8 illustrates the growth of the interface disturbance as a function of time in the two-dimensional KHI problem for a density ratio of 2 at  $Ri = 0.01$ . For this simulation, the stabilizing force is only the surface tension (*i.e.* the  $Ri$  number is calculated from Eq. (5.18)) and the coefficient of the artificial viscosity in Eq. (3.26) is set to be  $\alpha = 0.001$ . As a result of the interface disturbance, the heavier fluid starts moving in a positive vertical direction, while the lighter fluid in the opposite direction. As a result, both fluids begin to penetrate into each other. As the time progresses, the height of the instability gets larger, and due to the inertial effect, both fluids tend to gain horizontal velocity opposite to their initial bulk velocities. At ( $t^* \cong 0.75$ ) in Fig.5.8, a small vortex appears and the flow regime is no longer linear. This process results in the formation of the main billow. It should be noted that the linear stability analysis performed in section 5.5.3 is valid only before this time step. At later times, the characteristic form of the KHI becomes much more obvious. Just after the time step ( $t^* \cong 1.25$ ), the non-linear flow regime results in the formation of a Cat's Eye vortex out of the hydrodynamical motions.

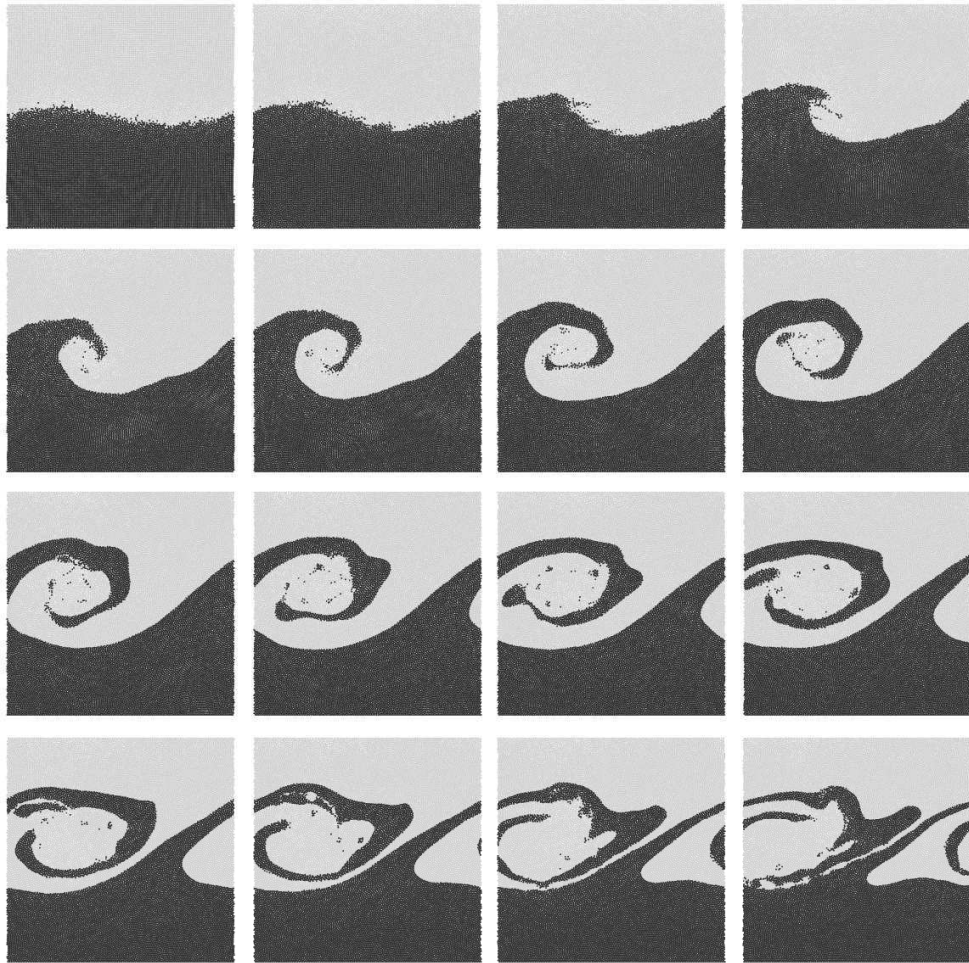


FIGURE 5.8: Time evolution of the interface in the two-dimensional KHI problem for the density ratio of ( $\rho_2/\rho_1 = 2$ ), and  $\alpha = 0.001$  at  $Ri = 0.01$ , which is given between dimensionless time  $t^* = 0.25$  and  $t^* = 4.0$  with a time interval of  $\Delta t = 0.25$ . The time step increment is from left-to-right for each row.

Figure 5.9 shows the time evolution of the growing disturbance for the density ratio  $\rho_2/\rho_1 = 2$  at various  $Ri$  numbers. Similar results are also presented for  $\rho_2/\rho_1 = 5$  and  $\rho_2/\rho_1 = 10$  in Figs. 5.10 and 5.11 respectively. In these figures, each row shows the status of the interface at various instances for a given  $Ri$  number. For these three test cases, the only stabilizing force is the surface tension and the artificial viscosity coefficient is set to be  $\alpha = 0.001$ .

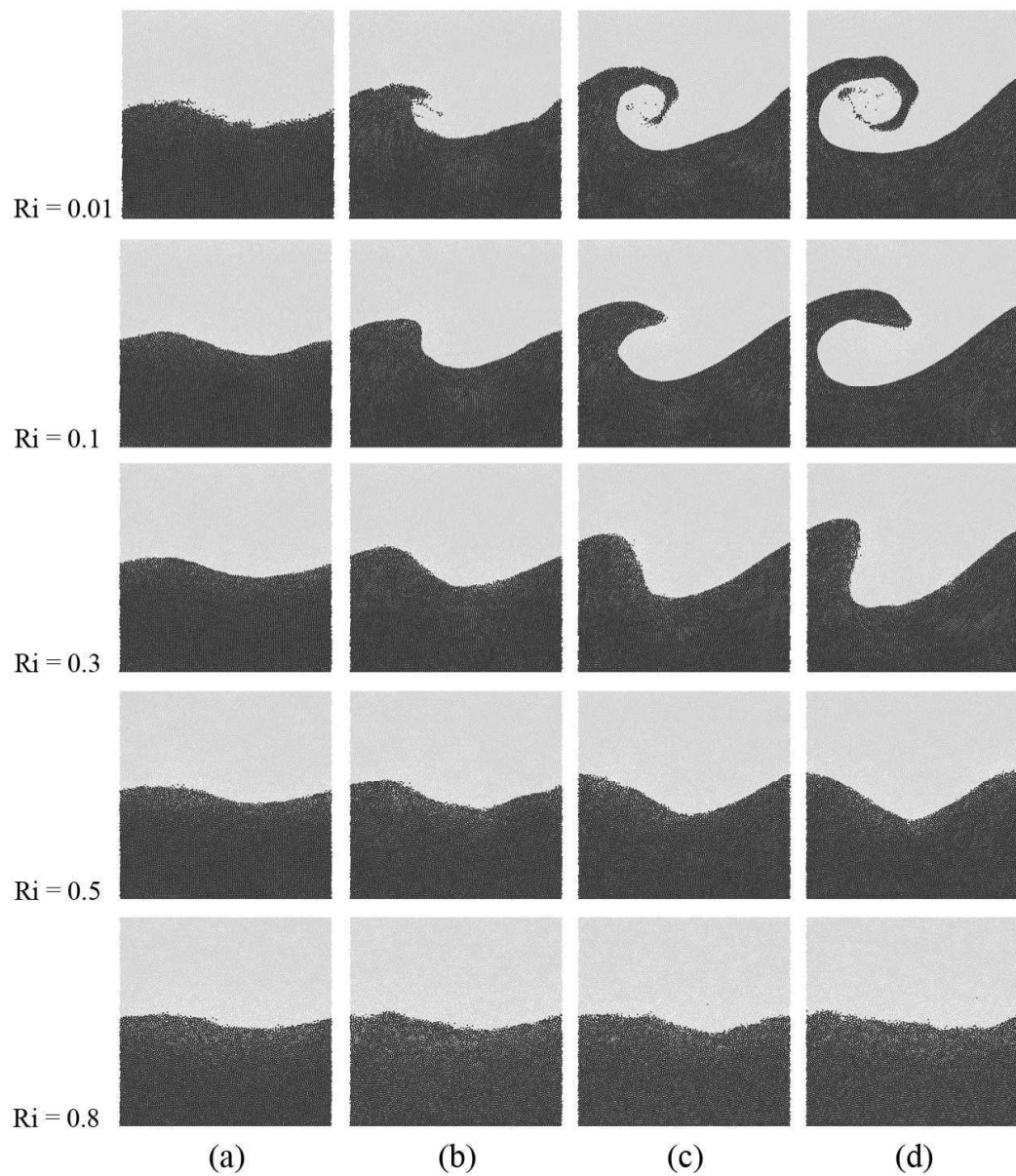


FIGURE 5.9: Time evolution of the interface in the two-dimensional KHI problem for the density ratio of  $\rho_2/\rho_1 = 2$  at various  $Ri$  numbers; (a)  $t^* = 0.5$ , (b)  $t^* = 1.0$ , (c)  $t^* = 1.5$ , (d)  $t^* = 2.0$ ; ( $\alpha = 0.001$ ).

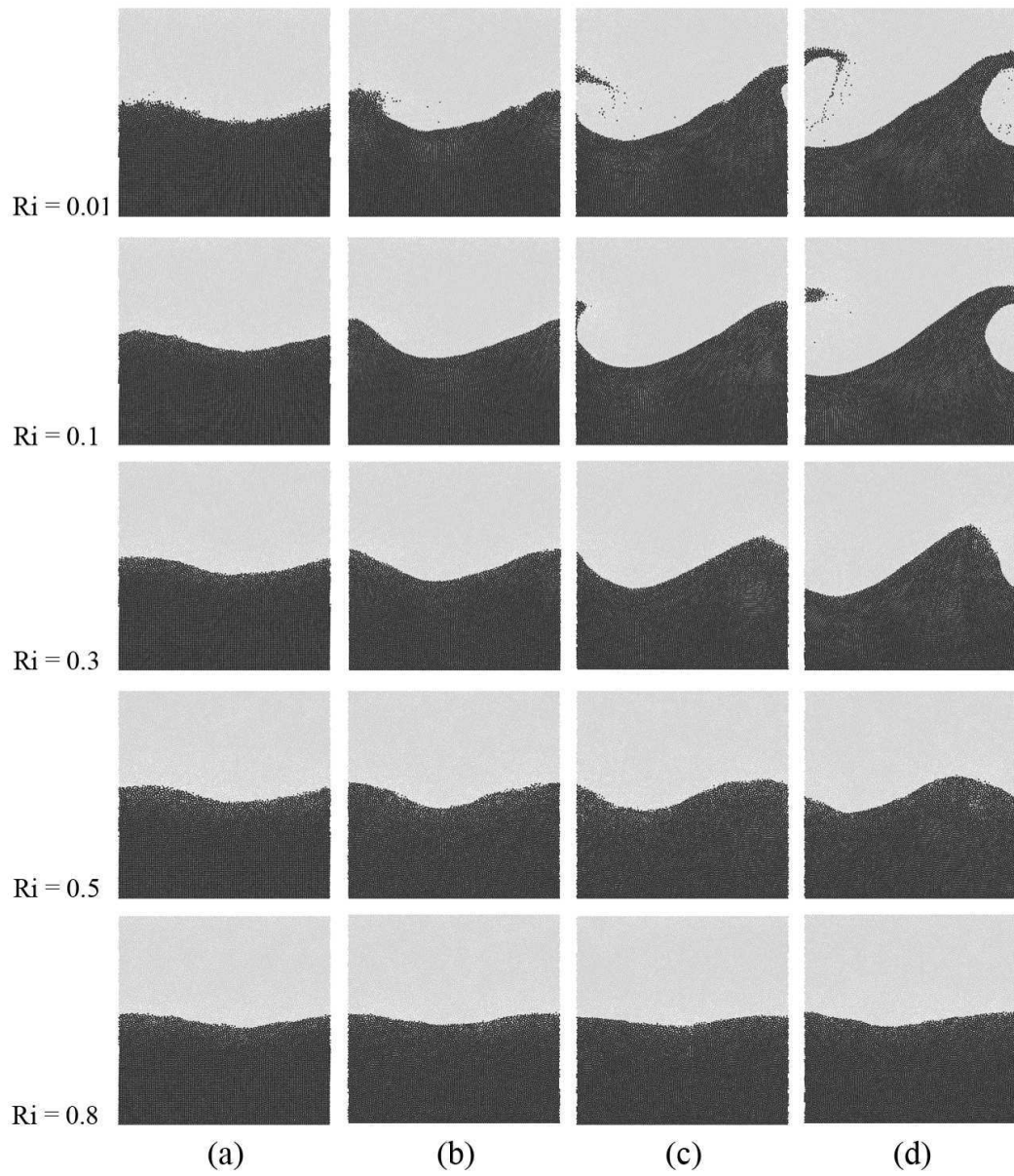


FIGURE 5.10: Time evolution of the interface in the two-dimensional KHI problem for the density ratio of  $\rho_2/\rho_1 = 5$  at various  $Ri$  numbers; (a)  $t^* = 0.5$ , (b)  $t^* = 1.0$ , (c)  $t^* = 1.5$ , (d)  $t^* = 2.0$ ; ( $\alpha = 0.001$ ).

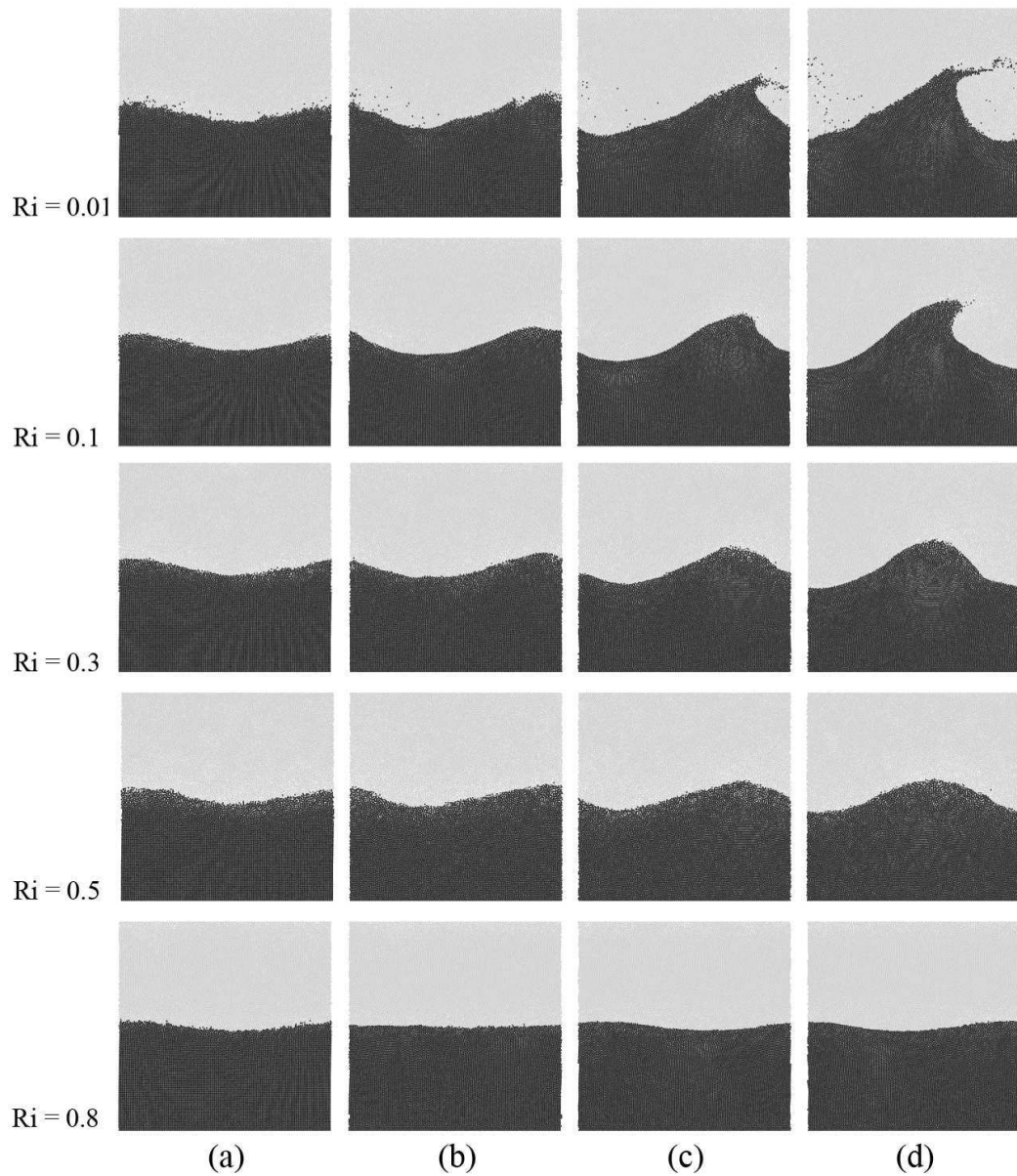


FIGURE 5.11: Time evolution of the interface in the two-dimensional KHI problem for the density ratio of  $\rho_2/\rho_1 = 10$  at various  $Ri$  numbers; (a)  $t^* = 0.5$ , (b)  $t^* = 1.0$ , (c)  $t^* = 1.5$ , (d)  $t^* = 2.0$ ; ( $\alpha = 0.001$ ).

As mentioned previously, the  $Ri$  number is the only parameter that controls the stability of the two fluid system in the KHI phenomena. Towards this end, it is important to determine the critical value for this number, which defines the border between stable and unstable flow regimes. The results of the simulations have shown that in the SPH method, the critical value for the  $Ri$  number is approximately 0.8 for all density ratios, which is slightly smaller than the one determined using the linear stability analysis. This

difference might be attributed to the artificial viscosity utilized in the SPH method, numerical diffusion and the methodology used to perturb the initial fluid-fluid interface.

The comparative examination of Figs. 5.9, 5.10 and 5.11 for a given  $Ri$  number reveals that the density ratio significantly affects the shape of the main billow as well as the growth rate. It is also important to note that with increasing density ratio, the transition from a linear to non-linear regime is delayed to later simulation times. On the other hand, as can be seen from these three figures individually that for a given density ratio, the growth rate and the transition in the flow pattern from a linear to non-linear regime is a function of the  $Ri$  number. Results presented in Figs. 5.9, 5.10 and 5.11 are summarized as the plot of growth rate versus the  $Ri$  number in Fig. 5.12 where numerically and analytically computed growth rates are compared. One can see from the figure that the numerically computed growth rate decreases with increasing  $Ri$  number and/or density ratio, which is consistent with Eq. (5.20), and simulation results are in close agreement with those corresponding to analytical solutions.

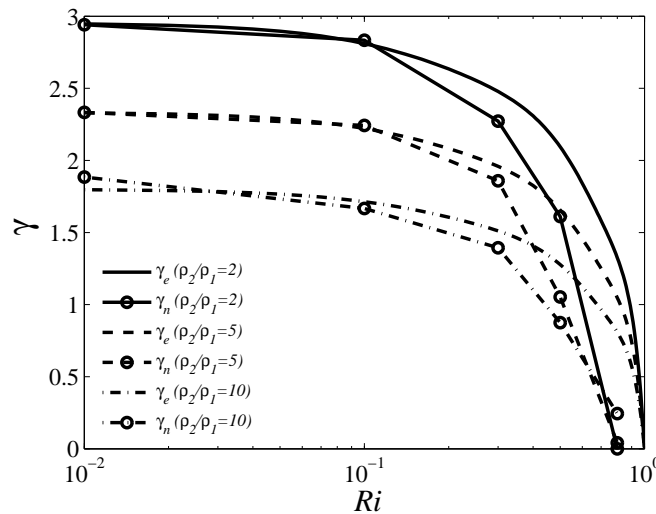


FIGURE 5.12: Growth rate ( $\gamma$ ) of the KHI in the linear regime for various  $Ri$  numbers and density ratios ( $Ri$  numbers are based on surface tension;  $\alpha = 0.001$ ).

Figure 5.13 shows the relation between the growth rate and stabilizing forces (the surface tension and body forces) at various  $Ri$  numbers calculated from Eqs.(5.18) and (5.19) respectively. For both cases, the density ratio is  $\rho_2/\rho_1 = 10$  and the artificial viscosity coefficient is set to be  $\alpha = 0.01$ . It is observed that for the same  $Ri$  number, nearly the same growth rate exists, which implies that the KHI phenomena is mainly related to the value of the  $Ri$  number, not to the nature of the stabilizing forces.

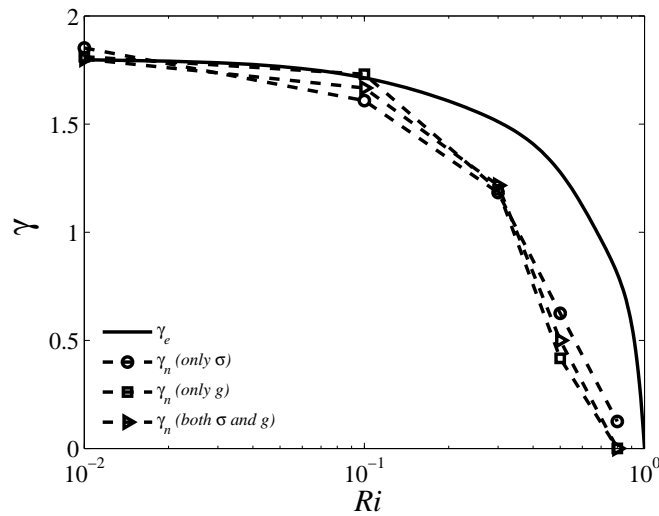


FIGURE 5.13: Effect of stabilizing forces on the growth rate ( $\gamma$ ) of the KHI in the linear regime ( $\rho_2/\rho_1 = 10$ ;  $\alpha = 0.01$ ).

It was previously stated that the artificial viscosity is one of the reasons that may cause numerically obtained simulation results to deviate slightly from analytical ones. Figure 5.14 illustrates the effect of the artificial viscosity on the time evolution of the interface in the two-dimensional KHI problem for one specific test case, which is chosen as a representative for the whole data. In this specific test case,  $Ri = 0.01$  and  $\rho_2/\rho_1 = 10$ . As seen from the figure, upon choosing a low artificial viscosity coefficient, the numerical results are in better agreement with those of the linear stability analysis. One can also notice that the growth rate decreases as the utilized artificial viscosity coefficient increases. To have stable numerical simulations, the artificial viscosity coefficient can not be chosen to be too small (as an example,  $\alpha \geq 0.0001$  and  $0.001$  for  $\rho_2/\rho_1 = 2$  and for  $\rho_2/\rho_1 = 10$ , respectively). Therefore, it should be selected carefully in order to have physically valid numerical results, which can predict the KHI phenomena accurately without losing numerical stability.

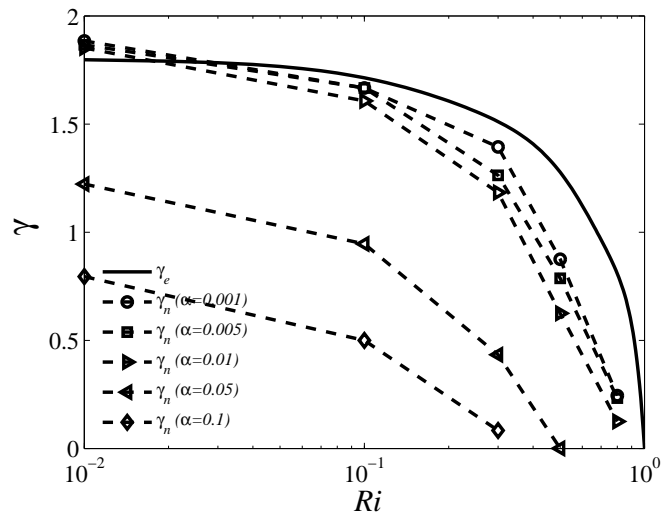


FIGURE 5.14: Effect of the artificial viscosity coefficient  $\alpha$  on the growth rate ( $\gamma$ ) of the KHI in the linear regime ( $\rho_2/\rho_1 = 10$ ).

Finally, for the sake of completeness, the time evolution of the interface for the density ratio of  $\rho_2/\rho_1 = 10$  is demonstrated in Fig. 5.15. For this simulation,  $Ri = 0.01$  (based on the surface tension calculated from Eq. (5.18) and  $\alpha = 0.01$ ). It can be concluded from Fig. 5.15 that for a large density ratio, the vortex elongates rather than rolling up. Such a behavior was attributed to the poor particle resolution in the low density region in the reference [16], where the density difference between two fluids was handled using a different particle resolution (and thus equal mass) for each fluid domain.

Although in the current work, the KHI problem was set using the same particle resolution for both fluids (thus unequal mass particles for each fluid [67]), the vortex elongation or the so called fingering is still observed. The fingering was also reported to occur in the modeling of the KHI with mesh-dependent methods [87, 60, 115] under certain modeling parameters, which might not necessarily be due to only the large density ratio. It should be noted that the flow circulation in the KHI system begins at the crest of the wave in all the test cases reported in this work. In the simulation with the density ratio of 2, both fluids have relatively close inertial forces, and therefore, the vortex is not advected significantly by fluid streams. Consequently, as the simulation progresses, the flow circulation forms the Cat's Eye shape. On the other hand, due to the fact that there exists a relatively large difference in the inertial forces between the upper and the lower fluid layers for the density ratio of 10, and the heavier fluid at the bottom of the modeling domain has a greater inertial force than the lighter fluid at the top, the flow

circulation is advected faster in the flow direction of the heavier fluid whereby it leaves the flow domain through the left side and re-enters it from the right side. Accordingly, the translational motion of the flow circulation along the interface brings about the elongation of the crest of the wave, or the fingering phenomenon.

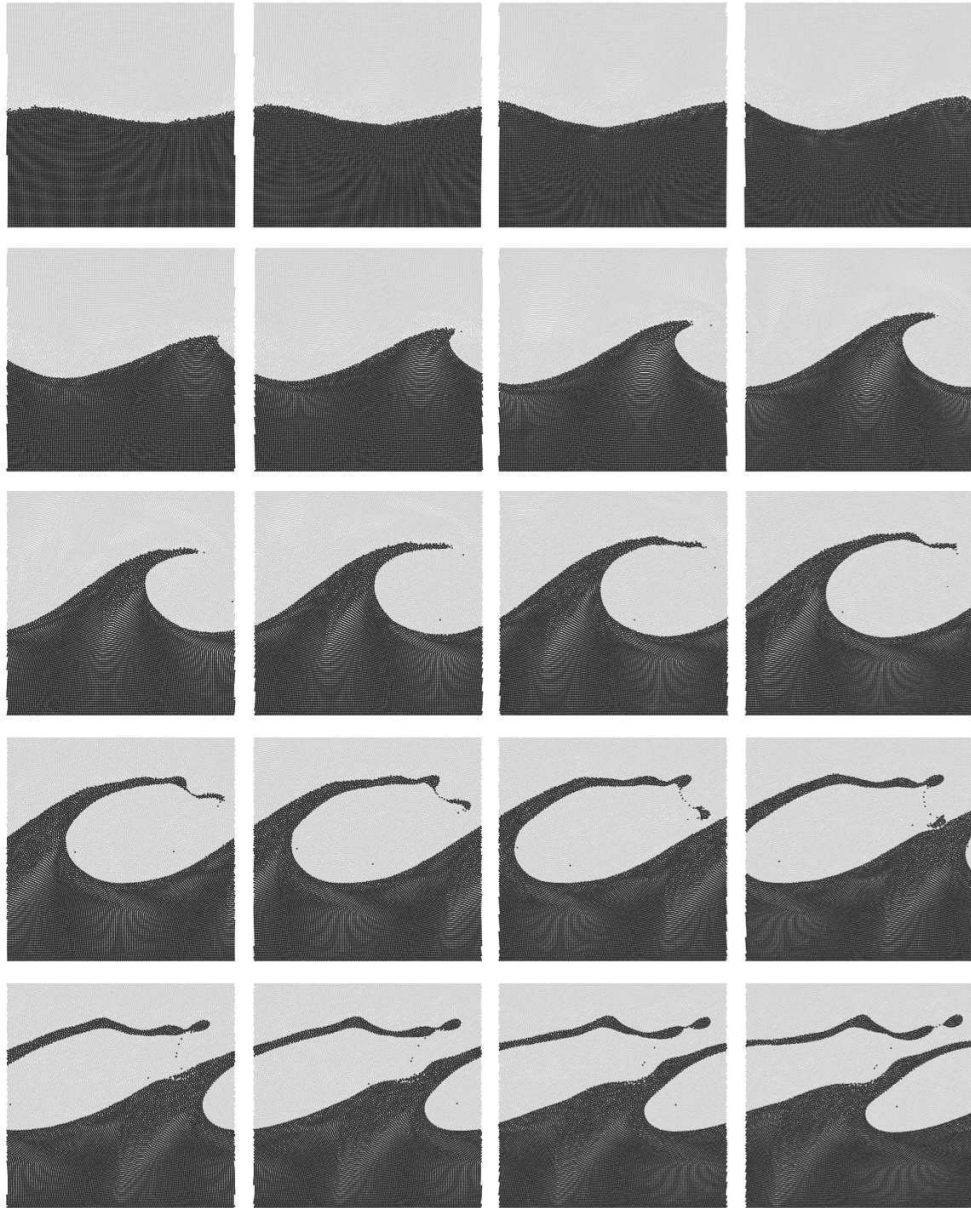


FIGURE 5.15: Time evolution of the interface in the two-dimensional KHI problem for the density ratio of  $(\rho_2/\rho_1 = 10)$ , and  $\alpha = 0.01$  at  $Ri = 0.01$ , which is given between dimensionless time  $t^* = 0.25$  and  $t^* = 6.0$  with a time interval of  $\Delta t = 0.25$ . The time step increment is from left-to-right for each row.

As briefly mentioned in the introduction section, the standard SPH formulation fails to

predict the KHI in the flow systems with large density ratios. The suppression of the instability or non-existence of mixing between two fluid layers is described as the *artificial surface tension* at the two-fluid interface [116]. The presence of the artificial surface tension at the discontinuity can be attributed to the generation of an artificial force owing to the inaccurate computation of the density gradient. Recall that in the present work, the particle number density is used in the discretization of governing equations unlike the standard SPH formulation which uses a real fluid density. Therefore, one can conclude that a fluid particle will not experience any artificial force when pressure equilibrium is assumed and the artificial viscosity and all the external forces are ignored.

### 5.5.5 Conclusions

In this section the KHI phenomenon in inviscid incompressible two-phase fluids under the effects of surface tension and body forces was studied. Numerical simulations were performed for numerous  $Ri$  numbers, density ratios and artificial viscosity coefficients. It was shown that under the influence of certain input parameters (i.e., body force, surface tension, and density ratios), flow instability develops in a two-phase fluid system with an initial disturbed fluid-fluid interface. The instability grows in time and subsequently, the flow system experiences a transition from a linear to non-linear regime. Simulation results are observed to be in good agreement with those corresponding to analytical solutions in the linear regime in terms of growth rate. Referring to the linear stability analysis, a two-phase fluid system with the  $Ri$  number less than unity ( $Ri < 1$ ) should experience instability. However, it is observed that the flow instability in the SPH method occurs at  $Ri$  number values less than roughly 0.8. The noted discrepancies between numerical and analytical results might be attributed to numerical diffusions, to the inclusion of artificial viscosity in the model and to the form of the initial interface disturbance. It was observed that the growth rate is higher for lower density ratio and  $Ri$  numbers, and reaches to free shear flow limit at  $Ri$  numbers near zero. Numerical results suggest that the growth rate of the instability is only controlled by the  $Ri$  number, and is independent of the nature of stabilizing forces. It is also shown that the artificial viscosity plays a significant role in all simulations. Therefore, it should be chosen such that it preserves the stability of the numerical method and captures all the complex physics behind this phenomenon. As a final remark, it should be noted that unlike the standard SPH formulation, the SPH discretization scheme based on the particle number

density formulation does not lead to the creation of so-called artificial surface tension force across the fluid-fluid interface that can suppress the KHI.

## 5.6 Rayleigh-Taylor instability

### 5.6.1 Introduction

Instability developing and evolving at the interface between two horizontal parallel fluids of different viscosities and densities with the heavier fluid at the top and the lighter at the bottom is known as the Rayleigh-Taylor Instability (RTI) to honor the pioneering works of Lord Rayleigh [124] and G. I. Taylor [150]. The instability initiates when a multiphase fluid system with different densities experiences gravitational force. As a result, an unstable disturbance tends to grow in the direction of gravitational field thereby releasing and reducing the potential energy of the system.

Due to being an important phenomenon in many fields of engineering and sciences, the RTI have been widely investigated by using experimental [162, 5], analytical [112, 97] as well as numerical [169, 118] approaches. In the literature, one may find many qualitative numerical study for this two phase flow problem [9, 13, 117, 133, 158, 159, 32, 108]. Surprisingly, out of the works which have been published up to now, there are only a few studies, especially for the long time evolution of the RTI, where the authors compare their numerical results with available analytical theories and if it is so, mesh dependent techniques were used [13, 108]. To our best knowledge there is no work in which the RTI problem is validated against analytical data using meshless methods.

### 5.6.2 Definition of the problem

The RTI can occur in a multiphase fluid system where a layer of heavier fluid is placed on top of another layer of lighter fluid with an interface having a small initial perturbation. This disturbance will grow to produce spikes of heavier fluid moving downward into the lighter fluid, and bubbles of the lighter fluid moving upward. For modeling the RTI phenomena, a rectangular computational domain (Fig. 5.16) with the width and height of  $H$  and  $4H$  is used. For simplicity,  $H$  is chosen to be unity ( $H = 1(m)$ ). The number of particles for each fluid region is the same. An initial sinusoidal perturbation,

$y = 2 + \xi_o \cos(kx)$ , is applied to the fluid-fluid interface through swapping the color fields of particles in the vicinity of the perturbation where  $\xi_o$  is the amplitude of the applied disturbance, which is  $\xi_o/H = 0.05$ ,  $k$  is the wave number  $k = 2/\pi\lambda$ , and  $\lambda$  is the wave length which is set to be  $\lambda = 1(m)$ .

In all simulations, the density of the heavier fluid layer is set to be  $\rho_2 = 1000(\frac{kg}{m^3})$  and kinematic viscosity for both fluids are kept constant, which is equal to  $\nu_1 = \nu_2 = 10^{-3}(\frac{m^2}{s})$ . When all modeling parameters are active, the surface tension force per unit length ( $\sigma$ ) acts only on the interface particles in the unit normal direction, while the gravity ( $g$ ) acts in downward direction on all particles. The boundaries are treated as solid walls, and the no-slip and zero pressure gradient boundary conditions are imposed using MBT method [168].

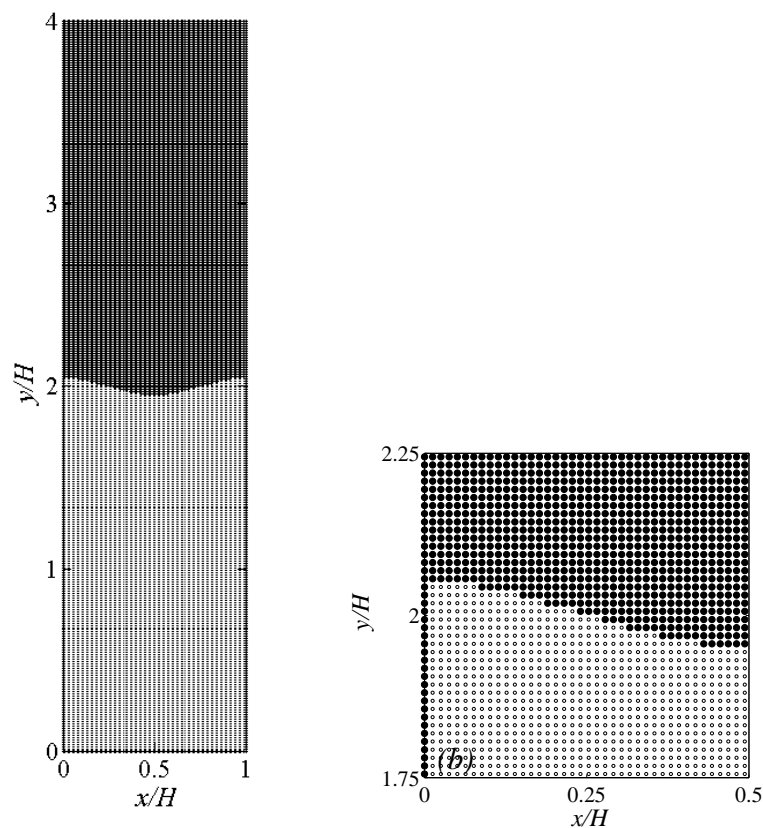


FIGURE 5.16: (a) Initial particle distribution for Rayleigh-Taylor instability (b) The zoom view of initial particle distribution for half of the interface. The particle resolution is  $80 \times 320$ .

### 5.6.3 Linear stability analysis

The linear stability analysis starts with considering a fluid system composed of two immiscible fluids possessing different densities with the configuration where the heavier fluid sits on top of the lighter one. At equilibrium, the fluid-fluid interface is located at  $y = 0$  and is assumed to be perfectly planer as illustrated in Fig. 5.17a. Therefore, fluid particles of both phases in close proximity to the interface feel the same pressure, namely,  $p_1 = p_2 = 0$ . The equilibrium state of the fluid-fluid interface can be perturbed through the application of a sinusoidal disturbance  $\zeta(x)$  whereby the interface position moves quasistatically to a new location,  $y = \zeta(x)$ . This disturbance will grow under the effect of gravitational force since the heavier fluid moves downward while dislocating the lighter fluid upwards. The growth of the initial disturbance leads to the release of potential energy. Upon employing the Newton's second law of motion, the equation governing the movement of the interface can be written

$$m\ddot{\zeta} = f^t, \quad (5.23)$$

where  $\ddot{\zeta}$  is the acceleration of the local coordinate system on the interface,  $f^t$  is the total force (sum of all forces) acting upon interface and  $m$  is the total fluid mass that moves due to the motion of the interface. The total mass is introduced as

$$m = m_1 + m_2 = \frac{(\rho_1 + \rho_2)a}{k}. \quad (5.24)$$

Here,  $a$  is the interfacial area,  $k$  is the wave number and  $m_1$  and  $m_2$ , and  $\rho_1$  and  $\rho_2$  are the masses and the densities of the lighter and heavier fluids respectively.

The total force  $f^t$  acting on the interface consists of pressure force  $f^p$ , surface tension force  $f^s$ , and viscous force  $f^\mu$ , namely,  $f^t = f^p + f^s + f^\mu$ . Given that the static pressure in an incompressible fluid linearly changes with the fluid depth, the fluid elements at  $\zeta > 0$  should feel more pressure than those at  $\zeta < 0$ . Also, knowing that the pressure is proportional to the fluid density, for the fluid region where  $\zeta > 0$ , the fluid pressure infinitesimally above the interface  $\acute{p}_2$  increases more than that below the interface  $\acute{p}_1$ . In what follows, pressure on both sides of the interface can be written as  $\acute{p}_2 = p_o + \rho_2 g \zeta$  and  $\acute{p}_1 = p_o + \rho_1 g \zeta$  as also shown in Fig. 5.17b, where  $p_o$  is the initial or equilibrium

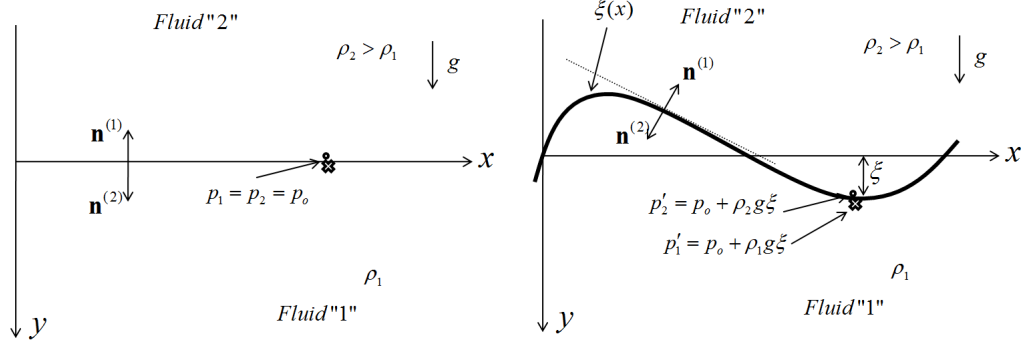


FIGURE 5.17: The schematic of two layer of fluid where the heavy fluid '2' is initially above the light fluid '1' (a) before initial disturbance, and (b) after initial disturbance.

pressure and  $g$  is the gravity. Subsequently, the pressure force across the interface can be formulated as

$$f^p = \Delta p a = (\rho_2 - \rho_1) g \zeta a. \quad (5.25)$$

where  $\Delta p = p'_2 - p'_1$ .

Furthermore, the surface tension force between two fluids is given by

$$f^s = \sigma \kappa a, \quad (5.26)$$

where  $\kappa = 1/R_o$  is the curvature of the interface with  $R_o$  being the radius of the curvature, which is defined as

$$R_o = \frac{[a + (d\zeta/dx)^2]^{3/2}}{d^2\zeta/dx^2}. \quad (5.27)$$

If it is assumed that the slope of the curve  $y = \zeta(x)$  is rather small compared with unity, one can write that  $R_o = \frac{1}{d^2\zeta/dx^2}$ .

With the initial sinusoidal disturbance and the fact that in linear regime  $k\zeta \ll 1$ , the curvature radius is simplifying to  $R_o \approx -\frac{1}{k^2\zeta}$  and the surface tension force become

$$f^s = -\sigma a k^2 \zeta. \quad (5.28)$$

Finally, the viscous force across the interface is of the following form,

$$f_k^\mu = -T_{kl}n_l a, \quad (5.29)$$

where  $T_{kl}$  is the deviatoric part of the stress tensor, and written in the component form as  $T_{kl} = \mu(v_{k,l} + v_{l,k})$ ,  $n_k$  is the  $k$ -th component of the unit normal vector  $\vec{n}$ . The vertical component of viscous force per unit area reads as

$$f_y^\mu = -(T_{yy}n_y + T_{yx}n_x)a. \quad (5.30)$$

Since in the linear regime  $|n_y| \approx 1$  and  $n_x \sim k\zeta \ll 1$ , the second term Eq. (5.30) is negligible and, hence  $f_y^\mu \approx -T_{yy}n_y a$ . The total viscous force on the interface is then

$$f^\mu = (f_y^{\mu_1} + f_y^{\mu_2})a = 2 \left( \mu_1 \frac{\partial v_1}{\partial y} - \mu_2 \frac{\partial v_2}{\partial y} \right) a. \quad (5.31)$$

where it should be noted that  $\vec{n}_1 = \vec{n}_2$ , and the subscripts 1 and 2 denote the lighter and heavier fluids respectively. Now if a perturb velocity is introduced as

$$v_1 \propto e^{ikx-ky}, \quad v_2 \propto e^{ikx+ky}. \quad (5.32)$$

Upon combining Eqs. (5.31) and (5.32), and noting that the velocity is continuous on the interface, namely,  $v_1|_{y=0} = v_2|_{y=0} = \dot{\zeta}$ , one can write the total viscous force in the form of

$$f^\mu \approx -2(\mu_1 + \mu_2)k\dot{\zeta}a. \quad (5.33)$$

Casting Eqs. (5.25), (5.28), and (5.23) into Eq. (5.23) together with some simple mathematical manipulations, the equation governing the motion of the interface can be introduced as

$$\ddot{\zeta} = A_T k g \zeta - \frac{\mu_1 + \mu_2}{\rho_2} (1 + A_T) k^2 \dot{\zeta} - \sigma k^3 \frac{1 + A_T}{2\rho_2} = 0, \quad (5.34)$$

where  $A_T = (\rho_2 - \rho_1)/(\rho_2 + \rho_1)$  is dimensionless Atwood number. If the interface disturbance is assumed to be of the form,  $\zeta \propto \exp(ikx + \gamma t)$ , the most general form for the asymptotic growth rate  $\gamma$  of the interface due to all active forces is then [97]

$$\gamma^2 - \frac{\mu_1 + \mu_2}{\rho_2}(1 + A_T)k^2\gamma - [A_Tkg - \sigma k^3 \frac{1 + A_T}{2\rho_2}] = 0. \quad (5.35)$$

It should be noted that Eq. (5.35) is not an exact, but an accurate analytical approximation (less than 11%) for the asymptotic growth rate of viscous flow in the linear regime. On neglecting the viscous effects in Eq. (5.35), one can obtain the well-known known exact analytical solution for inviscid fluid with the effect of surface tension [17]

$$\gamma^2 = kg[A_T - \frac{k^2\sigma}{g(\rho_1 + \rho_2)}]. \quad (5.36)$$

Upon setting  $\gamma^2 = 0$  in Eq. (5.36), one can calculate the maximum or critical surface tension ( $\sigma_c = \frac{(\rho_2 - \rho_1)g}{k^2}$ ) below which the given perturbation is unstable, namely,  $\sigma < \sigma_c$  where  $\sigma_c$  is the critical surface tension and shows the border of instability. In what follows, one can introduce an stability parameter as

$$\phi = \frac{\sigma}{\sigma_c}. \quad (5.37)$$

where  $\phi > 1$  means that the two-fluid system should be stable.

#### 5.6.4 Discussion

Figure 5.18 compares analytical and numerical growth rates in the linear regime which are plotted as a function of stability parameter where  $(\gamma_{x1}, \gamma_{x2})$ ,  $\gamma_e$  and  $(\gamma_n)$  denote respectively the roots of growth rate for viscous flow, growth rate for inviscid flow, and numerical growth rate which are correspondingly calculated from Eq. (5.35), Eq. (5.36) and

$$\gamma_n = \frac{\hat{\xi}/\xi_o - 1}{t^*}. \quad (5.38)$$

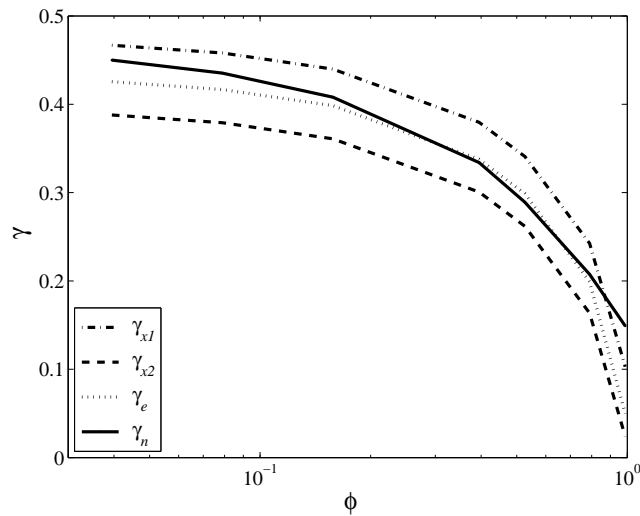


FIGURE 5.18: The dependence of the linear growth rate  $\gamma$ , of a disturbance on its stability parameter,  $\phi$ , for the Atwood number of  $A_T = 1/3$ . The dashed-dotted and dashed lines show two roots for the analytical approximation ( $\gamma_{x1}$ ,  $\gamma_{x2}$ ), the dotted line is exact theoretical result ( $\gamma_e$ ), and the solid line with the symbol inside is for numerical simulation ( $\gamma_n$ ).

Here  $t^*$  is the dimensionless simulation time at which the perturbation amplitude  $\hat{\xi}$  is approximately equal to  $\hat{\xi}/H \approx 0.1$ . There is a good agreement between analytical and numerical results except for some higher values of the stability parameter. However, all results follow the same pattern.

Figure 5.19 presents the results of numerical simulations with the density ratio of  $\rho_2/\rho_1 = 2$  which corresponds to  $A_T = 1/3$  for various stability parameters, namely,  $\phi = 0.0, 0.2, 0.6, 0.9$ , and  $1.1$ . In all cases, results are plotted for dimensionless time  $t^* = t(g/H)^{0.5} = 9.0$ . Simulation results show an exponential growth for  $\phi < 1.15$  and a stable oscillation for  $\phi > 1.15$ .

The close observation of Fig. 5.19 suggests that the morphology of the instability for the unstable regime can be divided into three visible categories. The first category is associated with small stability parameter values due to rather small surface tension. In this category, the gravitational force dominates over the surface tension force, hence causing the spike to accelerate into the lighter fluid. As a result, one can notice the formation of secondary vortices, so called Kelvin-Helmholtz instability, on the bubble-spike interface owing to the interfacial shear (see Figs. 5.19a and 5.19b). The second category is observed when the gravitational and interfacial forces are comparable. In this case, although the spike has its side tails, the shear due to the acceleration is not

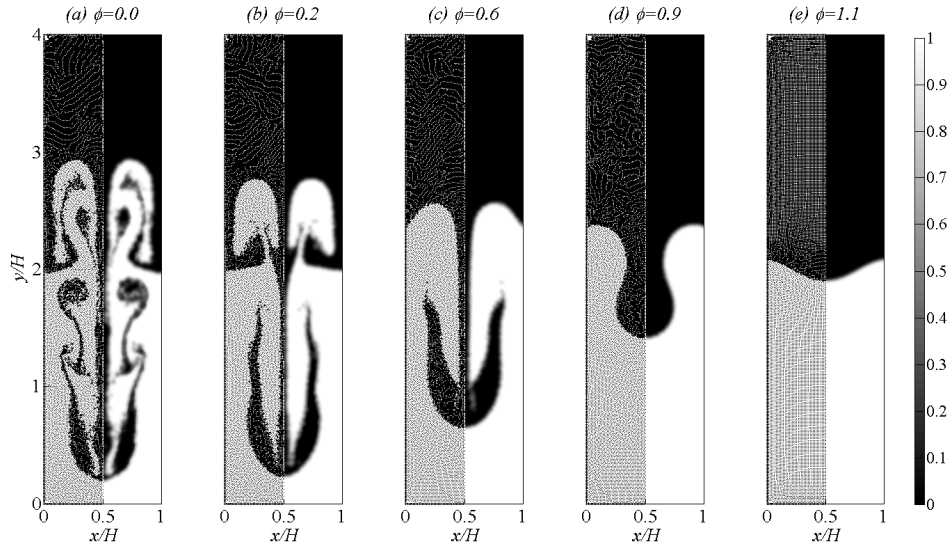


FIGURE 5.19: The stability parameter dependency of the fluid interface of the single mode perturbation Rayleigh-Taylor instability for the Atwood number of  $A_T = 1/3$  at dimensionless time of  $t^* = t(g/H)^{0.5} = 9$ . The left hand side of each sub figures presents particle distributions whereas the right hand side indicates the contour plots of the color function for the stability parameter values of (a)  $\phi = 0.0$ , (b)  $\phi = 0.2$ , (c)  $\phi = 0.6$ , (d)  $\phi = 0.9$ , and (e)  $\phi = 1.1$ .

so strong to lead to the creation of secondary instabilities (see Fig. 5.19c). In the last category corresponding to higher values of stability parameter, where the surface tension force is dominant, the instability is hindered (see Figs. 5.19d and 5.19e). It is noted that although according to Eq. (5.37), the border of instability is marked by the instability parameter of unity  $\phi = 1.0$ , here we have found this value is equal to  $\phi \approx 1.15$  which deviates by 15% from the analytical calculation. Several reasons might contribute to this discrepancy.

The first reason might be initial particle distribution. Recalling that the computational domain is initially represented by a Cartesian grid with a equidistant particle spacing, and then the sinusoidal perturbation is formed through swapping the color fields of particles in the vicinity of the planar interface, it is rather difficult to obtain highly smooth and continuous initial sinusoidal disturbance due to the discreteness in the particle distribution, as seen in Fig. 5.16b. This may result in several smaller wave-like structures on the main wave length. In the course of simulations, especially for initial times in the linear regime, these wave-like structures may act as additional disturbances which tend to grow, hence causing over prediction of the growth rate and the stability parameter. Another reason might be spurious currents due to the usage of CSF model for the surface tension. As elaborated in section 5.4.2, the spurious current brings about unphysical

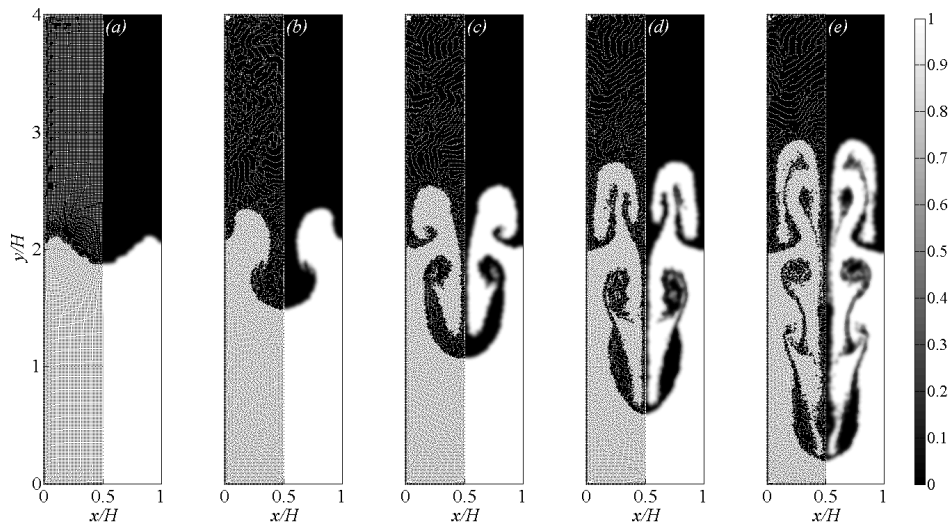


FIGURE 5.20: Time evolution of the fluid interface of the single mode perturbation Rayleigh-Taylor instability for the Atwood number of  $A_T = 1/3$  and the stability parameter of  $\phi = 0.0$ . The left panels of each sub figures show particle distributions while the right panels illustrate contour plots of the color function for dimensionless times of (a)  $t^* = 1.8$ , (b)  $t^* = 2.6$ , (c)  $t^* = 5.4$ , (d)  $t^* = 7.2$ , and (e)  $t^* = 9.0$ .

velocity field in the vicinity of the interface, which causes extra kinetic energy therein, thereby shifting the RTI problem toward unstable region. Finally, the numerical diffusion owing to the smoothing nature of the SPH method for variables such as density, viscosity, pressure, among others, especially in the neighborhood of the interface might also contribute to the deviation in the stability parameter since it consumes the stabilizing surface energy due to the surface tension.

Time evolution of the fluid interface of the single mode perturbation Rayleigh-Taylor instability for the stability parameter of  $\phi = 0.0$  and  $\phi = 0.4$  are shown in Figs. 5.20 and 5.21, respectively. Here, results are presented for five equidistant dimensionless times with  $0 \leq t^* = t(g/H)^{0.5} \leq 9.0$ .

Upon disturbing the initial planar interface sinusoidally, the hydrostatic pressure acts to drive the heavier fluid into the lighter one with the disturbance amplitude initially growing exponentially. Shortly afterward, a "mushroom cap" shape begins forming. As the time progresses, the heavy fluid falling down gradually forms a central spike with two side tails which shed side spikes from their ends for the lower stability parameter case. Eventually, for the first case where  $\phi = 0.0$ , the main spike of the heavy fluid experiences the Kelvin-Helmholtz instability while two side spikes are stretched and folded into very complicated shapes. On the other hand for the second case ( $\phi = 0.4$ ), the interface along

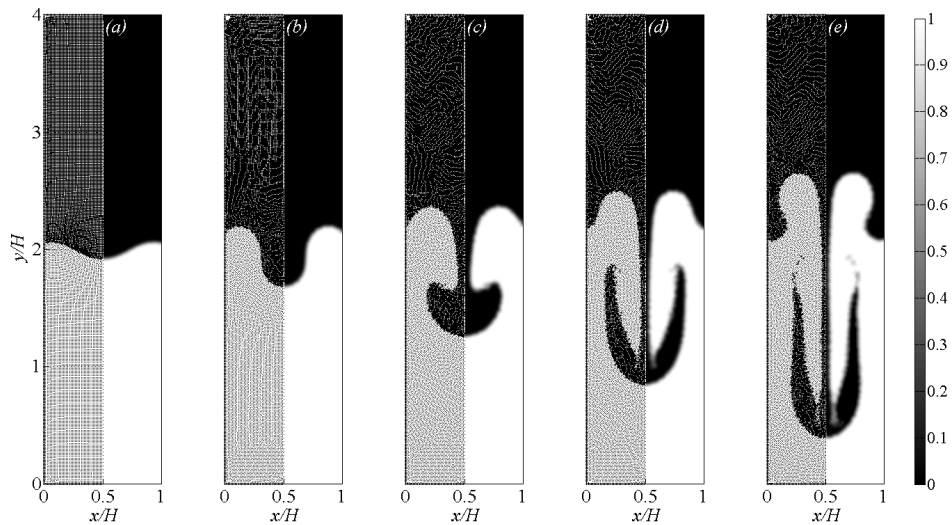


FIGURE 5.21: Time evolution of the fluid interface of the single mode perturbation Rayleigh-Taylor instability for the Atwood number of  $A_T = 1/3$  and the instability parameter of  $\phi = 0.4$ . On the left panels are given particle distributions while on the right panels are presented contours of the color function for dimensionless times of (a)  $t^* = 1.8$ , (b)  $t^* = 2.6$ , (c)  $t^* = 5.4$ , (d)  $t^* = 7.2$ , and (e)  $t^* = 9.0$ .

the central spike, as well as the fronts of both bubble and the spike remain relatively smooth.

The features of Rayleigh-Taylor instability during the time evolution can be better illustrated via the velocity fields. For this reason the velocity vectors and magnitudes for the same set of data are presented in Figs. 5.22 and 5.23. As expected, the heavier fluid falls down in the middle and the lighter fluid rises along vertical walls. A distorted single vortex is clearly visible at the initial time for both cases. For the lower stability parameter case (see Fig. 5.22) a strong shear layer exists, which provides a good condition for the formation of secondary instabilities. In this situation, with an increase in time, more and more vortices are generated and the flow field becomes quite distorted along both side of the domain. However, an increase in the stability parameter (or an increase in the surface tension) significantly suppresses the development of both Kelvin-Helmholtz instability and the tails roll-up and the interface along the instability remains rather smooth (see Fig. 5.23). In this case, up to late time, the dilute single vortex still exists and elongates along the domain height. The interfacial patterns obtained in this work compare very well with those in [158, 54].

In Figs. 5.24 and 5.25, the positions and velocities of the bubble's fronts and spike's tips,  $h_b$ ,  $v_b$  and  $h_s$ , and  $v_s$  respectively, are plotted as a function of time for the test

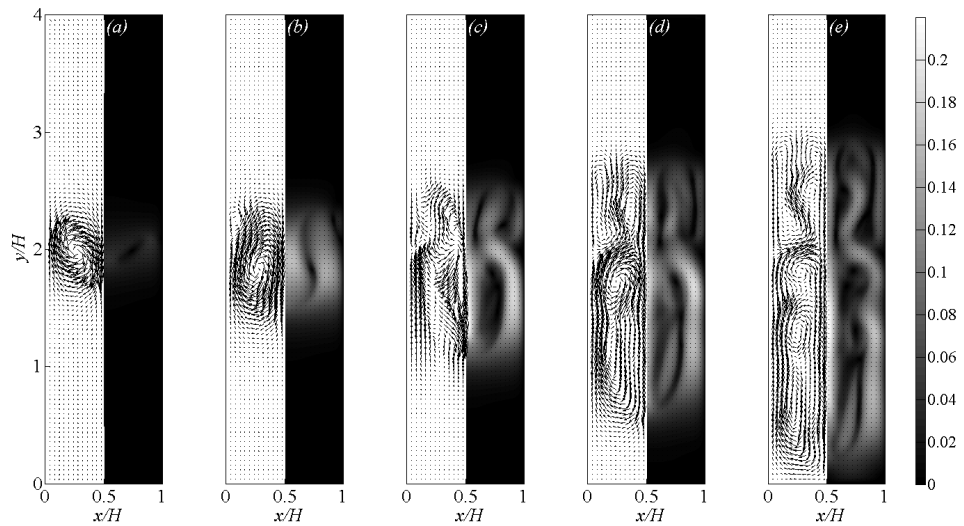


FIGURE 5.22: Time evolution of velocity fields of the Rayleigh-Taylor instability for the Atwood number of  $A_T = 1/3$  and the stability parameter of  $\phi = 0.0$ . The left hand sides of sub figures denote velocity vectors while the right hand sides show velocity contours ( $m/s$ ) (the interval between contours is 0.02) for the dimensionless time of (a)  $t^* = 1.8$ , (b)  $t^* = 2.6$ , (c)  $t^* = 5.4$ , (d)  $t^* = 7.2$ , and (e)  $t^* = 9.0$

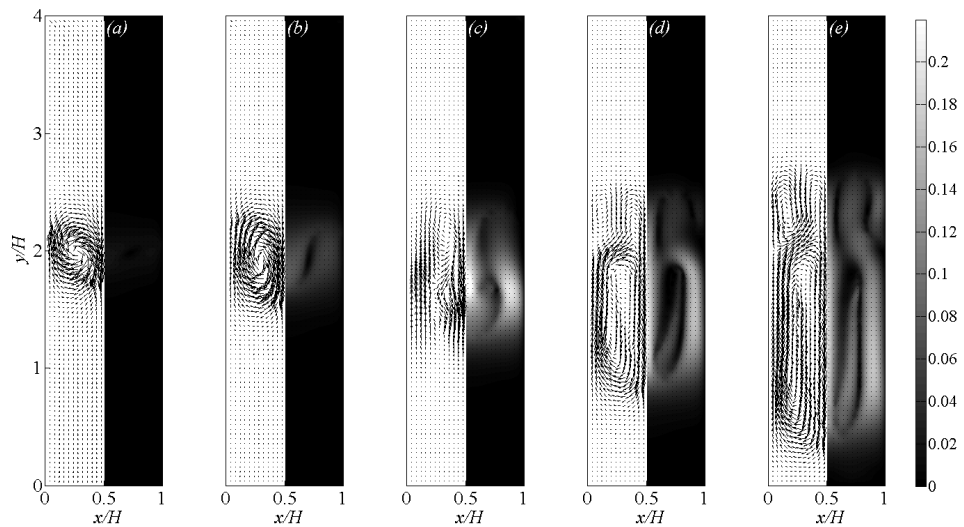


FIGURE 5.23: Time evolution of velocity fields of the Rayleigh-Taylor instability for the Atwood number of  $A_T = 1/3$  and the stability parameter of  $\phi = 0.4$ . The left hand sides of sub figures denote velocity vectors while the right hand sides show velocity contours ( $m/s$ ) (the interval between contours is 0.02) for the dimensionless time of (a)  $t^* = 1.8$ , (b)  $t^* = 2.6$ , (c)  $t^* = 5.4$ , (d)  $t^* = 7.2$ , and (e)  $t^* = 9.0$

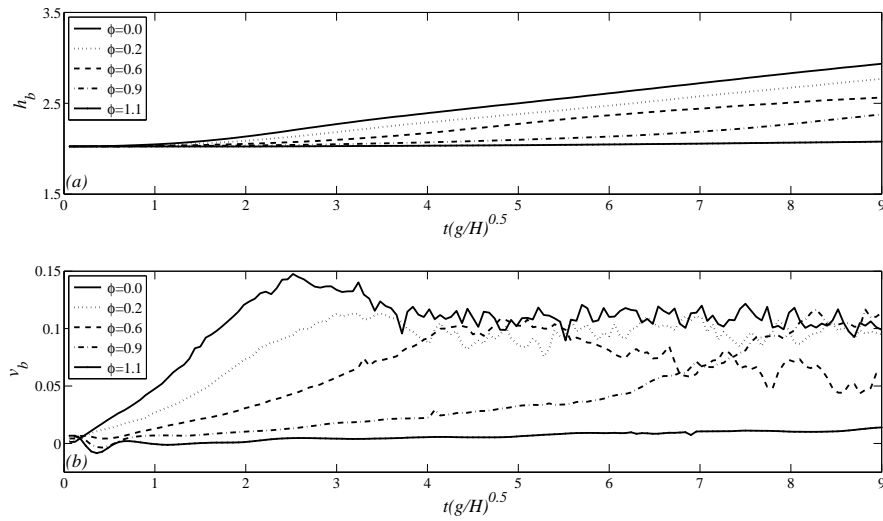


FIGURE 5.24: (a) The y-coordinate positions and (b) the velocities of the tip of the rising fluid (bubble) versus dimensionless time at the Atwood number of  $A_T = 1/3$  for various stability parameters, namely,  $\phi = 0.0, 0.2, 0.6, 0.9,$  and  $1.1$ .

case presented in Fig. 5.19. As expected, the lower the stability parameter, the higher the bubble front (Fig. 5.24a) and the faster the bubble velocity (Fig. 5.24b). The bubble velocity is one of the important characteristic behaviors of RT instability which attracted the attention of researchers [119, 52, 1]. The single bubble is found to rise with the steady velocity of [134]

$$v_b = Fr \sqrt{\frac{\rho_2 - \rho_1}{\rho_2} \frac{g D_b}{2}}, \quad (5.39)$$

where  $Fr$  is the Froude number (a dimensionless number which is defined as the ratio of inertial to gravitational forces and is used to quantify resistance of an object moving through a fluid), and  $D_b$  is the bubble diameter. If  $D_b$  is taken to be approximately equal to  $\lambda$  and with some simple mathematical manipulation, the following relationship for  $Fr$  can be obtained:

$$Fr = \frac{v_b}{\sqrt{\frac{A_T}{1+A_T} g \lambda}}. \quad (5.40)$$

It is noted that Eqs. (5.39) and (5.40) does not take into account the dilution of bubbles due to the entrainment of heavier fluid and any physical and numerical diffusions.

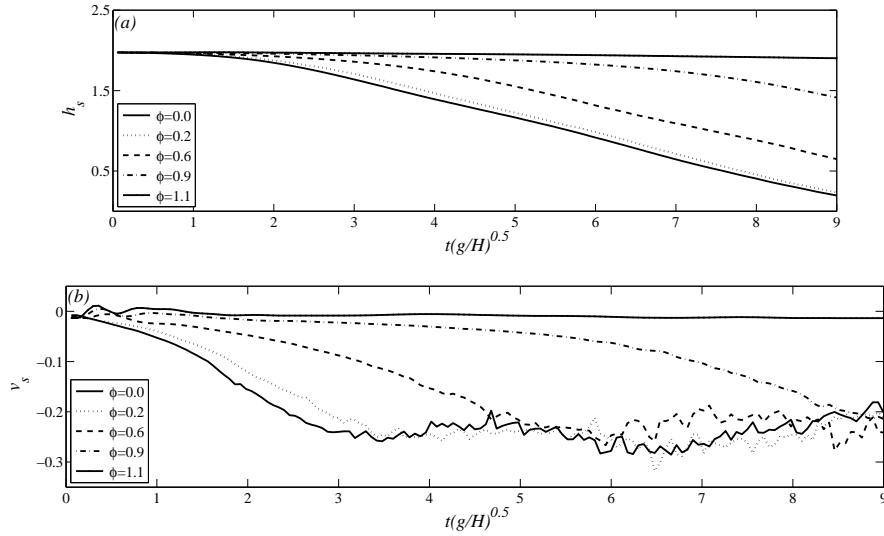


FIGURE 5.25: (a) The y-coordinate positions and (b) the velocities of the tip of the falling fluid (spike) versus dimensionless time at the Atwood number of  $A_T = 1/3$  for various stability parameters, namely,  $\phi = 0.0, 0.2, 0.6, 0.9,$  and  $1.1$ .

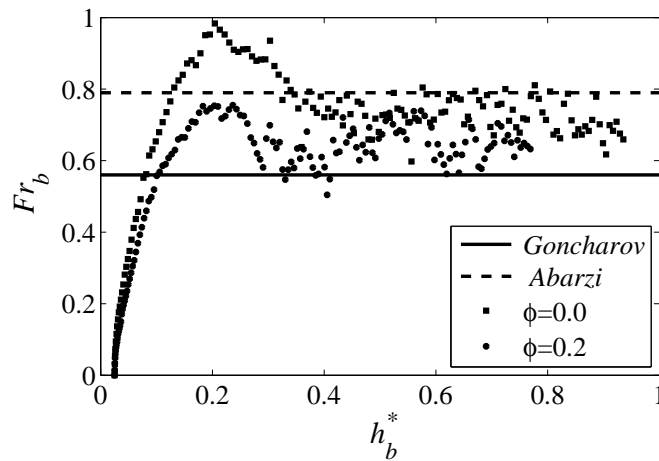


FIGURE 5.26: The Froude number of the rising fluid (bubble) versus dimensionless bubble tip position at the Atwood number of  $A_T = 1/3$ . The solid and the dashed lines are the analytical solutions proposed by Goncharov [52] and Abarzi [1] respectively, and the square and circle points represent the simulation results for the values corresponding to stability parameters  $\phi = 0.0,$  and  $\phi = 0.2$  respectively. The dimensionless bubble tip position is calculated as  $h_b^* = h_b/\lambda$ .

Calculating the magnitude of bubble velocity from numerical results, one can obtain the  $Fr$  number for the bubble motion as presented in Fig. 5.26. Evidentially, it is shown that two well known analytical solutions proposed by Goncharov [52] and Abarzi [1] form the lower and the upper bounds for the simulation results. Additionally, the presented velocity and  $Fr$  number patterns are consistent with those reported in literature [120, 165].

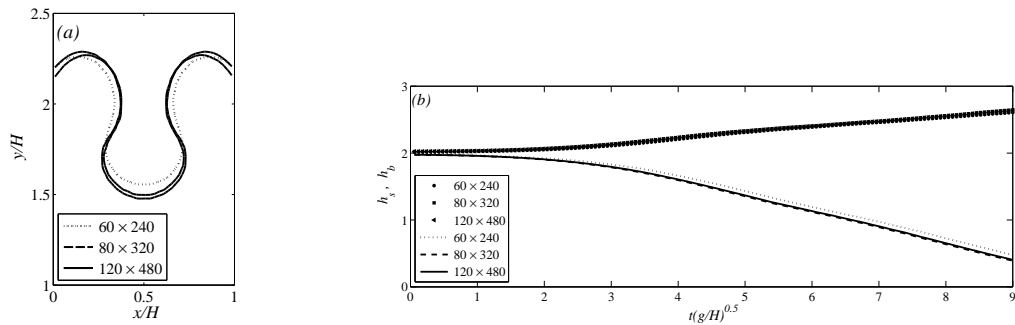


FIGURE 5.27: Particle convergence for a test case with the Atwood number of  $A_T = 1/3$  and the instability parameter of  $\phi = 0.4$  on three different sets of particles (i.e.,  $60 \times 240$  (coarse),  $80 \times 320$  (intermediate), and  $120 \times 480$  (fine)); (a) the interface position at dimensionless time of  $t^* = 4.5$ , and (b) the  $y$ -coordinates of the tip of the falling (spike) and rising (bubble) fluid versus dimensionless time

For the sake of completeness, the sensitivity of the numerical solutions to particle numbers has been investigated through solving a test case with the Atwood number of  $A_T = 1/3$  and the stability parameter of  $\phi = 0.4$  on three different sets of particles (i.e.,  $60 \times 240$  (coarse),  $80 \times 320$  (intermediate), and  $120 \times 480$  (fine)). Results of these simulations are summarized as; the interface position at dimensionless time of  $t^* = 4.5$  in Fig. 5.27a, and the  $y$ -coordinates of the tip of the falling (spike) and rising (bubble) fluid as function of dimensionless time in Fig. 5.27b.

Figure 5.27a demonstrates evidently that the intermediate particle number provides solutions with sufficient accuracy considering the trade-off between computational costs and capturing the features being studied. Additionally, Fig. 5.27b indicates that the bubble position is well reproduced by using coarse particle number, but the spike appears to need at least the intermediate particle resolution in order to achieve convergence. Therefore, in this work, all RTI results are obtained using intermediate particle resolution.

Like many other works on the numerical simulation of RTI in literature, the previously presented results have been obtained utilizing initially uniform Cartesian particle distribution (referred to as cubic grid hereafter). For the sake of completeness, to be able assess possible difficulties caused by irregular distributions of particles, numerical experiments with initially non-uniform particles have also been conducted; namely, staggered Cartesian grid and two different forms of circular grid (radially centered, and radially off-centered) with nearly equal particle spacing as illustrated in Figs. 5.28b, 5.28c, and 5.28d, respectively. Particles for circular grids are generated following the procedure

described. Initially, particle spacing is determined in accordance with the dimensions of domain boundaries and the number of particles in the  $x$ - and  $y$ -direction of the Cartesian grid. Then, the largest boundary length is chosen as a radius for the greatest circle. This radius is divided into particles with the same particle spacing as the boundary particles. Accordingly, the position of each particle on the radius of the largest circle (*i.e.*,  $4H$  for the current computational domain configuration) is used as the radius for other smaller circles. The number of particles to be generated on each circle is determined in a way that the particle spacing is equal. Once particles are generated in circular manner on all circles, the rectangular computational domain is extracted from the domain represented by particles with circular arrangement. Simulation parameters for numerical experiments conducted on these irregular particle distributions are identical to one presented in Fig. 5.20c. The number of particles for cubic grid, staggered grid, radially centered and off-centered grids is 25600, 25600, 25974, and 25989, respectively. It is noted that the non-uniform particle distribution makes it impossible to construct a symmetric disturbance with respect to vertical central line. Due to the discreteness of the particles, the initial amplitudes of the disturbances for circular grids are slightly different from cubic and staggered grids, and circular grids have larger  $y$ -coordinate positions for the tip of the spike than cubic and staggered grids with respect to bottom horizontal wall of the domain. As can be seen from Figs. 5.28e - 5.28h, these issues leads to the development of asymmetry in the spike of the instability, and inconsistencies among simulation results in terms the position of the tip of the spike as well as the straightness of the stem of the spike since the initial cosine shape disturbance is no longer a perfect cosine function and also there are also several wavelike disturbances on the main wave which change the form of the initial disturbance. To conclude, even though as the simulation progress, all fluid particles acquire random distribution, it appears that the initial particle distribution is quite important to be able construct a symmetric and a smoothly varying disturbance.

### 5.6.5 Conclusions

The developed SPH scheme have been used for the simulation of incompressible multiphase flow where the interfacial dynamics are modeled by CSF model. Numerical simulations reveal most features of Rayleigh-Taylor instability observed in previous theoretical and numerical studies. For the single-mode Rayleigh-Taylor instability, both

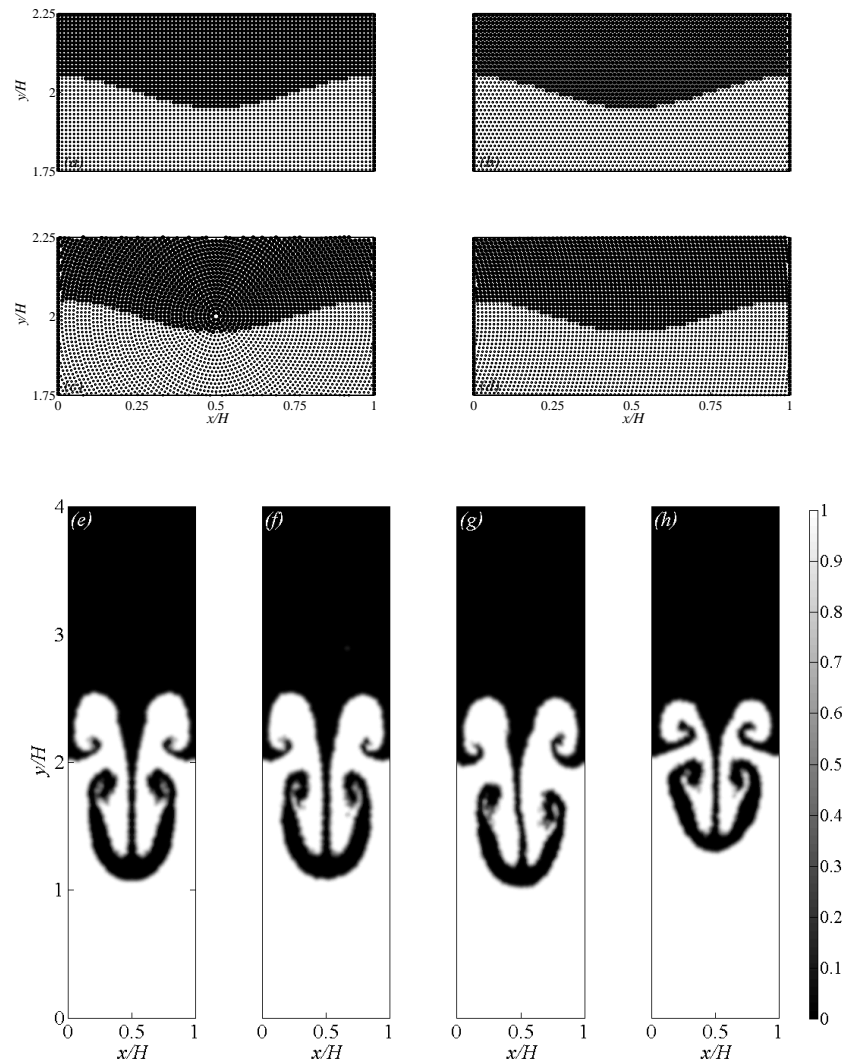


FIGURE 5.28: The different initial particle distributions namely, (a) cubic, (b) staggered, (c) radially-centered, and (d) radially-off-centered, and in sub figures (e), (f), (g) and (e) are given the evolutions of the fluid interface of the single mode RTI for the Atwood number of  $A_T = 1/3$  at dimensionless time of  $t^* = t(g/H)^{0.5} = 5.4$  calculated correspondingly on the grids in sub figures (a), (b), (c) and (d). It is noted that sub figure (e) has the lowest initial disturbance amplitude (0.044) and highest tip position with respect to the bottom wall of the domain which might explain the lag in the presented position of the tip of the spike.

the initial linear growth rate and the terminal bubble velocity as well as its Froude number agree well quantitatively with the theoretical prediction and previous numerical simulations. Furthermore, for the stability parameter analysis, some deviations from analytical results were noted, which were discussed and reasoned in details.

## Chapter 6

# ElectroHydrodynamics

### 6.1 Introduction

The motion of droplet within a bulk fluid medium takes place in numerous natural and engineering processes such as blood-flow, air entrainment at ocean surfaces, cloud cavitation, boiling heat transfer, petroleum refining, spraying of liquid fuel and paint, and bubble reactors in the chemical industry [36, 164, 166]. This motion in a viscous liquid is a dynamically complicated, nonlinear, and non-stationary hydrodynamical process, and is usually associated with a significant deformation in the droplet geometry due to the complex interactions among fluid convection, viscosity, gravitational and interfacial forces. Deforming droplet can acquire complex shapes, thereby resulting in a large variety of flow patterns around droplets [36, 157, 81, 70].

In multiphase systems of different electrical permittivities and conductivities, the utilization of electric fields provides a promising way to control the motion and deformation of droplets which can be crucial for a variety of engineering applications such as electrospray ionization, electro-coalescence and mixing, electrostatic printing and electrospinning [164, 166, 69]. To state more explicitly, if a droplet suspended in a quiescent viscous liquid is exposed to an externally applied electric field, in addition to the gravitational force induced deformation and motion if exist, it will also be deformed depending on the strength of the applied electric field and the fluid properties such as viscosity, surface tension, electrical conductivity, and permittivity [69, 155, 55].

Although a number of experimental, theoretical, and numerical studies have addressed the buoyancy-driven motion of a droplet through a quiescent fluid [70, 15, 130, 42], there are only a few works that consider the effect of the applied electric field on the dynamics of bubble deformation [81, 69, 155], and a complete understanding of the underlying mechanisms has not yet been achieved, which necessitates further studies in this field. Additionally, not only the problem in question but also the large majority of other multiphase flow problems have generally been modeled using mesh dependent techniques [81, 70, 155, 41] and the validity and accuracy of mesh free methods for modeling droplet deformation under the influence of electric field need to be further investigated.

## 6.2 Mathematical Formulation

### 6.2.1 Mechanical balance laws of continua

All constituents of the multiphase system are considered to be viscous, Newtonian and incompressible liquids with constant material properties  $D\Gamma/Dt = 0$  where  $D/Dt$  is the material time derivative operator, and the arbitrary field  $\Gamma$  may represent the density, and viscosity, among others. The set of equations governing the electrohydrodynamics of viscous fluids is composed of Maxwell's equations, and the conservation of mass and linear momentum which are written in their local form for the volume and the discontinuity surface, respectively as

$$\frac{D\rho}{Dt} = -\rho\nabla \cdot \vec{v}, \quad (6.1)$$

$$\rho \frac{D\vec{v}}{Dt} = \nabla \cdot \mathbf{T} + \rho \vec{f}^b + \vec{f}^v + \vec{f}^E, \quad (6.2)$$

$$\|\rho(\vec{v} - \vec{u})\| \cdot \vec{n} = 0, \quad (6.3)$$

$$\|\rho\vec{v}(\vec{v} - \vec{u}) - \mathbf{T} - \mathbf{T}^E\| \cdot \vec{n} = \vec{f}^s, \quad (6.4)$$

where Eq. (6.1) and (6.2) are valid in  $V - \xi$  which denotes the volume excluding points lying on the discontinuity surface  $\xi$  while Eqs. (6.3) and (6.4) are valid only on the discontinuity surface and represent the jump condition across  $\xi$ . Here,  $\rho$  is the density,  $\vec{v}$  the divergence-free velocity vector,  $\mathbf{T}$  is the symmetric total stress tensor,  $\vec{f}^b$  is the body force, and  $\vec{f}^E$  is the Lorentz force per unit volume, which can be shown to be equal to the divergence of the so-called Maxwell stress tensor  $\mathbf{T}^E$  as  $\vec{f}^E = \nabla \cdot \mathbf{T}^E$  [37]. As can be noted, the electrostatics and hydrodynamics are coupled together through the Maxwell stress tensor. Furthermore, the symbol  $\| \|$  indicates the jump of the enclosed quantities across the discontinuity surface  $\xi$ ; for instance,  $\|\Gamma\| = \Gamma^+ - \Gamma^-$  where  $\Gamma^+$  and  $\Gamma^-$  are the values of  $\Gamma$  on the positive and negative sides of the discontinuity surface,  $\vec{u}$  is the velocity of the discontinuity surface, and  $\vec{n}$  is the unit normal to the discontinuity surface, and finally,  $\vec{f}^s$  is the surface force per unit area on the interface due to the surface tension. For a Newtonian fluid, the total stress tensor can be defined as  $\mathbf{T} = -p\mathbf{I} + \tau$  where  $p$  is the absolute pressure,  $\mathbf{I}$  is the identity tensor, and  $\tau = \mu(\nabla\vec{v} + (\nabla\vec{v})^T)$  is the viscous part of the total stress tensor, where  $\mu$  is the dynamic viscosity, and  $T$  denotes transpose operation.

### 6.2.2 Electrohydrodynamics Balance Laws

Electrohydrodynamics (EHD) is a science concerned with the interactions of electric fields and electric charges in fluids. The electrical conductivity of fluids may range from exceedingly low value to high value hence allowing for a fluid to be classified as extremely good insulator (dielectrics) or highly conducting. In electrohydrodynamics transport phenomena, due to the transient nature of the problems, the electric current distribution is not steady. Therefore, in accordance with the Ampere-Maxwell's law,

$$\nabla \times \vec{B} = \mu_M \vec{J} + \mu_M \epsilon^E \frac{\partial \vec{E}}{\partial t}, \quad (6.5)$$

dynamic currents in the system give rise to a time-varying induced magnetic field. Here,  $\vec{B}$  and  $\vec{E}$  respectively are magnetic and electric field vectors,  $\mu_M$  is the magnetic permeability, and  $\vec{J}$  is total volume current. In electrohydrodynamics, the dynamic currents

are so small that the influence of magnetic induction is negligible whereby the electromagnetic part of the system can be described by a *quasi-static electric field model*. Additionally, in the system considered, there is no externally applied time-varying magnetic field. In light of these assumptions, the coupling between the electric and magnetic field quantities in the Faraday's law  $\nabla \times \vec{E} = -\partial\vec{B}/\partial t$  disappears which requires that the electric field vector be irrotational as [132]

$$\nabla \times \vec{E} = 0, \quad (6.6)$$

which necessitates that the gradient of the electric field vector be a symmetric tensor, namely,  $\nabla\vec{E} = (\nabla\vec{E})^T$ . The total volume current is defined as

$$\vec{J} = q^v \vec{v} + \vec{j}, \quad (6.7)$$

where the first term on the right hand side is the convection current due to the free charges,  $q^v$  is the volume-charge density of free charges, and  $\vec{j}$  is the volume conduction current density, ohmic current, which is related to electric field vector through

$$\vec{j} = \sigma^E \vec{E}, \quad (6.8)$$

where  $\sigma^E$  is the electrical conductivity.

The Gauss' law for electricity in a dielectric material with the absolute permittivity (hereafter referred to as the permittivity)  $\varepsilon^E$  can be written in terms of the electric displacement vector,  $\vec{D} = \varepsilon^E \vec{E}$  as

$$\nabla \cdot \vec{D} = q^v. \quad (6.9)$$

On taking the divergence of the differential form of Ampere's law, and using the entity  $\nabla \cdot \nabla \times \vec{B} = 0$  (the divergence of the curl is equal to zero) together with the Gauss' law (Eq. (6.9)) for electricity, one can write the charge conservation as

$$\frac{Dq^v}{Dt} + \nabla \cdot \vec{j} = 0. \quad (6.10)$$

Considering a homogeneous fluid with the constant permittivity and the electrical conductivity, and then substituting the Gauss' law for electricity in a dielectric material (Eq. (6.9)) together with the volume conduction current density (Eq. (6.8)) into the charge conservation equation (Eq. (6.10)), one can write

$$\dot{q}^v = -q^v \frac{\sigma^E}{\varepsilon^E}. \quad (6.11)$$

The integration of this differential equation produces

$$q^v = q_o^v \exp\left(\frac{-t}{t^E}\right), \quad (6.12)$$

which describes the time relaxation of the net free charges along fluid particles line. Hence, homogeneous fluids support no net free charges. However, in inhomogeneous materials, free charges can be generated by an electric field component along the gradients of electrical conductivity and/or permittivity. Here,  $t^E = \varepsilon^E/\sigma^E$  is referred to as the bulk relaxation time. For electrohydrodynamics problems, the time  $t$  can be considered as the viscous time scale of the fluid motion, which is defined as  $t^\mu = \rho L^2/\mu$ , where  $L$  is the characteristic length scale. A two-fluid system can be classified as dielectric-dielectric, dielectric-conducting, or conducting-conducting by comparing the magnitude of  $t^E$  with  $t^\mu$  where the last case is the focus of this work.

As in the case of mechanical balance laws, in the surface-coupled model for a sharp interface, the electrical material properties are also piecewise constant on either side of the interface. However, jump conditions are also needed for Maxwell's equations to relate interfacial and bulk properties. The jump conditions corresponding to Eqs. (6.6), (6.9) and (6.10) are written respectively as [37, 132]

$$\vec{n} \times \|\vec{E}\| = 0, \quad (6.13)$$

$$\vec{n} \cdot \|\vec{D}\| = q^s, \quad (6.14)$$

$$\frac{\bar{\delta}q^s}{\delta t} + \vec{n} \cdot \|\vec{J} - q^s\vec{v}\| + \nabla_s \cdot \vec{K} = 0, \quad (6.15)$$

where  $q^s$  is a surface density of free charge (charge per unit surface area),  $\bar{\delta}/\delta t$  is the total time derivative in following the motion of the discontinuity surface  $\xi$  along its normal, and defined as  $\bar{\delta}/\delta t = \partial/\partial t + (\vec{v} \cdot \vec{n})(\vec{n} \cdot \nabla)$  wherein the velocity of the discontinuity surface  $\vec{u}$  is replaced by  $\vec{v}$  based on the assumption that the discontinuity surface is a material interface ( $\vec{v} = \vec{u}$ ). Here,  $\vec{K}$  is the total surface current defined as  $\vec{K} = \vec{k} + q^s\vec{u}$  where  $\vec{k}$  and  $q^s\vec{u}$  are the surface conduction and convection currents, respectively. Eq. (6.13) states that the tangential component of the electric field vector is continuous across the discontinuity surface while Eq. (6.14) reveals that the normal component of the electric displacement vector is discontinuous at the interface. (Eq. (6.15)) is the conservation of charge on the discontinuity surface.

As stated previously, the electrostatics and hydrodynamics of a fluid system can be coupled together in the momentum balance equation through the Maxwell stress tensor which accounts for the stress induced in an incompressible liquid medium due to the presence of an electric field. The Maxwell stress tensor can be written as [96, 132]

$$T^E = \vec{D}\vec{E} - 0.5(\vec{D} \cdot \vec{E})I, \quad (6.16)$$

where in Eq. (6.16), the contribution from the induced magnetic field was neglected. Upon taking the divergence of the Maxwell stress tensor and then using Eq. (6.9) and the symmetry of the gradient of the electric field vector as well as the product rule of differentiation, one can obtain the electric force  $\vec{f}^E$  per unit volume as [96, 132]

$$\vec{f}^E = q^s\vec{E} - 0.5\vec{E} \cdot \vec{E}\nabla\varepsilon^E, \quad (6.17)$$

Here, the first term on the right hand side of Eq. (6.17) is the electric force acting along the direction of the electric field due to the interaction of the free charges with the

electric field while the second term accounts for the polarization force due to the pairs of charges, which acts along the normal direction to the interface as a result of term  $\nabla \varepsilon^E$ .

### 6.2.3 Leaky dielectric model

For a two-fluid system with finite electrical conductivities in a quasistatic electric field and  $t^\mu \gg t^E$  and in the absence of buoyancy forces, both volume and surface charge conservation equations in Eqs. (6.10) and (6.15) can attain steady state condition (i.e.,  $Dq^v/Dt = 0$  and  $\bar{\delta}q^s/\delta t=0$ ) in a time scale much smaller than the viscous time scale of the fluid motion. Such a system can be referred to as conducting-conducting. Therefore, relying on the quasistatic assumption, the conservation of charge in Eq. (6.10) can be simplified to

$$\nabla \cdot (\sigma^E \vec{E}) = 0. \quad (6.18)$$

Additionally, since the electric field is irrotational ( $\nabla \times \vec{E} = 0$ ), due to the mathematical entity of  $\nabla \times \nabla \phi = 0$  (the curl of the gradient is equal to zero), which holds for any arbitrary scalar field, the electric field vector can be expressed in terms of electric potential as

$$\vec{E} = -\nabla \phi, \quad (6.19)$$

where  $\phi$  is the electric potential. This would mean that the charge conservation equation (Eq. (6.18)) in the domain can be re-written as

$$\nabla \cdot (\sigma^E \nabla \phi) = 0. \quad (6.20)$$

The interface condition for Eq. (6.20) can be written from the jump condition for the conservation of charge in Eq. (6.15) in the form of

$$\|\sigma^E \vec{E}\| \cdot \vec{n} = 0, \quad (6.21)$$

by ignoring the surface current for the computational simplicity. This interface condition is referred to as the continuity of the current across the interface. Further interface condition can be written as the continuity of the electric potential across the interface as  $\|\phi\| = 0$ . For a two-fluid system, having a constant electrical conductivity in each fluid, Eq. (6.20) for electrical potential reduces to Laplace equation ( $\nabla^2\phi = 0$ ) in each medium.

With the solution of Eq. (6.20), the electric potential can be obtained, and then the electric field strength is calculated by  $\vec{E} = -\nabla\phi$ . Based on Eq. (6.9), we can obtain the distribution of volume charge density as  $q^v = \nabla \cdot (\varepsilon^E \vec{E})$ . Having calculated the distributions of electric charge density and electric field strength, the electric force within the liquid bulk in the vicinity of interface can then be determined through Eq. (6.17) for incompressible fluid.

Upon combining Eq. (6.2) with Eqs. (5.8) and (6.17), one can obtain the equation of motion including volumetric surface tension and electric field forces as

$$\rho \frac{D\vec{v}}{Dt} = -\nabla p + \mu \nabla^2 \vec{v} + \rho \vec{f}^b + \sigma \kappa \vec{n} \delta + q^v \vec{E} - 0.5 \vec{E} \cdot \vec{E} \nabla \varepsilon^E. \quad (6.22)$$

### 6.3 Results

In this section, we consider two main test cases. The first one is the deformation of static circular droplet under the influence of the surface tension force only, which is modeled to validate the implementation of surface force and the numerical scheme. The second one is also the deformation of a droplet which is this time subjected to both surface tension and a constant externally applied electric field. The second test case has been numerically simulated under various combinations of fluid properties to reveal the capability and the accuracy of the SPH method in modeling the multiphase electrohydrodynamics problems.

The deformation of a static circular droplet under the surface tension force is a commonly utilized test case for validating the accuracy of numerically computed pressure jump

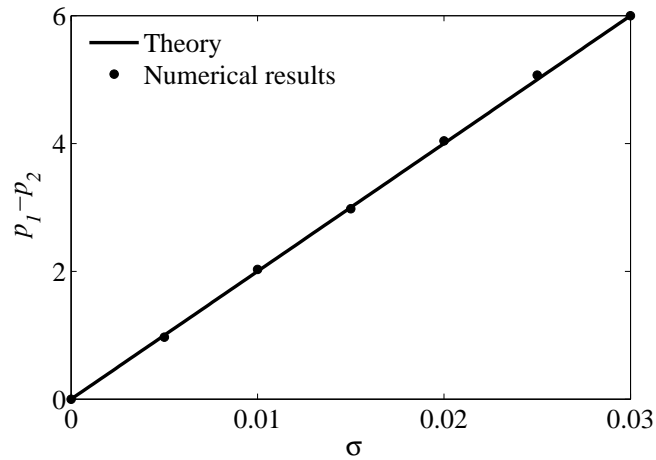


FIGURE 6.1: The comparison of numerically computed pressure jumps as a function of surface tension coefficient with that calculated by the analytical equation, namely, Laplace's law.

across the interface in multiphase systems, which can also be calculated analytically from the relation,  $p_{in} - p_{out} = \sigma/r$ . This relation is known as the Laplace's law that relates pressure difference between inside and outside of the droplet to the surface tension coefficient and the curvature (more details can be found in chapter 5). For this test problem, the computations are performed in a square domain with the edge length of  $H = 0.04$  ( $m$ ). The origin of the static circular droplet with a radius of  $r = 0.005$  ( $m$ ) is placed at the center of the square domain, which is represented by an array of  $100 \times 100$  particles in  $x$ - and  $y$ - directions, and the smoothing length for all particles is set equal to 1.6 times the initial particle spacing. The simulations are performed for constant density and viscosity values of  $\rho_1 = \rho_2 = 1000$  ( $kg/m^3$ ),  $\mu_1 = \mu_2 = 1$  ( $Pa.s$ ), respectively, and for several values of the surface tension coefficient  $\sigma$  ( $N/m$ ). Here, subscripts 1, and 2 are used to denote parameters associated with the inner and outer fluids, respectively. As for the boundary conditions of the current test case, the pressure on the boundaries is set equal to zero, and the no-slip boundary condition is imposed for velocity on all solid walls. The initial velocity field is zero. Pressure jumps computed across the interface for various surface tension coefficients are presented in Fig. 6.1 together with the results of the analytical solution, where the linear continuous line represents the results obtained from the analytical relation while the outcomes of the numerical simulations are shown with filled-in circles. From this figure, one can notice the good agreement between numerical and analytical results.

In Fig. 6.2 is shown the two dimensional problem geometry for the second test problem

which is composed of a square domain occupied by the immiscible background fluid and the initially circular droplet having the radius of  $r_o$  whose origin is located at the center of the square domain. The size of the computational domain and droplet radius for this test case is identical to that for the first one unless stated otherwise. Likewise, the modeling domain is represented by particles generated on a rectangular grid with identical and equidistant particle spacing. Additionally, for all simulations, the domain size is eight times greater than initial droplet radius. The smoothing length for all particles is set equal to 1.6 times the initial particle spacing as in the case of the first test case. In the present test case, both the droplet and background fluids have identical densities and viscosities, namely,  $(\rho_1 = \rho_2, \mu_1 = \mu_2)$ , respectively, and a constant surface tension coefficient  $\sigma$  is used. However, the inner fluid's electric permittivity  $\varepsilon_1^E$  and conductivity  $\sigma_1^E$  may differ from that of the background fluid depending on the test case studied. The relative differences in the electric permittivity and conductivity of both constituent phases are represented by their ratios as

$$S = \frac{\varepsilon_{in}^E}{\varepsilon_{out}^E} = \frac{\varepsilon_1^E}{\varepsilon_2^E}, \quad Q = \frac{\sigma_{in}^E}{\sigma_{out}^E} = \frac{\sigma_1^E}{\sigma_2^E}, \quad (6.23)$$

which are two significant parameters that play an important role in simulations which will be discussed later in details.

One of the main features that can be compared in bubble dynamics research is the droplet deformation parameter  $D$ , which is defined as

$$D = \frac{A - B}{A + B}, \quad (6.24)$$

where  $A$  and  $B$  are the diameters of the elliptic droplet which are parallel and perpendicular to the direction of the applied electric, respectively, at the steady state condition. The droplet deformation parameter quantifies the deviation in the geometry of a droplet from its original circular shape to an elliptic one. The higher the value of  $D$ , the larger the ellipticity whereas as the  $D$  goes to zero, the droplet approaches a circular shape. Besides, the positive value of  $D$  indicates that the droplet is stretched in the electric field direction thus acquiring a prolate shape while the negative value denotes that it is lengthened perpendicularly to the electric field direction (transverse direction) hence forming an oblate shape.

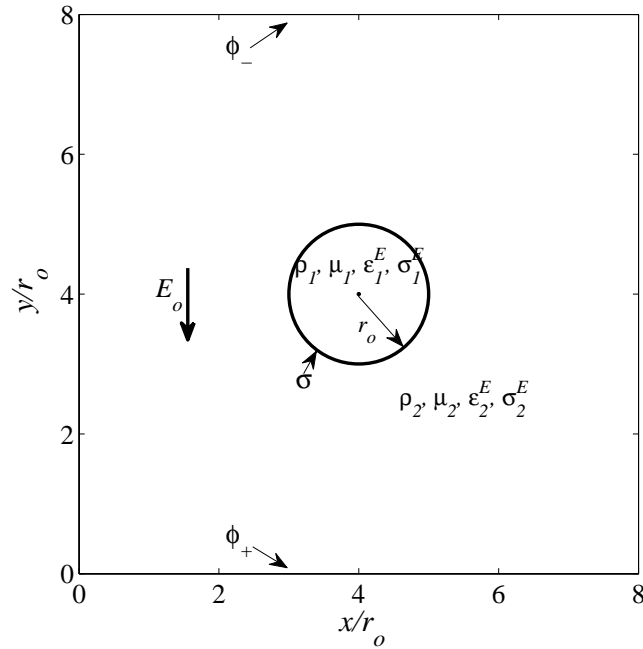


FIGURE 6.2: The schematic of the problem domain. Upon setting an electric potential at the upper and lower horizontal boundaries, a constant electric field in the downward direction is obtained in the model domain.

The numerical findings of this test case are compared with two different theories in terms of the droplet deformation parameter. The first one is the analytical equation developed by Taylor [151] which formulates the droplet deformation parameter as

$$D_T = \frac{9f_{d,T}E_o^2\epsilon_2^E r_o}{8(2+Q)^2\sigma}, \quad (6.25)$$

where  $E_o$  is the magnitude of the electric field vector (set to be  $E_o = 1$  unless stated otherwise) which is calculated as  $(\phi_+ - \phi_-)/H$  with  $\phi_- = 0$ , and  $f_{d,T}$  is the discriminating function, which is evaluated as

$$f_{d,T} = Q^2 + 1 - 2S + \frac{3}{2}(Q - S), \quad (6.26)$$

which determines the sign of  $D_T$  in the above equation so that according to  $f_{d,T}$ , the droplet may oblate or prolate.

Taylor also showed that the fluid rotation in the droplet and surrounding fluid is only dependent on the ratios between electric permittivity and conductivities. Figure 6.3

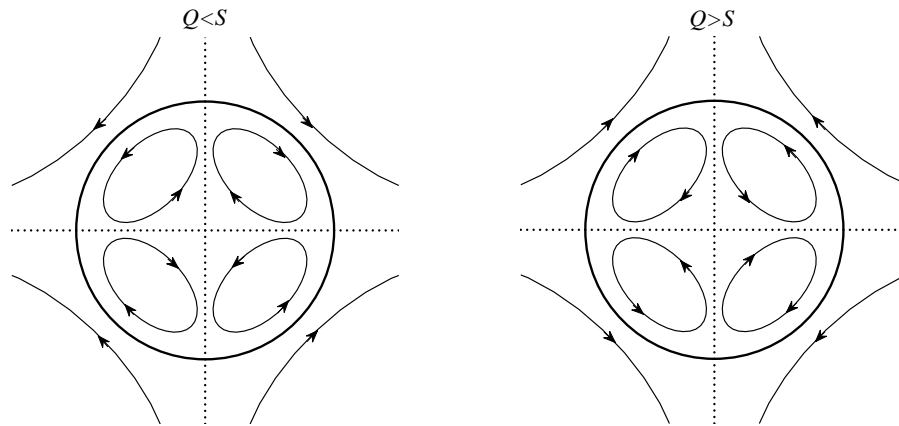


FIGURE 6.3: Schematics for two types of induced flow: (a)  $Q < S$  and (b)  $Q > S$ .

shows fluid vorticities inside and outside of a droplet subjected to a constant electric field for the conditions of the  $Q < S$  (left) and  $Q > S$  (right). Taylor's theory suggests that for the condition of  $Q < S$ , there are four vortices inside the droplet which have identical flow patterns. Namely, the flow direction is from the center of the drop toward the pole along vertical axis, from the pole to the equator along the perimeter of the drop, and from the equator to the center of the drop along the horizontal axis. However, for the condition of  $Q > S$ , the fluid circulates in the opposite direction in comparison to the first case.

The second theoretical analysis which is used to evaluate our results is the one introduced by Feng [41] wherein the droplet deformation parameter  $D$  is formulated as

$$D_F = \frac{f_{d,F} E_o^2 \varepsilon_1^E r_o}{3(1+Q)^2 S \sigma}. \quad (6.27)$$

In the above equation, the sign of  $D_F$  also depends on the sign of  $f_{d,F}$  because all the other terms have positive sign. The discriminating function  $f_{d,F}$  in Eq. (6.27) is defined as

$$f_{d,F} = Q^2 + Q + 1 - 3S. \quad (6.28)$$

If  $f_{d,F}$  is positive, the droplet deformation parameter  $D_F$  will be positive, wherefore the droplet will prolate, while the negative values of  $f_{d,F}$  result in oblate deformation of the

TABLE 6.1: The comparison of SPH and theoretical results (Eqs. (6.25) and (6.27)) in terms of the discriminating function  $f_d$  and the deformation parameter  $D$  for different combinations of conductivity and permittivities.

$\varepsilon_1^E$	$S$	$\sigma_1^E$	$Q$	$\sigma$	$f_{d,T}$	$D_T$	$f_{d,F}$	$D_F$	$D_n$
0.3	0.5	40	2	0.01	6.25	0.0659	5.5	0.06111	0.0854
0.5	0.5	40	2	0.01	6.25	0.1099	5.5	0.10185	0.1304
0.5	0.5	150	3	0.01	12.75	0.1434	11.5	0.1198	0.1683
0.5	0.5	1	0.05	0.01	-0.6725	-0.0450	-4.25	-0.0630	-0.0612
3	5	10	0.5	0.03	-15.5	-0.1395	-13.25	-0.1963	-0.2293
0.05	0.2	2	0.1	0.03	0.46	0.00248	0.51	0.0058	0.0051

droplet.

In this paper, it is shown that the results of simulations by the SPH method are in good agreement with those of theoretical analysis explained previously. In order to compare numerical results with those obtained by using Taylor and Feng theories quantitatively, Table 6.1 is presented. In this table, the droplet deformation parameter  $D$  is presented for six different sets of input parameters. As one may infer from the sign of evaluated droplet deformation  $D$  in Table 6.1, the input parameters given in the first three rows of the table lead to prolate deformation while the input parameters in the fourth and fifth rows causes the droplet to deform in the oblate form. However, the simulation with input parameters given in the last row is an exception, which will be discussed in details later by referring to Fig. 6.4.

One may notice from Table 6.1 that for small deformation parameter values in both oblate and prolate conditions, the results of numerical simulations agree very well with those of analytical analysis except that there are rather small deviations between the analytical and simulation results. However, for relatively higher values of the droplet deformation parameter, the results of numerical simulations deviate observably from those of both theories. It is important to state that the theoretical analysis of both Taylor and Feng assume that the droplet remains circular hence being accurate for small droplet deformations only. Therefore, our findings are in mesh with what have been reported in literature [157, 69, 171] wherein it was shown both experimentally and numerically that for large droplet deformations, these two analytical expressions underestimate the droplet deformation parameter. Another important point worthy of mentioning here is that for the prolate deformation, our results are closer in magnitude to those of the Taylor's theory. On the other hand, when the droplet oblates, our findings

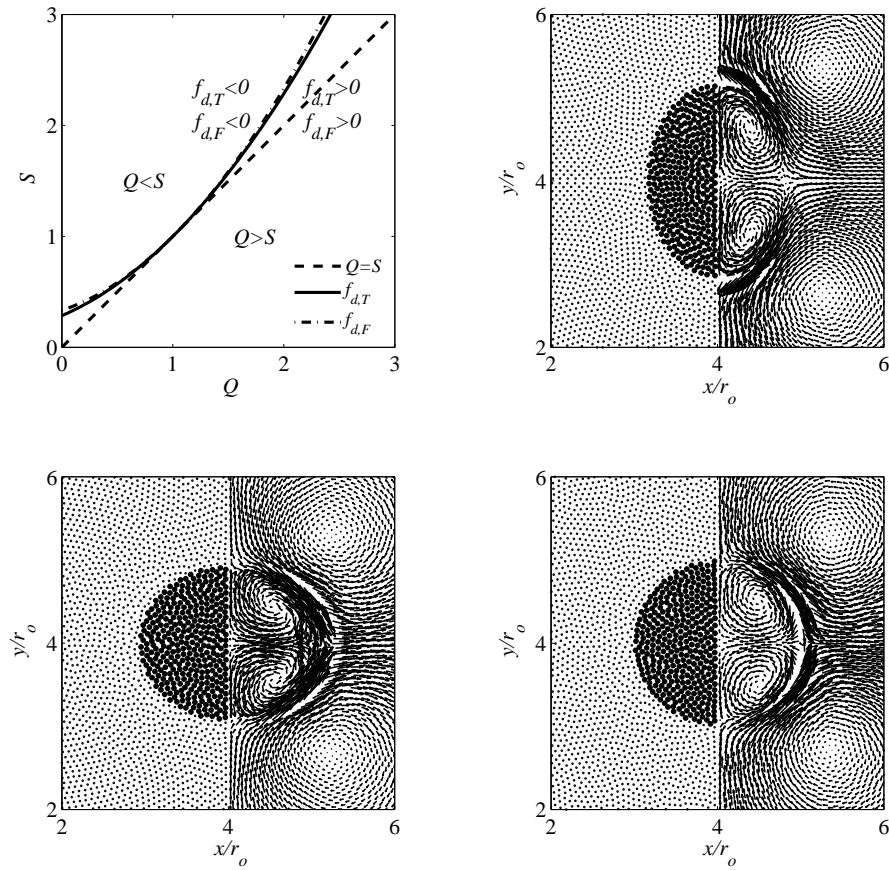


FIGURE 6.4: (a) The relation between the permittivity and the conductivity ratios: (b)  $Q > S$ ,  $f_{d,F} > 0$ ; (c)  $Q < S$ ,  $f_{d,F} < 0$ ; and (d)  $Q < S$ ,  $f_{d,F} > 0$ . Only a half of the central regions are displayed; different particle shape and size are also shown to indicate the fluid-fluid interfaces and drop deformations.

have better agreement with the results of the Feng's theory rather than the Taylor's theory. In other words, in the prolate deformation, the Taylor's theory calculates higher values for the droplet deformation parameter and the relative difference between Taylor data and ours are less than the Feng's theory. Yet, in oblate deformation, the opposite situation is observed. The reason for such a controversy is hidden in Eqs. (6.25) and (6.27) where in Feng's theory, the inner fluid permittivity is used while in Taylor's theory, the droplet deformation parameter is evaluated using the outer fluid's permittivity.

The relation between the permittivity ratio  $S$  and the conductivity ratio  $Q$  is shown in Fig. 6.4a, which is hereafter referred to as  $S - Q$  map. In this figure, the dashed straight line represents the situation of  $S = Q$ . For the case of  $Q < S$  which is the region above the dashed straight line on the map, the fluid particles inside and outside

of droplet circulate with the pattern explained earlier and depicted in Fig. 6.3a. As for the case of  $Q > S$ , the opposite flow circulation pattern should be expected. Moreover, in the same figure, the variation of  $S$  as a function of  $Q$  is plotted by utilizing the discrimination functions  $f_{d,T}$  and  $f_{d,F}$  in Eqs. (6.26) and (6.28) for the values of  $f_{d,T} = 0$  and  $f_{d,F} = 0$ , and the curves are denoted by solid and dash-dot lines, respectively. Since these two curves are almost equivalent to each other, we have provided our discussion below referring to the Feng's theory. The regions above and below this curve represent the conditions of  $f_{d,F} < 0$  and  $f_{d,F} > 0$  in the given order, which correspond to the oblate and prolate droplet deformations, respectively. Three different combinations or configurations might be formed out of the above given situations, which are plotted in Figs. 6.4b, c, and d, where the right half of each sub-figure shows particle velocity vectors and the left half represents droplet (dark) and surrounding (light) particles distribution for corresponding simulations. The first configuration, which is shown in Fig. 6.4b, belongs to the situation where  $Q > S$  and in turn  $f_{d,F} > 0$ , which can be obtained using the input parameters given in the first three rows of Table6.1. The results in Fig. 6.4b are obtained by using the simulation parameters provided in the second row of the Table6.1. As a result, the flow circulation inside the droplet is according to Fig. 6.3b, and the droplet prolates. The second combination shown in Fig. 6.4c represents the  $Q < S$  and as a result  $f_{d,F} < 0$ , which leads to the formation of the flow pattern as illustrated in Fig. 6.3a and oblate droplet deformation. Under this configuration, the droplet deformation is a representative figure for the fourth and fifth rows of Table6.1. The input parameters for the Fig. 6.4c is given in the forth row of the Table6.1. The third configuration (i.e.,  $Q < S$  and  $f_{d,F} > 0$ ) forms when the problem conditions belong to the small region flanked by the straight and curved lines. In this configuration, as can be observed from Fig. 6.4d for which the input parameters are given in the last row of the Table6.1, the droplet tends to prolate due to the fact that  $f_{d,F} > 0$  while the flow pattern is opposite to Fig. 6.4b. One can note that the droplet does not prolate severely, which is a quite expected result since the input parameters result in  $S$ ,  $Q$ , and  $f_{d,F}$  values that fall into the region between the straight and curved lines in the  $S - Q$  map.

Figure 6.5 shows the variation of droplet deformation with respect to different parameter changes. In subfigures, electric field strength, droplet initial radius, inner fluid permittivity, and surface tension coefficient are separately varied to show the dependency of

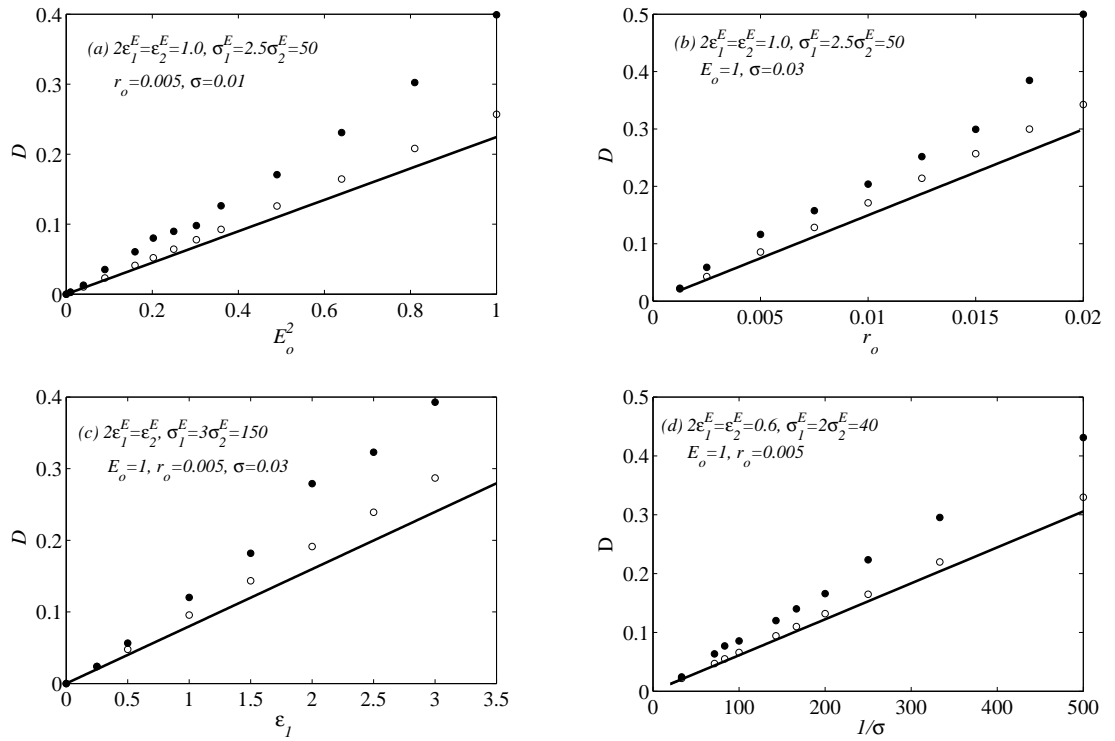


FIGURE 6.5: The variation of droplet deformation parameter  $D$  as a function of (a) the electric field strength  $E_o$ , (b) the permittivity  $\varepsilon_1^E$ , (c) the initial droplet radius  $r_o$ , and (d) the reciprocal of the surface tension  $1/\sigma$ .

droplet deformation to each parameter. In these figures, the solid lines and unfilled circles represent the results of Feng and Taylor theories, respectively, while the numerical values are shown with filled circles. It is observed that for all cases, our numerical simulations for larger droplet deformations have overestimated values of  $D$  calculated by both theoretical analyses. However, as discussed before, for small deformations, the overestimation is relatively small.

Other parameters that can be compared with the theory are the velocity profiles of fluid media inside and outside of droplet. Thanks to Feng [41], the fluid velocity inside and outside the droplet may be evaluated theoretically as,

$$v_{r,in} = U^*[(r/r_o)^3 - (r/r_o)] \cos 2\theta, \quad (6.29)$$

$$v_{\theta,in} = U^*[(r/r_o) - 2(r/r_o)^3] \sin 2\theta, \quad (6.30)$$

$$v_{r,out} = U^*[(r_o/r) - (r_o/r)^3] \cos 2\theta, \quad (6.31)$$

$$v_{\theta,out} = -U^*[(r_o/r)^3] \sin 2\theta, \quad (6.32)$$

where  $r$  is the radial position,  $v_r$  and  $v_\theta$  are the radial and tangential velocities in the given order. Also, the  $U^*$  is the characteristic velocity, which corresponds to the maximum velocity

$$U^* = \frac{Q - S}{2S(1 + Q)^2} \frac{\varepsilon_1^E E_o^2 r_o}{\mu_1 + \mu_2}. \quad (6.33)$$

These equations carry some valuable conceptual facts which are perfectly captured by current simulations. First, for the radial velocity, in both expressions for inner and outer fluid velocities, the fluid velocity approaches zero near the droplet boundary. Moreover, the maximum radial velocity may be observed where the cosine function in Eqs. (6.29) and (6.31) is maximized. This happens at angles like  $\theta = 0$ , and  $\pi/2$ . On the other hand, for the angles like  $\pi/4$  at which the sinusoidal function has its maximum value, the tangential velocity is maximized.

Figure 6.6 shows the profiles of the radial and tangential velocity components for two different angles at which one of the velocity components is maximized. In this figure, the theoretical velocity profile for radial and tangential components are shown with solid and dashed lines, respectively. Also, the numerical data for radial and tangential velocity components are represented with unfilled and filled circles, respectively. In accordance with Eqs. (6.30) and (6.32), the tangential velocity component has to be zero at  $\theta = 0$ , which is observed in Fig. 6.6a where the radial velocity may have its maximize values. Eqs. (6.29) and (6.31) require that for the circular droplet, the radial velocity should be zero at the droplet interface where  $r = r_o$ . Nevertheless, after the droplet gets deformed, its interface is no longer at  $r = r_o$ . Thus, the numerical results show a slight deviation in evaluation of zero radial velocity prediction, which is again due to the assumption made in theory that the droplet remains circle.

Finally, to show the convergence of our results with respect to particle resolution, one of the test cases is reexamined here. In this case, the numerical parameters are set

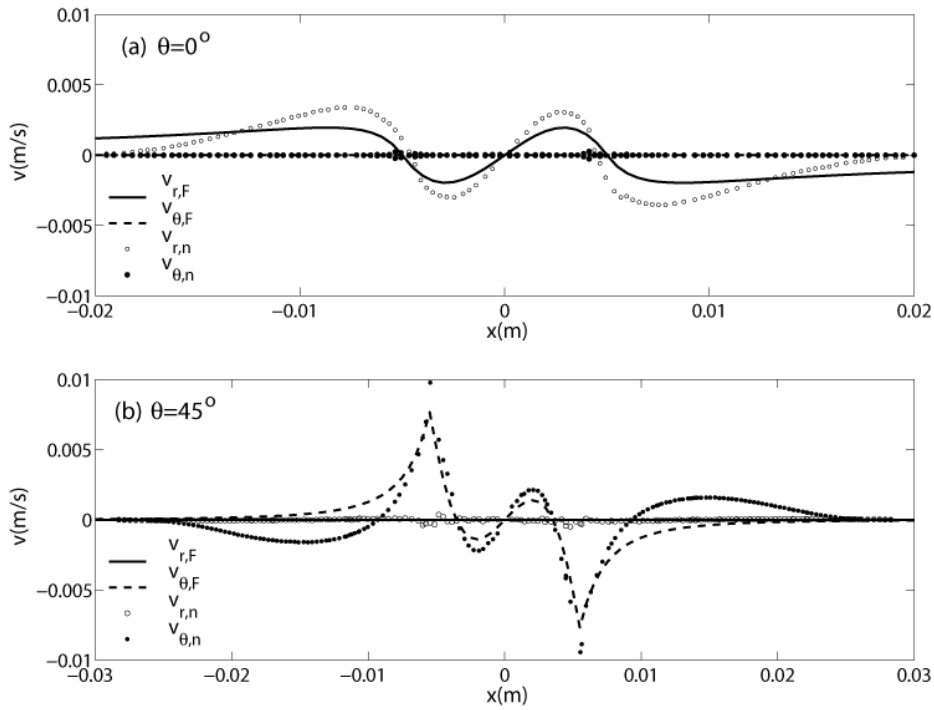


FIGURE 6.6: The profiles for the components of the velocity profile and their comparison with analytical results (a) for the case of  $\theta = 0$ , (b) for the case of  $\theta = \pi/4$ . This figures are generated from the simulation with input parameters provided in the forth row of Table6.1 after the steady state has been reached.

to  $S = 0.5$ ,  $Q = 2.0$ ,  $\sigma_1^E = 40$ ,  $\varepsilon_1^E = 0.3$ , and the surface tension coefficient has the value of 0.012. Under this condition, the droplet prolates as the calculated deformation parameter is equal to  $D = 0.077$ . Figure 6.7a represents the fluid particles' positions for four different particle resolutions of  $60 \times 60$ ,  $80 \times 80$ ,  $100 \times 100$ , and  $120 \times 120$  for the quarter of the entire domain. Figure 6.7b shows the corresponding velocity vectors inside and outside the droplet.

A close observation on Fig. 6.7a reveals that for low particle resolution cases, i.e.  $60 \times 60$  and  $80 \times 80$ , the droplet deformation is dependent on the particle resolution. However, as the particle resolution increases, this dependency vanishes so that the droplet deformation is identical for  $100 \times 100$ , and  $120 \times 120$  particle resolutions. Moreover, Fig. 6.7b clearly reveals that as the particle resolution increases, the center of vorticities inside and outside of droplet converges to a certain location, so that the position of vorticity centers are independent of particle resolution at high values. This brings the conclusion that considering the computational costs and the satisfactory accuracy of  $100 \times 100$  particle resolution, as well as minor quantitative and qualitative difference between  $100 \times 100$ ,

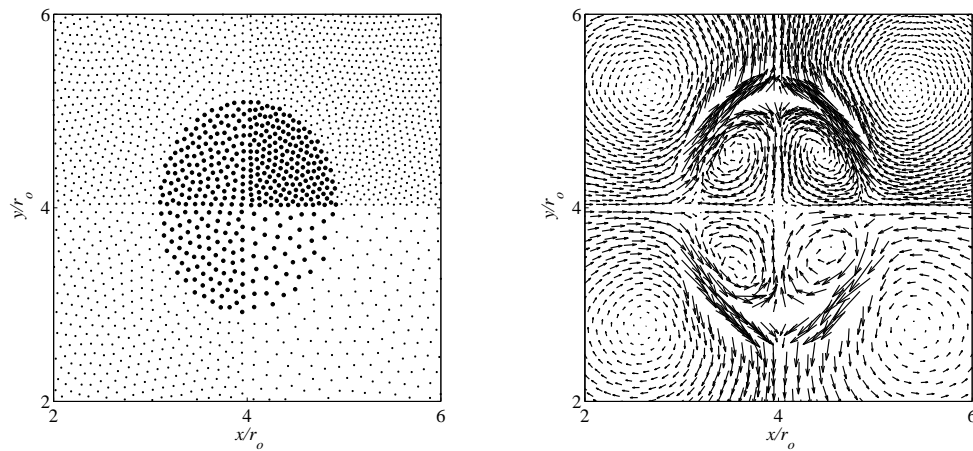


FIGURE 6.7: (a) Particle position distribution, and (b) velocity vectors, for different particle resolutions of  $60 \times 60$ ,  $80 \times 80$ ,  $100 \times 100$ , and  $120 \times 120$ .

and  $120 \times 120$  results, the particle resolution of  $100 \times 100$  has been employed for all the simulations for which results are presented.

## 6.4 Conclusion

In this chapter, the SPH method has been extended to model EHD of a droplet suspended inside a neutral viscous fluid with different electrical and hydrodynamical properties. To be able couple electric field forces, surface tension forces, droplet deformation, and flow fields, momentum balance equations with the source terms for the electric field and surface tension forces on the droplet interface are solved together with a set of Maxwell equations simplified by the using leaky dielectric model. The electric field force is included in the momentum balance equations as volumetric forces through taking the divergence of the Maxwell stress tensor. Quite many simulations have been performed to investigate the effects of the electric field strength, permittivity ratios, and electrical conductivity ratios, surface tension and the initial droplet radius on the droplet deformation parameter. It is found that in the leaky dielectric model, droplets deform in either prolate or oblate manners depending on the ratios of electrical conductivity and permittivity. The simulation results have been validated by two theories and shown to agree well with those predicted by both theories for small droplet deformation parameters. However, it is observed that the numerical results overestimate the analytically

calculated droplet deformation parameters for high deformations, which was also underscored in some other relevant works in literature. The reason behind this discrepancy lies in the assumption made by theories such that droplet deformation is rather small, and hence the droplet remains nearly circular after the deformation. Depending on the relative magnitudes of the electric permittivity and conductivity ratios (i.e., the case of  $Q > S$ , or  $S > Q$ ), flow circulations have different patterns. The electric field strength only affects the magnitude of drop deformation. The intensity of the circulatory flow motion gets stronger when the droplet is subject to a larger deformation due to the high value of the steady electric field. The results of the current work suggest that the SPH method is able to capture the physics behind the droplet deformation under the influence of a steady electric field in robust and accurate manner.

## Chapter 7

# Future Works

**High performance computing:** Although researchers have done numerous interesting works, these works are usually limited either to the simplification assumptions in the analytical approach or to the highly expensive devices and facilities in experiments. With the recent significant enhancement in the computational technology the computational modeling becomes more and more attractive. Thanks to the massive parallel processing technology one can easily solve the full Navier-Stoke equations without any simplification even for the three dimensional problems in a small fraction of time. This enables us to solve real life scientific and industrial applications in a more accurate and cheaper way. Benefitting from not having inter-linked particles, SPH has a great potential to be treated in parallel clusters. Especially the three main component of the SPH namely, neighbor list construction, force computation, and the integration of the equation of motion have capabilities to be computed in a parallel algorithm. The code can be further developed to three dimensions that uses the Compute Unified Device Architecture (CUDA) programing developed by Nvidia for executing a larg number of particles on a Graphical Processing Unit (GPU). This provides us a powerful tool (the computer performance of couple of teraflop) which performs the massive parallel computation on a cheap cluster (less than 1000 USD at the moment). Considering the fact that with achieveing this type of parallel processing, simulation of more challenging and realistic three-dimensional problems will be feasible in the near future.

**Three or more phases flows:** Multiphase flow where two or more fluid have interfacial surface occurs in various applications including hydrocarbon reservoirs, oil pipes,

drug injection. In many engineering problems, determining free surface and tracking interfaces are of particular importance. Multiphase flow problems so far have been studied widely using mesh dependent techniques. Nevertheless, because of the complexity of these problems, most current works has not gone beyond the simple ones. In mesh-dependent methods, additional equations have to be solved to track interfacial surface, and depending on the problem in hand, mesh-refinement might be required. The SPH method due to its Lagrangian nature is an excellent candidate to address complex flow phenomena such as free surface, and interfacial surface. As a first practical application for multiphase flow modeling, the deformation of a compound drop with multiple interfaces in a flow field can be solved. When many compound drops exist in another liquid medium, the mixture formed is referred to as multiple emulsion; for example, water in oil compound suspending in water, abbreviated as (w-o-w) emulsion. w-o-w system was proposed as a drug delivery vehicle for insulin, and is widely encountered in polymer processing applications as well. In the literature, little attention has been given to the deformation and morphological evolution of compound drops in flow fields. These are practically important issues since shear-induced burst of the oil shell is an important mechanism for drug release. Modeling the deformation of a compound drop is a computational challenge because of the two moving and deforming interfaces. It needs endeavor the development of a new approaches to track the interfaces and accurately compute momentum transfer across the multiple interfaces by using color fields, or level set method (whichever is more efficient). The second practical application with scientific and industrial significance is the modeling of non-Newtonian fluid flow under the effect of electric field through a capillary tube. The study intends to shed a light on the flow nature and the droplet formation at the end of a capillary tube where the surface tension strength as well as electric field distribution control "necking" behavior and droplet size. This problem has many practical applications such as electro spinning of polymers for producing nano-fibers, and droplet-droplet and oil-surface interactions.

**Fluid-Structure interaction:** Fluid-Structure interaction (FSI) is one of the challenging problems in the field of computational fluid dynamics. Typical examples include flow around aircrafts wings, bridges and other many complex structures. There are two main approaches for solving FSI problems. The first one is Monolithic approach which solves the governing equations of fluid and structure displacement simultaneously and

the second one is partitioned approach which solves these equations separately. In general, Lagrangian-Eulerian methods (LE) have been used in literature, which implements Eulerian formulation for fluid and Lagrangian formulation for solid structure. However this approach, when the deformation of the solid is large, faces numerous difficulties such as transferring data between fluid and the solid structure. To overcome these modeling difficulties, it would be a prudent choice to use Lagrangian formulations for both fluid and solid sites, because Lagrangian methods can solve the governing equations of fluid and structure simultaneously without implementing any specific treatment for data transfer from one region to another. The Lagrangian nature of SPH method lends itself excellently to the simulation of a variety of complex fluid flow processes such FSI. In this work a modified SPH algorithm should be implemented to solve problems including fluid flow in interaction with compatible structures under a large deformation. One possible modification of this algorithm can be based on neglecting the intermediate data transfer steps terms, which result in an easy and time-saving numerical simulation method. The algorithm needs to be developed further so that it can solve the fluid site with incompressible SPH and can handle more complex test applications such as the impact of an object to a liquid surface.

**Turbulent multiphase flows:** The turbulent multiphase problem contains extremely destructive and dangerous natural hazards. There is a significant need for reliable methods for predicting the dynamics, run-out distances, mass transport, and inundation areas of such events. They consist of a broad distribution of soil/ice sizes mixed with fluid. The flow behavior can vary and depends on the sediment composition and percentage of solid and fluid phases. Strong coupling between the solid- and fluid-momentum transfer leads to simultaneous deformation, mixing, and separation of the phases. Also, the evolution, advection, and diffusion of the solid-volume fraction play important roles in these phenomena. Due to the problem complexity, strong phase coupling and highly nonlinear nature of its equation, comprehensive theory accounting for all the interactions between the solid particles and the fluid is still out of reach. The mathematical models and computational solution algorithms can be further develops in the way that it can count and describe all existing forces and predict the whole physics behind these phenomena.

# Appendix A

## First and second order approximations

The following section provides derivations for the SPH approximation to first- and second-order derivatives of a vector-valued function. The derivations are carried out in Cartesian coordinates. The SPH approximation for the gradient of a vectorial function starts with a Taylor series expansion of  $f^p(\vec{r}_j)$  so that

$$f^p(\vec{r}_j) = f^p(\vec{r}_i) + r_{ji}^l \frac{\partial f^p(\vec{r}_i)}{\partial x_i^l} \Big|_{\vec{r}_j=\vec{r}_i} + \frac{1}{2} r_{ji}^l r_{ji}^k \frac{\partial^2 f^p(\vec{r}_i)}{\partial x_i^l \partial x_i^k} \Big|_{\vec{r}_j=\vec{r}_i}. \quad (\text{A.1})$$

Upon multiplying Eq. (A.1) by the term,  $\frac{\partial W_{ij}}{\partial x_j^s}$ , and then integrating over the whole space,  $d^3\vec{r}_j$ , one can write,

$$\begin{aligned} \int_{\Omega} (f^p(\vec{r}_j) - f^p(\vec{r}_i)) \frac{\partial W_{ij}}{\partial x_j^s} d^3\vec{r}_j &= \frac{\partial f^p(\vec{r}_i)}{\partial x_i^l} \underbrace{\int_{\Omega} r_{ji}^l \frac{\partial W_{ij}}{\partial x_j^s} d^3\vec{r}_j}_{I^{ls}} \\ &+ \frac{1}{2} \frac{\partial^2 f^p(\vec{r}_i)}{\partial x_i^l \partial x_i^k} \underbrace{\int_{\Omega} r_{ji}^l r_{ji}^k \frac{\partial W_{ij}}{\partial x_j^s} d^3\vec{r}_j}_{I^{lks=0}}. \end{aligned} \quad (\text{A.2})$$

Note that the first and the second integrals on the right hand side of Eq. (A.2) are, respectively, second- and third-rank tensors. The third-rank tensor can be integrated by parts, which, upon using the Green-Gauss theorem produces Eq. (A.3) since the kernel

$W_{\mathbf{ij}}$  vanishes beyond its support domain

$$I^{lks} = - \int_{\Omega} W_{\mathbf{ij}} \frac{\partial}{\partial r_{\mathbf{j}}^s} \left( r_{\mathbf{ji}}^l r_{\mathbf{ji}}^k \right) d^3 \vec{\mathbf{r}}_{\mathbf{j}} = - \int_{\Omega} W_{\mathbf{ij}} \left( r_{\mathbf{ji}}^l \delta^{sk} + r_{\mathbf{ji}}^k \delta^{ls} \right) d^3 \vec{\mathbf{r}}_{\mathbf{j}}. \quad (\text{A.3})$$

Recalling that the kernel function is spherically symmetric even function and the multiplication of an even function by an odd function produces an odd function. Integration of an odd function over a symmetric domain leads to zero

$$I^{lks} = -\delta^{sk} \int_{\Omega} r_{\mathbf{ji}}^l W_{\mathbf{ij}} d^3 \vec{\mathbf{r}}_{\mathbf{j}} - \delta^{ls} \int_{\Omega} r_{\mathbf{ji}}^k W_{\mathbf{ij}} d^3 \vec{\mathbf{r}}_{\mathbf{j}} = 0. \quad (\text{A.4})$$

Following the above described procedure identically, the second rank tensor,  $I^{ls}$ , can be written as

$$I^{ls} = -\delta_{ls} \underbrace{\int_{\Omega} W_{\mathbf{ij}} d^3 \vec{\mathbf{r}}_{\mathbf{j}}}_{=1} = -\delta^{ls}. \quad (\text{A.5})$$

On combining Eq. (A.2) with Eq. (A.4) and (A.5), one can write,

$$\frac{\partial f^p(\vec{\mathbf{r}}_{\mathbf{i}})}{\partial x_{\mathbf{i}}^s} = \int_{\Omega} (f^p(\vec{\mathbf{r}}_{\mathbf{j}}) - f^p(\vec{\mathbf{r}}_{\mathbf{i}})) \frac{\partial W_{\mathbf{ij}}}{\partial x_{\mathbf{i}}^s} d^3 \vec{\mathbf{r}}_{\mathbf{j}}. \quad (\text{A.6})$$

Note that in Eq. (A.6), the relationship  $\frac{\partial W_{\mathbf{ij}}}{\partial x_{\mathbf{j}}^s} = -\frac{\partial W_{\mathbf{ij}}}{\partial x_{\mathbf{i}}^s}$  has been used. Replacing the integration in Eq. (A.6) with SPH summation over particle “ $\mathbf{j}$ ” and setting  $d^3 \vec{\mathbf{r}}_{\mathbf{j}} = m_{\mathbf{j}}/\rho_{\mathbf{j}}$ , we can obtain the gradient of a vector-valued function in the form of SPH interpolation as,

$$\frac{\partial f^p(\vec{\mathbf{r}}_{\mathbf{i}})}{\partial x_{\mathbf{i}}^s} = \sum_{\mathbf{j}=1}^N \frac{1}{\psi_{\mathbf{j}}} (f^p(\vec{\mathbf{r}}_{\mathbf{j}}) - f^p(\vec{\mathbf{r}}_{\mathbf{i}})) \frac{\partial W_{\mathbf{ij}}}{\partial x_{\mathbf{i}}^s} d^3 \vec{\mathbf{r}}_{\mathbf{j}}. \quad (\text{A.7})$$

It is important to note that the second rank tensor  $I^{ls}$ , shown to be equal to kronecker delta for a continuous function, may not be equal to kronecker delta for discrete particles. Hence, for the accuracy of the computations, this term should be included in the SPH gradient interpolation of a function. From Eq. (A.2), we can write

$$\sum_{\mathbf{j}=1}^N \frac{1}{\psi_{\mathbf{j}}} (f^p(\vec{\mathbf{r}}_{\mathbf{j}}) - f^p(\vec{\mathbf{r}}_{\mathbf{i}})) \frac{\partial W_{\mathbf{ij}}}{\partial x_{\mathbf{i}}^s} d^3 \vec{\mathbf{r}}_{\mathbf{j}} = \frac{\partial f^p(\vec{\mathbf{r}}_{\mathbf{j}})}{\partial x_{\mathbf{i}}^l} \sum_{\mathbf{j}=1}^N \frac{1}{\psi_{\mathbf{j}}} \frac{\partial W_{\mathbf{ij}}}{\partial x_{\mathbf{i}}^s} d^3 \vec{\mathbf{r}}_{\mathbf{j}}. \quad (\text{A.8})$$

Eq. (A.8) can be written in matrix form as

$$\begin{bmatrix} \sum_{\mathbf{j}}^N f_{\mathbf{j}\mathbf{i}}^{(1)} a_{\mathbf{j}}^{(1)} \\ \sum_{\mathbf{j}}^N f_{\mathbf{j}\mathbf{i}}^{(1)} a_{\mathbf{j}}^{(2)} \end{bmatrix} = \begin{bmatrix} \sum_{\mathbf{j}}^N r_{\mathbf{j}\mathbf{i}}^{(1)} a_{\mathbf{j}}^{(1)} & \sum_{\mathbf{j}}^N r_{\mathbf{j}\mathbf{i}}^{(2)} a_{\mathbf{j}}^{(1)} \\ \sum_{\mathbf{j}}^N r_{\mathbf{j}\mathbf{i}}^{(1)} a_{\mathbf{j}}^{(2)} & \sum_{\mathbf{j}}^N r_{\mathbf{j}\mathbf{i}}^{(2)} a_{\mathbf{j}}^{(2)} \end{bmatrix} \begin{bmatrix} \frac{\partial f_{\mathbf{i}}^{(1)}}{\partial x_{\mathbf{i}}^{(1)}} \\ \frac{\partial f_{\mathbf{i}}^{(1)}}{\partial x_{\mathbf{i}}^{(2)}} \end{bmatrix} \quad (\text{A.9})$$

where  $a_{\mathbf{j}}^s = \frac{1}{\psi_{\mathbf{j}}} \frac{\partial W_{\mathbf{ij}}}{\partial x_{\mathbf{i}}^s}$ .

Starting with the relation for the SPH second-order derivative approximation [168] of a vector valued-function  $f^p(\vec{\mathbf{r}}_{\mathbf{i}})$  given in Eq. (A.10)

$$2 \int_{\Omega} (f^p(\vec{\mathbf{r}}_{\mathbf{i}}) - f^p(\vec{\mathbf{r}}_{\mathbf{j}})) \frac{r_{\mathbf{ij}}^s}{r_{\mathbf{ij}}^2} \frac{\partial W_{\mathbf{ij}}}{\partial x_{\mathbf{i}}^m} d^3 \vec{\mathbf{r}}_{\mathbf{j}} = \frac{2}{\xi} \frac{\partial^2 f^p(\vec{\mathbf{r}}_{\mathbf{i}})}{\partial x_{\mathbf{i}}^s \partial x_{\mathbf{i}}^m} + \frac{1}{\xi} \frac{\partial^2 f^p(\vec{\mathbf{r}}_{\mathbf{i}})}{\partial x_{\mathbf{i}}^k \partial x_{\mathbf{i}}^k} \delta^{sm}, \quad (\text{A.10})$$

which, upon contracting on indices  $p$  and  $s$ , one can obtain

$$2 \int_{\Omega} (f^p(\vec{\mathbf{r}}_{\mathbf{i}}) - f^p(\vec{\mathbf{r}}_{\mathbf{j}})) \frac{r_{\mathbf{ij}}^p}{r_{\mathbf{ij}}^2} \frac{\partial W_{\mathbf{ij}}}{\partial x_{\mathbf{i}}^m} d^3 \vec{\mathbf{r}}_{\mathbf{j}} = \frac{1}{\xi} \frac{\partial^2 f^p(\vec{\mathbf{r}}_{\mathbf{i}})}{\partial x_{\mathbf{i}}^k \partial x_{\mathbf{i}}^k} \delta^{pm}. \quad (\text{A.11})$$

Note that the first term on the right hand side of Eq. (A.10) becomes  $\frac{\partial^2 f^p(\vec{\mathbf{r}}_{\mathbf{i}})}{\partial x_{\mathbf{i}}^p \partial x_{\mathbf{i}}^m}$  and consequently drops off if the vector-valued function  $f^p(\vec{\mathbf{r}}_{\mathbf{i}})$  is assumed to be divergence-free velocity field. Here, the coefficient  $\xi$  takes the value of 4 and 5 in two and three dimensions, respectively. We have shown in Eqs. (A.2) and (A.5) that Kronecker delta can be written as,

$$\delta^{pm} = \int_{\Omega} r_{\mathbf{ij}}^p \frac{\partial W_{\mathbf{ij}}}{\partial x_{\mathbf{i}}^m} d^3 \vec{\mathbf{r}}_{\mathbf{j}}. \quad (\text{A.12})$$

Casting Eq. (A.12) into Eq. (A.11) leads to

$$2 \int_{\Omega} (f^p(\vec{\mathbf{r}}_{\mathbf{i}}) - f^p(\vec{\mathbf{r}}_{\mathbf{j}})) \frac{r_{\mathbf{ij}}^p}{r_{\mathbf{ij}}^2} \frac{\partial W_{\mathbf{ij}}}{\partial x_{\mathbf{i}}^m} d^3 \vec{\mathbf{r}}_{\mathbf{j}} = \frac{1}{\xi} \frac{\partial^2 f^p(\vec{\mathbf{r}}_{\mathbf{i}})}{\partial x_{\mathbf{i}}^k \partial x_{\mathbf{i}}^k} \int_{\Omega} r_{\mathbf{ij}}^p \frac{\partial W_{\mathbf{ij}}}{\partial x_{\mathbf{i}}^m} d^3 \vec{\mathbf{r}}_{\mathbf{j}}. \quad (\text{A.13})$$

Eq.(A.13) can be written in matrix form as

$$\sum_{\mathbf{j}}^N \left( f_{\mathbf{j}\mathbf{i}}^{(1)} r_{\mathbf{j}\mathbf{i}}^{(1)} + f_{\mathbf{j}\mathbf{i}}^{(2)} r_{\mathbf{j}\mathbf{i}}^{(2)} \right) \begin{bmatrix} a_{\mathbf{j}}^{(1)} \\ a_{\mathbf{j}}^{(2)} \end{bmatrix} = \begin{bmatrix} \sum_{\mathbf{j}}^N r_{\mathbf{j}\mathbf{i}}^{(1)} a_{\mathbf{j}}^{(1)} & \sum_{\mathbf{j}}^N r_{\mathbf{j}\mathbf{i}}^{(2)} a_{\mathbf{j}}^{(1)} \\ \sum_{\mathbf{j}}^N r_{\mathbf{j}\mathbf{i}}^{(1)} a_{\mathbf{j}}^{(2)} & \sum_{\mathbf{j}}^N r_{\mathbf{j}\mathbf{i}}^{(2)} a_{\mathbf{j}}^{(2)} \end{bmatrix} \begin{bmatrix} \frac{\partial^2 f_{\mathbf{i}}^{(1)}}{\partial x_{\mathbf{i}}^k \partial x_{\mathbf{i}}^k} \\ \frac{\partial^2 f_{\mathbf{i}}^{(2)}}{\partial x_{\mathbf{i}}^k \partial x_{\mathbf{i}}^k} \end{bmatrix} \quad (\text{A.14})$$

Upon contracting on indices  $s$  and  $m$  of Eq. (A.10), an alternative form of Laplacian for a vector field can be obtained as

$$8 \sum_{j=1}^N \frac{1}{\psi_j} (f^p(\vec{r}_i) - f^p(\vec{r}_j)) \frac{r_{ij}^s}{r_{ij}^2} \frac{\partial W_{ij}}{\partial x_i^m} d^3\vec{r}_j = \frac{2}{\xi} \frac{\partial^2 f^p(\vec{r}_i)}{\partial x_i^s \partial x_i^m} + \frac{1}{\xi} \frac{\partial^2 f^p(\vec{r}_i)}{\partial x_i^k \partial x_i^k} \delta^{sm}. \quad (\text{A.15})$$

If the trace of the Kronecker delta in Eq. (A.15) is replaced by the trace of Eq. (A.15), one can obtain an alternative form of corrective SPH interpolation for a Laplacian.

# Appendix B

## Publications

### *Journal Papers:*

1. A. Zainali, N. Tofghi, **M. Safdari Shadloo**, M. Yildiz, "Numerical investigation of Newtonian and non-Newtonian multiphase flows using ISPH method", *Comput. Methods Appl. Mech. Engrg.* 2013 (254) 99113.
2. **Mostafa Safdari Shadloo**, Amir Zainali, Mehmet Yildiz, "Simulation of Single Mode Rayleigh-Taylor Instability by SPH Method", *Computational Mechanics*, DOI 10.1007/s00466-012-0746-2.
3. **Mostafa Safdari Shadloo**, Amir Zainali, Mehmet Yildiz, Afzal Suleman, "A Robust Weakly Compressible SPH Method and its Comparison with Truly Incompressible SPH", *International Journal for Numerical Methods in Engineering*, 2011 (89) 939 956.
4. **M. Safdari Shadloo**, M. Yildiz, "Numerical modeling of Kelvin-Helmholtz Instability Using Smoothed Particle Hydrodynamics Method", *International Journal for Numerical Methods in Engineering*, 2011 (87) 988 1006.
5. **M. Safdari Shadloo**, A. Zainali, S. H. Sadek, M. Yildiz, "Improved Incompressible Smoothed Particle Hydrodynamics Method for Simulating Flow around Bluff Bodies", *Computer Methods in Applied Mechanics and Engineering*, 2011 (200) 1008– 1020.

6. **M. S. Shadloo**, A. Rahmat, M. Yildiz, "The electrohydrodynamics deformation of a suspended droplet in a neutrally buoyant Newtonian fluid", *Computational Mechanics*, (Nov. 2012 Submitted).
7. **Mostafa Safdari Shadloo**, Amin Rahmat, Mehmet Yildiz, "Numerical Investigation of Two Phase Rayleigh-Taylor Instability", *Physics of Fluid*, in preparation.
8. **Mostafa Safdari Shadloo**, Amin Rahmat, Mehmet Yildiz, " The electrohydrodynamics' Rayleigh-Taylor Instability", *Physics of Fluid*, in preparation.
9. **Mostafa Safdari Shadloo**, Robert Weiss, Robert. A. Dalrymple, Alexis Herculault, Giuseppe Bilotta, Mehmet Yildiz, "SPH Simulations of the Breaking and Non-breaking Long Waves: Validation with Experiments and Analytical Theory", *Coastal Engineering*, in preparation.

*Conference Papers:*

1. **Mostafa Safdari Shadloo**, "Mehmet Yildiz, Simulation of Rayleigh-Taylor Instability by Smoothed Particles Hydrodynamics: Advantages and Limitations", 7th Symposium on Numerical Analysis of Fluid Flow and Heat Transfer, 19-25 Sept., 2012, Kos, Greece.
2. **M. S. Shadloo**, M. Yildiz, "Two-Phase Electrohydrodynamics by Smoothed Particles Hydrodynamic", *International Conference on Numerical Methods in Multiphase Flows*, 12-14 June, 2012, Penn State University, State College, Pennsylvania, United States.
3. **Mostafa Safdari Shadloo**, Mmehet Yildiz, "Kelvin-Helmholtz Instability by SPH", 2nd conference on Particle-Based Methods (PARTICLES 2011), Barcelona, Spain, 26-28 Oct. 2011.
4. **Mostafa Safdari Shadloo**, Mehmet Yildiz, "ISPH Modeling of Rayleigh-Taylor Instability", 6th International SPHERIC SPH Workshop, Hamburg University of Technology, Germany, 8-11 June 2011, p:179-186.
5. **Mostafa Safdari Shadloo**, Amir Zainali, Mehmet Yildiz, "Bluff-body Simulation by SPH Method with Relatively High Reynolds Number in Laminar Flow Regime", *FEDSM-ICNMM 2010-31135*, 1-4 Aug. 2010, Montreal, Qubec, Canada.

6. **Mostafa Safdari Shadloo**, Amir Zainali, Mehmet Yildiz, "Fluid-Structure Interaction Simulation by Smoothed Particles Hydrodynamic", FEDSM-ICNMM 2010-31137, 1-4 Aug. 2010, Montreal, Qubec, Canada.
7. **Mostafa Safdari Shadloo**, Amir Zainali, Mehmet Yildiz, "Improved Solid Boundary Treatment Method for the Solution of Flow over an Airfoil and Square Obstacle by SPH Method", 5th International SPHERIC SPH Workshop, The University of Manchester, UK, 23-25 Jun. 2010, p:37-41.

# Bibliography

- [1] SI Abarzhi, K. Nishihara, and J. Glimm. Rayleigh-taylor and richtmyer-meshkov instabilities for fluids with a finite density ratio. *Physics Letters A*, 317(5-6):470–476, 2003.
- [2] O. Agertz, B. Moore, J. Stadel, D. Potter, F. Miniati, J. Read, L. Mayer, A. Gawryszczak, A. Kravtsov, Å. Nordlund, et al. Fundamental differences between sph and grid methods. *Monthly Notices of the Royal Astronomical Society*, 380(3):963–978, 2007.
- [3] I. Alfaro, J. Yvonnet, F. Chinesta, and E. Cueto. A study on the performance of natural neighbour-based galerkin methods. *International Journal for Numerical Methods in Engineering*, 71(12):1436–1465, 2007.
- [4] DM Anderson, G.B. McFadden, and AA Wheeler. Diffuse-interface methods in fluid mechanics. *Annual review of fluid mechanics*, 30(1):139–165, 1998.
- [5] M.J. Andrews and S.B. Dalziel. Small atwood number rayleigh–taylor experiments. *Philosophical Transactions of the Royal Society A: Mathematical, Physical and Engineering Sciences*, 368(1916):1663, 2010.
- [6] C. Antoci, M. Gallati, and S. Sibilla. Numerical simulation of fluid–structure interaction by sph. *Computers & structures*, 85(11):879–890, 2007.
- [7] N. Ashgriz and JY Poo. Flair: Flux line-segment model for advection and interface reconstruction. *Journal of Computational Physics*, 93(2):449–468, 1991.
- [8] E. Bänsch. *Numerical methods for the instationary Navier-Stokes equations with a free capillary surface*. PhD thesis, Schr., 1998.
- [9] J.B. Bell and D.L. Marcus. A second-order projection method for variable-density flows\* 1. *Journal of Computational Physics*, 101(2):334–348, 1992.

- 
- [10] T. Belytschko, DP Flanagan, and JM Kennedy. Finite element methods with user-controlled meshes for fluid-structure interaction. *Computer Methods in Applied Mechanics and Engineering*, 33(1-3):669–688, 1982.
- [11] R. Benzi, S. Succi, and M. Vergassola. The lattice boltzmann equation: theory and applications. *Physics Reports*, 222(3):145–197, 1992.
- [12] S. Borge and DJ Price. Hydrodynamical instabilities in compressible fluids using sph. In *Fourth International SPHERIC Workshop, Nantes, France*, pages 27–29, 2009.
- [13] JU Brackbill, D.B. Kothe, and C. Zemach. A continuum method for modeling surface tension\* 1. *Journal of computational physics*, 100(2):335–354, 1992.
- [14] U. Bulgarelli, V. Casulli, and D. Greenspan. Pressure methods for the numerical solution of free surface fluid flows. *Pineridge Press, Swansea, UK*, 1984.
- [15] B. Bunner and G. Tryggvason. Effect of bubble deformation on the properties of bubbly flows. *Journal of Fluid Mechanics*, 495(1):77–118, 2003.
- [16] S.H. Cha, S.I. Inutsuka, and S. Nayakshin. Kelvin–helmholtz instabilities with godunov smoothed particle hydrodynamics. *Monthly Notices of the Royal Astronomical Society*, 403(3):1165–1174, 2010.
- [17] Subrahmanyam Chandrasekhar. *Hydrodynamic and hydromagnetic stability*. Dover Pubns, 1961.
- [18] JK Chen and JE Beraun. A generalized smoothed particle hydrodynamics method for nonlinear dynamic problems. *Computer Methods in Applied Mechanics and Engineering*, 190(1):225–239, 2000.
- [19] J.S. Chen, C. Pan, C.T. Wu, and W.K. Liu. Reproducing kernel particle methods for large deformation analysis of non-linear structures. *Computer Methods in Applied Mechanics and Engineering*, 139(1):195–227, 1996.
- [20] A.J. Chorin. Numerical solution of the navier-stokes equations. *Math. Comp*, 22(104):745–762, 1968.
- [21] A.J. Chorin. On the convergence of discrete approximations to the navier-stokes equations. *Math. Comp*, 23(341-353):17, 1969.

- [22] KN Christodoulou and LE Scriven. Discretization of free surface flows and other moving boundary problems. *Journal of Computational Physics*, 99(1):39–55, 1992.
- [23] A. Colagrossi and M. Landrini. Numerical simulation of interfacial flows by smoothed particle hydrodynamics\* 1. *Journal of Computational Physics*, 191(2):448–475, 2003.
- [24] W. Crowley. Flag: a free-lagrange method for numerically simulating hydrodynamic flows in two dimensions. In *Proceedings of the Second International Conference on Numerical Methods in Fluid Dynamics*, pages 37–43. Springer, 1971.
- [25] S. J. Cummins and M. Rudman. An SPH projection method. *Journal of computational physics*, 152(2):584–607, 1999.
- [26] C. Cuvelier. A time dependent free boundary governed by the navier-stokes equations. In *Ninth International Conference on Numerical Methods in Fluid Dynamics*, pages 170–174. Springer, 1985.
- [27] C. Cuvelier and R. Schulkes. Some numerical methods for the computation of capillary free boundaries governed by the navier-stokes equations. *Siam Review*, pages 355–423, 1990.
- [28] RA Dalrymple and BD Rogers. Numerical modeling of water waves with the sph method. *Coastal engineering*, 53(2):141–147, 2006.
- [29] L. Delorme, A. Colagrossi, A. Souto-Iglesias, R. Zamora-Rodriguez, and E. Botia-Vera. A set of canonical problems in sloshing, part i: Pressure field in forced roll–comparison between experimental results and sph. *Ocean Engineering*, 36(2):168–178, 2009.
- [30] A. Dervieux and F. Thomasset. A finite element method for the simulation of a rayleigh-taylor instability. *Approximation methods for Navier-Stokes problems*, pages 145–158, 1980.
- [31] G. Dhatt, DM Gao, and A.B. Cheikh. A finite element simulation of metal flow in moulds. *International journal for numerical methods in engineering*, 30(4):821–831, 1990.

- [32] H. Ding, P.D.M. Spelt, and C. Shu. Diffuse interface model for incompressible two-phase flows with large density ratios. *Journal of Computational Physics*, 226(2):2078–2095, 2007.
- [33] J. Donea, S. Giuliani, and JP Halleux. An arbitrary lagrangian-eulerian finite element method for transient dynamic fluid-structure interactions. *Computer Methods in Applied Mechanics and Engineering*, 33(1-3):689–723, 1982.
- [34] P.G. Drazin and W.H. Reid. *Hydrodynamic stability*. Cambridge Univ Pr, 2004.
- [35] MS Engelman and RL Sani. Finite element simulation of incompressible fluid flows with a free/moving surface. *Computational Techniques for Fluid Flow*, 47, 1986.
- [36] J.S. Eow and M. Ghadiri. Motion, deformation and break-up of aqueous drops in oils under high electric field strengths. *Chemical Engineering and processing*, 42(4):259–272, 2003.
- [37] A.C. Eringen and G.A. Maugin. *Electrodynamics of continua*, volume 1. Springer New York, 1990.
- [38] A. Esmaeeli and G. Tryggvason. Direct numerical simulations of bubbly flows. part 1. low reynolds number arrays. *Journal of Fluid Mechanics*, 377(1):313–345, 1998.
- [39] A. Esmaeeli and G. Tryggvason. Direct numerical simulations of bubbly flows part 2. moderate reynolds number arrays. *Journal of Fluid Mechanics*, 385(1):325–358, 1999.
- [40] J. Feldman and J. Bonet. Dynamic refinement and boundary contact forces in sph with applications in fluid flow problems. *International Journal for Numerical Methods in Engineering*, 72(3):295–324, 2007.
- [41] J.Q. Feng and T.C. Scott. A computational analysis of electrohydrodynamics of a leaky dielectric drop in an electric field. *Journal of Fluid Mechanics*, 311(1):289–326, 1996.
- [42] ZC Feng and LG Leal. Nonlinear bubble dynamics. *Annual review of fluid mechanics*, 29(1):201–243, 1997.

- [43] JM Floryan and H. Rasmussen. Numerical methods for viscous flows with moving boundaries. *Applied Mechanics Reviews*, 42:323, 1989.
- [44] MJ Fritts and JP Boris. The lagrangian solution of transient problems in hydrodynamics using a triangular mesh. *Journal of Computational Physics*, 31(2):173–215, 1979.
- [45] D.E. Fyfe, E.S. Oran, and MJ Fritts. Surface tension and viscosity with lagrangian hydrodynamics on a triangular mesh. *Journal of Computational Physics*, 76(2):349–384, 1988.
- [46] R. A. Gingold and J. J. Monaghan. Smoothed particle hydrodynamics-theory and application to non-spherical stars. *Monthly Notices of the Royal Astronomical Society*, 181:375–389, 1977.
- [47] I. Ginzburg and G. Wittum. Two-phase flows on interface refined grids modeled with vof, staggered finite volumes, and spline interpolants. *Journal of Computational Physics*, 166(2):302–335, 2001.
- [48] J. Glimm, J. Grove, B. Lindquist, O.A. McBryan, and G. Tryggvason. The bifurcation of tracked scalar waves. *SIAM Journal on Scientific and Statistical Computing*, 9:61, 1988.
- [49] J. Glimm, O. McBryan, R. Menikoff, and DH Sharp. Front tracking applied to rayleigh–taylor instability. *SIAM Journal on Scientific and Statistical Computing*, 7:230, 1986.
- [50] JN Glosli, DF Richards, KJ Caspersen, RE Rudd, JA Gunnels, and FH Streitz. Extending stability beyond cpu millennium: a micron-scale atomistic simulation of kelvin-helmholtz instability. In *Proceedings of the 2007 ACM/IEEE Conference on Supercomputing*, page 58. ACM, 2007.
- [51] Moncho Gomez-Gesteira, Benedict D. Rogers, Damien Violeau, Jose Maria Grassa, and Alex J.C. Crespo. Foreword: Sph for free-surface flows. *Journal of Hydraulic Research*, 48(sup1):3–5, 2010.
- [52] VN Goncharov. Analytical model of nonlinear, single-mode, classical rayleigh-taylor instability at arbitrary atwood numbers. *Physical review letters*, 88(13):134502, 2002.

- [53] JP Gray, JJ Monaghan, and RP Swift. Sph elastic dynamics. *Computer methods in applied mechanics and engineering*, 190(49-50):6641–6662, 2001.
- [54] J.L. Guermond and L. Quartapelle. A projection fem for variable density incompressible flows. *Journal of Computational Physics*, 165(1):167–188, 2000.
- [55] J.W. Ha and S.M. Yang. Electrohydrodynamics and electrorotation of a drop with fluid less conductive than that of the ambient fluid. *Physics of Fluids*, 12:764, 2000.
- [56] WT Hancox, RL Ferch, WS Liu, and RE Nieman. One-dimensional models for transient gas-liquid flows in ducts. *International Journal of Multiphase Flow*, 6(1-2):25–40, 1980.
- [57] P. Hansbo. The characteristic streamline diffusion method for the time-dependent incompressible navier-stokes equations. *Computer methods in applied mechanics and engineering*, 99(2-3):171–186, 1992.
- [58] F.H. Harlow, J.E. Welch, et al. Numerical calculation of time-dependent viscous incompressible flow of fluid with free surface. *Physics of fluids*, 8(12):2182, 1965.
- [59] M. Hayashi, K. Hatanaka, and M. Kawahara. Lagrangian finite element method for free surface navier-stokes flow using fractional step methods. *International journal for numerical methods in fluids*, 13(7):805–840, 1991.
- [60] M. Herrmann. A eulerian level set/vortex sheet method for two-phase interface dynamics. *Journal of Computational Physics*, 203(2):539–571, 2005.
- [61] CW Hirt, A.A. Amsden, and JL Cook. An arbitrary lagrangian-eulerian computing method for all flow speeds\* 1. *Journal of computational physics*, 14(3):227–253, 1974.
- [62] CW Hirt and JL Cook. Calculating three-dimensional flows around structures and over rough terrain\* 1. *Journal of Computational Physics*, 10(2):324–340, 1972.
- [63] CW Hirt, JL Cook, and TD Butler. A lagrangian method for calculating the dynamics of an incompressible fluid with free surface\* 1. *Journal of Computational Physics*, 5(1):103–124, 1970.
- [64] C.W. Hirt and B.D. Nichols. Volume of fluid (vof) method for the dynamics of free boundaries\* 1. *Journal of computational physics*, 39(1):201–225, 1981.

- [65] W.G. Hoover. Isomorphism linking smooth particles and embedded atoms. *Physica-Section A*, 260(3):244–254, 1998.
- [66] T.Y. Hou. Numerical solutions to free boundary problems. *Acta Numerica*, 4(1):335–415, 1995.
- [67] X. Y. Hu and N. A. Adams. A multi-phase SPH method for macroscopic and mesoscopic flows. *Journal of Computational Physics*, 213(2):844–861, 2006.
- [68] X. Y. Hu and N. A. Adams. An incompressible multi-phase SPH method. *Journal of Computational Physics*, 227(1):264–278, 2007.
- [69] J. Hua, L.K. Lim, and C.H. Wang. Numerical simulation of deformation/motion of a drop suspended in viscous liquids under influence of steady electric fields. *Physics of Fluids*, 20:113302, 2008.
- [70] J. Hua and J. Lou. Numerical simulation of bubble rising in viscous liquid. *Journal of Computational Physics*, 222(2):769–795, 2007.
- [71] J. P. Hughes and D. I. Graham. Comparison of incompressible and weakly-compressible sph models for free-surface water flows. *Journal of hydraulic research*, 48:105–117, 2010.
- [72] T.J.R. Hughes, W.K. Liu, and T.K. Zimmermann. Lagrangian-eulerian finite element formulation for incompressible viscous flows\* 1. *Computer Methods in Applied Mechanics and Engineering*, 29(3):329–349, 1981.
- [73] J.M. Hyman. Numerical methods for tracking interfaces. *Physica D: Nonlinear Phenomena*, 12(1-3):396–407, 1984.
- [74] R. Issa, E. S. Lee, D. Violeau, and D. R. Laurence. Incompressible separated flows simulations with the smoothed particle hydrodynamics gridless method. *International journal for numerical methods in fluids*, 47(10-11):1101–1106, 2005.
- [75] S. Jun, W.K. Liu, and T. Belytschko. Explicit reproducing kernel particle methods for large deformation problems. *International Journal for Numerical Methods in Engineering*, 41(1):137–166, 1998.
- [76] V. Junk, F. Heitsch, and T. Naab. The kelvin-helmholtz instability in smoothed-particle hydrodynamics. *Proceedings of the International Astronomical Union*, 2(S235):210–210, 2006.

- [77] HS Kheshgi and LE Scriven. Penalty-finite element analysis of time-dependent two-dimensional free surface film flows. In *Finite Element Flow Analysis*, volume 1, pages 113–120, 1982.
- [78] E.S. Kordyban, T. Ranov, and American Society of Mechanical Engineers. Mechanism of slug formation in horizontal two-phase flow. ASME, 1970.
- [79] Y. Krongauz and T. Belytschko. Enforcement of essential boundary conditions in meshless approximations using finite elements. *Computer Methods in Applied Mechanics and Engineering*, 131(1-2):133–145, 1996.
- [80] S. Kulasegaram, J. Bonet, R. W. Lewis, and M. Profit. A variational formulation based contact algorithm for rigid boundaries in two-dimensional sph applications. *Computational Mechanics*, 33(4):316–325, 2004.
- [81] E. Lac and GM Homsy. Axisymmetric deformation and stability of a viscous drop in a steady electric field. *Journal of Fluid Mechanics*, 590:239–264, 2007.
- [82] B. Lafaurie, C. Nardone, R. Scardovelli, S. Zaleski, and G. Zanetti. Modelling merging and fragmentation in multiphase flows with surfer. *Journal of Computational Physics*, 113(1):134–147, 1994.
- [83] H. Lamb and S.H. Lamb. *Hydrodynamics*. Cambridge Univ Pr, 1997.
- [84] E. S. Lee, C. Moulinec, R. Xu, D. Violeau, D. Laurence, and P. Stansby. Comparisons of weakly compressible and truly incompressible algorithms for the sph mesh free particle method. *Journal of Computational Physics*, 227(18):8417–8436, 2008.
- [85] E. S. Lee, D. Violeau, R. Issa, and S. Ploix. Application of weakly compressible and truly incompressible sph to 3-d water collapse in waterworks. *Journal of Hydraulic Research*, 48(S1):50–60, 2010.
- [86] RW Lewis and K. Ravindran. Finite element simulation of metal casting. *International journal for numerical methods in engineering*, 47(1-3):29–59, 2000.
- [87] J. Li, Y.Y. Renardy, and M. Renardy. A numerical study of periodic disturbances on two-layer couette flow. *Physics of Fluids*, 10:3056, 1998.

- [88] PY Lin and TJ Hanratty. Prediction of the initiation of slugs with linear stability theory. *International journal of multiphase flow*, 12(1):79–98, 1986.
- [89] PY Lin and TJ Hanratty. Effect of pipe diameter on flow patterns for air-water flow in horizontal pipes. *International journal of multiphase flow*, 13(4):549–563, 1987.
- [90] M. B. Liu and G. R. Liu. Smoothed particle hydrodynamics (sph): an overview and recent developments. *Archives of Computational Methods in Engineering*, 17(1):25–76, 2010.
- [91] W.K. Liu, S. Jun, S. Li, J. Adee, and T. Belytschko. Reproducing kernel particle methods for structural dynamics. *International Journal for Numerical Methods in Engineering*, 38(10):1655–1679, 1995.
- [92] W.K. Liu, S. Jun, D.T. Sihling, Y. Chen, and W. Hao. Multiresolution reproducing kernel particle method for computational fluid dynamics. *International journal for numerical methods in fluids*, 24(12):1391–1415, 1997.
- [93] W.K. Liu, S. Jun, and Y.F. Zhang. Reproducing kernel particle methods. *International Journal for Numerical Methods in Fluids*, 20(8-9):1081–1106, 1995.
- [94] L. B. Lucy. A numerical approach to the testing of the fission hypothesis. *The Astronomical Journal*, 82:1013–1024, 1977.
- [95] U.B. Mehta and Z. Lavan. Starting vortex, separation bubbles and stall- a numerical study of laminar unsteady flow around an airfoil. *Journal of Fluid Mechanics*, 67(Part 2):227–256, 1975.
- [96] JR Melcher and GI Taylor. Electrohydrodynamics: a review of the role of interfacial shear stresses. *Annual Review of Fluid Mechanics*, 1(1):111–146, 1969.
- [97] K.O. Mikaelian. Effect of viscosity on rayleigh-taylor and richtmyer-meshkov instabilities. *Physical Review E*, 47(1):375, 1993.
- [98] L.M. Milne-Thomson. *Theoretical hydrodynamics*. Dover Pubns, 1996.
- [99] J. J. Monaghan. Smoothed particle hydrodynamics. *Annual Review of Astronomy and Astrophysics*, 30:543–574, 1992.

- 
- [100] J. J. Monaghan. Simulating free surface flows with SPH. *Journal of computational physics*, 110:399–399, 1994.
- [101] J. J. Monaghan. SPH without a tensile instability. *Journal of Computational Physics*, 159(2):290–311, 2000.
- [102] J. J. Monaghan. Smoothed particle hydrodynamics. *Reports on Progress in Physics*, 68:1703, 2005.
- [103] J. J. Monaghan and A. Kos. Solitary waves on a cretan beach. *Journal of Waterway, Port, Coastal and Ocean Engineering*, 125(3):145–154, 1999.
- [104] J. P. Morris. Simulating surface tension with smoothed particle hydrodynamics. *International Journal for Numerical Methods in Fluids*, 33(3):333–353, 2000.
- [105] J. P. Morris, P. J. Fox, and Y. Zhu. Modeling low reynolds number incompressible flows using sph. *Journal of Computational Physics*, 136(1):214–226, 1997.
- [106] T.J. Mueller and S.M. Batil. Experimental studies of separation on a two-dimensional airfoil at low reynolds numbers. *AIAA Journal*, 20:457–463, 1982.
- [107] W. Noh and P. Woodward. Slic (simple line interface calculation). In *Proceedings of the Fifth International Conference on Numerical Methods in Fluid Dynamics June 28–July 2, 1976 Twente University, Enschede*, pages 330–340. Springer, 1976.
- [108] M. Oevermann, R. Klein, M. Berger, and J. Goodman. *A projection method for two-phase incompressible flow with surface tension and sharp interface resolution*. Konrad-Zuse-Zentrum für Informationstechnik Berlin, 2000.
- [109] A. Okajima. Strouhal numbers of rectangular cylinders. *J. Fluid Mech*, 123:379–398, 1982.
- [110] T. Okamoto and M. Kawahara. Two-dimensional sloshing analysis by lagrangian finite element method. *International Journal for Numerical Methods in Fluids*, 11(5):453–477, 1990.
- [111] S. Osher and J.A. Sethian. Fronts propagating with curvature-dependent speed: algorithms based on hamilton-jacobi formulations. *Journal of computational physics*, 79(1):12–49, 1988.

- [112] AR Piriz, OD Cortazar, J.J.L. Cela, and NA Tahir. The rayleigh-taylor instability. *American journal of physics*, 74:1095, 2006.
- [113] S. Popinet and S. Zaleski. A front-tracking algorithm for accurate representation of surface tension. *International Journal for Numerical Methods in Fluids*, 30(6):775–793, 1999.
- [114] J. Pozorski and A. Wawrenczuk. SPH computation of incompressible viscous flows. *JOURNAL OF THEORETICAL AND APPLIED MECHANICS-WARSAW-*, 40:917–938, 2002.
- [115] C. Pozrikidis. Instability of two-layer creeping flow in a channel with parallel-sided walls. *Journal of Fluid Mechanics*, 351:139–165, 1997.
- [116] D.J. Price. Modelling discontinuities and kelvin-helmholtz instabilities in sph. *Journal of Computational Physics*, 227(24):10040–10057, 2008.
- [117] E.G. Puckett, A.S. Almgren, J.B. Bell, D.L. Marcus, and W.J. Rider. A high-order projection method for tracking fluid interfaces in variable density incompressible flows\* 1. *Journal of Computational Physics*, 130(2):269–282, 1997.
- [118] DI Pullin. Numerical studies of surface-tension effects in nonlinear kelvin-helmholtz and rayleigh-taylor instability. *Journal of Fluid Mechanics*, 119(1):507–532, 1982.
- [119] P. Ramaprabhu, G. Dimonte, and MJ Andrews. A numerical study of the influence of initial perturbations on the turbulent rayleigh-taylor instability. *Journal of Fluid Mechanics*, 536(1):285–319, 2005.
- [120] P. Ramaprabhu, G. Dimonte, Y.N. Young, AC Calder, and B. Fryxell. Limits of the potential flow approach to the single-mode rayleigh-taylor problem. *Physical Review E*, 74(6):066308, 2006.
- [121] B. Ramaswamy and M. Kawahara. Arbitrary lagrangian-eulerian finite element method for unsteady, convective, incompressible viscous free surface fluid flow. *International Journal for Numerical Methods in Fluids*, 7(10):1053–1075, 1987.
- [122] J.D. Ramshaw and J.A. Trapp. A numerical technique for low-speed homogeneous two-phase flow with sharp interfaces\* 1. *Journal of Computational Physics*, 21(4):438–453, 1976.

- [123] P. W. Randles and L. D. Libersky. Smoothed particle hydrodynamics: some recent improvements and applications. *Computer methods in Applied mechanics and Engineering*, 139(1-4):375–408, 1996.
- [124] L. Rayleigh. Investigation of the character of the equilibrium of an incompressible heavy fluid of variable density. *Proc. Lond. Math. Soc.*, 14(1):170–177, 1883.
- [125] W.J. Rider and D.B. Kothe. Reconstructing volume tracking\* 1,\* 2. *Journal of computational physics*, 141(2):112–152, 1998.
- [126] D.H. Rothman and S. Zaleski. Lattice-gas models of phase separation: interfaces, phase transitions, and multiphase flow. *Reviews of Modern Physics*, 66(4):1417, 1994.
- [127] D.H. Rothman and S. Zaleski. *Lattice-gas cellular automata: simple models of complex hydrodynamics*, volume 5. Cambridge Univ Pr, 2004.
- [128] M. Rudman. Volume-tracking methods for interfacial flow calculations. *International Journal for Numerical Methods in Fluids*, 24(7):671–691, 1997.
- [129] K.J. Ruschak. A method for incorporating free boundaries with surface tension in finite element fluid-flow simulators. *International Journal for Numerical Methods in Engineering*, 15(5):639–648, 1980.
- [130] AC Rust and M. Manga. Effects of bubble deformation on the viscosity of dilute suspensions. *Journal of non-newtonian fluid mechanics*, 104(1):53–63, 2002.
- [131] H. Saito and LE Scriven. Study of coating flow by the finite element method. *Journal of Computational Physics*, 42(1):53–76, 1981.
- [132] DA Saville. Electrohydrodynamics: the taylor-melcher leaky dielectric model. *Annual review of fluid mechanics*, 29(1):27–64, 1997.
- [133] R. Scardovelli and S. Zaleski. Direct numerical simulation of free-surface and interfacial flow. *Annual Review of Fluid Mechanics*, 31(1):567–603, 1999.
- [134] RS Scorer. Experiments on convection of isolated masses of buoyant fluid. *Journal of Fluid Mechanics*, 2(06):583–594, 1957.

- [135] MS Shadloo and M. Yildiz. Numerical modeling of kelvin–helmholtz instability using smoothed particle hydrodynamics. *International Journal for Numerical Methods in Engineering*, 87:988–1006, 2011.
- [136] M.S. Shadloo, A. Zainali, S.H. Sadek, and M. Yildiz. Improved incompressible smoothed particle hydrodynamics method for simulating flow around bluff bodies. *Computer methods in applied mechanics and engineering*, 200(9):1008–1020, 2011.
- [137] MS Shadloo, A. Zainali, and M. Yildiz. Simulation of single mode rayleigh–taylor instability by sph method. *Computational Mechanics*, pages 1–17, 2012.
- [138] M.S. Shadloo, A. Zainali, M. Yildiz, and A. Suleman. A robust weakly compressible sph method and its comparison with an incompressible sph. *International Journal for Numerical Methods in Engineering*, 2011.
- [139] S. Shao and E. Y. M. Lo. Incompressible SPH method for simulating Newtonian and non-Newtonian flows with a free surface. *Advances in Water Resources*, 26(7):787–800, 2003.
- [140] P.J. Shopov, P.D. Minev, and I.B. Bazhlekov. Numerical method for unsteady viscous hydrodynamical problem with free boundaries. *International journal for numerical methods in fluids*, 14(6):681–705, 1992.
- [141] W. Shyy, HS Udaykumar, M.M. Rao, and RW Smith. Computational fluid dynamics with moving boundaries. series in computational and physical processes in mechanics and thermal sciences. *WJ Minkowycz and EM Sparrow ed*, 1996.
- [142] J. C. Simpson and M. A. Wood. Classical kinetic theory simulations using smoothed particle hydrodynamics. *Physical Review E*, 54(2):2077, 1996.
- [143] A. Smolianski. *Numerical modeling of two-fluid interfacial flows*. University of Jyväskylä, 2001.
- [144] M. Sussman and P. Smereka. Axisymmetric free boundary problems. *Journal of Fluid Mechanics*, 341(1):269–294, 1997.
- [145] M. Sussman, P. Smereka, and S. Osher. A level set approach for computing solutions to incompressible two-phase flow. *Journal of computational Physics*, 114(1):146–159, 1994.

- [146] Y. Taitel and AE Dukler. A model for predicting flow regime transitions in horizontal and near horizontal gas-liquid flow. *AIChE Journal*, 22(1):47–55, 1976.
- [147] H. Takeda, S. M. Miyama, and M. Sekiya. Numerical simulation of viscous flow by smoothed particle hydrodynamics. *Progress of Theoretical Physics*, 92(5):939–960, 1994.
- [148] A. M. Tartakovsky and P. Meakin. A smoothed particle hydrodynamics model for miscible flow in three-dimensional fractures and the two-dimensional rayleigh-taylor instability. *Journal of Computational Physics*, 207(2):610–624, 2005.
- [149] A.M. Tartakovsky, P. Meakin, T.D. Scheibe, and B.D. Wood. A smoothed particle hydrodynamics model for reactive transport and mineral precipitation in porous and fractured porous media. *Water resources research*, 43(5):W05437, 2007.
- [150] G. Taylor. The instability of liquid surfaces when accelerated in a direction perpendicular to their planes. i. *Proceedings of the Royal Society of London. Series A, Mathematical and Physical Sciences*, pages 192–196, 1950.
- [151] G. Taylor and G. Taylor. Studies in electrohydrodynamics. i. the circulation produced in a drop by electrical field. *Proceedings of the Royal Society of London. Series A. Mathematical and Physical Sciences*, 291(1425):159–166, 1966.
- [152] TE Tezduyar, M. Behr, S. Mittal, and J. Liou. A new strategy for finite element computations involving moving boundaries and interfaces—the deforming-spatial-domain/space-time procedure: I. the concept and the preliminary numerical tests. *Computer methods in applied mechanics and engineering*, 94(3):339–351, 1992.
- [153] TE Tezduyar, M. Behr, S. Mittal, and J. Liou. A new strategy for finite element computations involving moving boundaries and interfaces—the deforming-spatial-domain/space-time procedure: Ii. computation of free-surface flows, two-liquid flows, and flows with drifting cylinders. *Computer methods in applied mechanics and engineering*, 94(3):353–371, 1992.
- [154] E. Thompson. Use of pseudo-concentrations to follow creeping viscous flows during transient analysis. *International journal for numerical methods in fluids*, 6(10):749–761, 1986.

- [155] G. Tomar, D. Gerlach, G. Biswas, N. Alleborn, A. Sharma, F. Durst, SWJ Welch, and A. Delgado. Two-phase electrohydrodynamic simulations using a volume-of-fluid approach. *Journal of Computational Physics*, 227(2):1267–1285, 2007.
- [156] A.K. Tornberg. Interface tracking methods with application to multiphase flows. 2000.
- [157] S. Torza, RG Cox, and SG Mason. Electrohydrodynamic deformation and burst of liquid drops. *Philosophical Transactions of the Royal Society of London. Series A, Mathematical and Physical Sciences*, 269(1198):295–319, 1971.
- [158] G. Tryggvason. Numerical simulations of the rayleigh-taylor instability. *Journal of Computational Physics*, 75(2):253–282, 1988.
- [159] G. Tryggvason, B. Bunner, O. Ebrat, and W. Tauber. Computations of multiphase flows by a finite difference/front tracking method. i. multi-fluid flows. *LECTURE SERIES-VON KARMAN INSTITUTE FOR FLUID DYNAMICS*, pages 7–7, 1998.
- [160] W.T. Tsai and D.K.P. Yue. Computation of nonlinear free-surface flows. *Annual review of fluid mechanics*, 28(1):249–278, 1996.
- [161] S.O. Unverdi and G. Tryggvason. A front-tracking method for viscous, incompressible, multi-fluid flows. *Journal of Computational Physics*, 100(1):25–37, 1992.
- [162] JT Waddell, CE Niederhaus, and JW Jacobs. Experimental study of rayleigh–taylor instability: low atwood number liquid systems with single-mode initial perturbations. *Physics of Fluids*, 13:1263, 2001.
- [163] G.B. Wallis and J.E. Dodson. The onset of slugging in horizontal stratified air-water flow. *International Journal of Multiphase Flow*, 1(1):173–193, 1973.
- [164] S.W.J. Welch and G. Biswas. Direct simulation of film boiling including electrohydrodynamic forces. *Physics of Fluids*, 19:012106, 2007.
- [165] JP Wilkinson and JW Jacobs. Experimental study of the single-mode three-dimensional rayleigh-taylor instability. *Physics of Fluids*, 19:124102, 2007.
- [166] J. Xie, L.K. Lim, Y. Phua, J. Hua, and C.H. Wang. Electrohydrodynamic atomization for biodegradable polymeric particle production. *Journal of colloid and interface science*, 302(1):103–112, 2006.

- 
- [167] J.Y. Yang and J.W. Chang. Rarefied flow instability simulation using model boltzmann equations. In *AIAA, Fluid Dynamics Conference, 28 th, Snowmass Village, CO*, 1997.
- [168] M. Yildiz, R. A. Rook, and A. Suleman. Sph with the multiple boundary tangent method. *International Journal for Numerical Methods in Engineering*, 77(10):1416–1438, 2009.
- [169] D.L. Youngs. Numerical simulation of turbulent mixing by rayleigh-taylor instability. *Physica D: Nonlinear Phenomena*, 12(1-3):32–44, 1984.
- [170] A. Zainali, N. Tofghi, M. Safdari Shadloo, and M. Yildiz. Numerical investigation of newtonian and non-newtonian multiphase flows using isph method. *Computer Methods in Applied Mechanics and Engineering*, 254:99–113, 2013.
- [171] J. Zhang and D.Y. Kwok. A 2d lattice boltzmann study on electrohydrodynamic drop deformation with the leaky dielectric theory. *Journal of Computational Physics*, 206(1):150–161, 2005.
- [172] R. Zhang, X. He, G. Doolen, and S. Chen. Surface tension effects on two-dimensional two-phase kelvin-helmholtz instabilities. *Advances in water resources*, 24(3-4):461–478, 2001.